Volume 97, Number 2, March–April 1992
Journal of Research of the National Institute of Standards and Technology

Contents

Articles

The Development of a Standard Reference Material for Calibration of the University of Pittsburgh Smoke Toxicity Method for Assessing the Acute Inhalation Toxicity of Combustion Products	**Barbara C. Levin, Yves Alarie, Maryanne F. Stock, and Susannah B. Schiller**	245
Certification of NIST SRM 1962: 3 μm Diameter Polystyrene Spheres	**Arie W. Hartman, Theordore D. Doiron, and Joseph Fu**	253
Optical Calibration of a Submicrometer Magnification Standard	**Jon Geist, Barbara Belzer, Mary Lou Miller, and Peter Roitman**	267
Probe-Position Error Correction in Planar Near Field Measurements at 60 GHz: Experimental Verification	**Lorant A. Muth**	273
Measuring the Electron's Charge and the *Fine-Structure Constant by Counting* Electrons on a Capacitor	**E. R. Williams, Ruby N. Ghosh, and John M. Martinis**	299

Volume 97, Number 2, March–April 1992
Journal of Research of the National Institute of Standards and Technology

News Briefs

GENERAL DEVELOPMENTS 305

Bioassay Reference Values Established for Three NIST SRMs
Analytical Method Developed to Investigate the Role of Vitamin C in Cancer Prevention and Juvenile Arthritis

Intramolecular Vibrational Energy Redistribution Studied by Picosecond IR Spectroscopy 306
Frequency and Wavelength Standard for the Far Infrared
In Situ Characterization of the Pulsed Laser Deposition of Thin Films
New Computational Method for Pattern Formation During Alloy Solidification

Fiber Laser Offers Wavelength Standard 307
NIST Research Leads to Significant Yield Improvement in the Manufacture of Memory Chips
NIST Leads Industry to Accord in X-Ray Mask Specifications

Neutron Reflectometry Helps Characterize Polymer Brushes 308
Fast Restoration of Images
Neutron Focusing Using Capillary Optics

NIST Develops Methods for High-Precision Phase Noise Measurements 309
Hubble Data Suggest No End for Universe
New "Measures" Needed to Boost Productivity
Measurement Service for CW Wattmeters Coming
New Glossary of Computer Security Terminology

New Proceedings Issued on High Integrity Software 310
Automated Manufacturing Stars in New VHS Program
NIST Reports on ISO 9000 Standard Series
Software Package for Antenna Metrology Available

New Guide Designed to Help Federal GOSIP Users 311
Book Reviews Supercritical Fluid Extraction
Video Highlights 1991 Baldrige Award Winners
Radio Waves "Lower the Boom" on Buried Mines
Photonic Probes Developed to Measure EM Fields

Shaping New Designs for Wave Probes 312
IC Device Offers Improved Speed, Accuracy
Alaska Marine Mammal Pollution Data Available
Superconductor Abstracts Compiled in Single Volume

Report Details Risks, Handling Care for 3480 Tape 313
NIST Issues "How-To" Manual on Smoke Control
Better Solutions for Wave Equations Offered
New Microscope Offers Unprecedented Range

New Test Improves Understanding of Smoke Danger 314
New Detector for Gas Chromatography Patented
Guide Makes SRMs Useful Tools in Chemistry Labs
CARB Solves Second Sugar Transport Protein

Volume 97, Number 2, March–April 1992
Journal of Research of the National Institute of Standards and Technology

Papers Requested for Fall Optics Symposium 315
Conformity Assessment Program Proposed
New Atlas Improves Infrared Spectrometry Calibrations
Comments Sought for Language C Test Method
Report Examines "Bridging" SGML/ODA Standards

Summer Technology Outreach Conferences Scheduled 316
NIST Laboratory Metrology Seminar Held at the University of Puerto Rico (UPR), Mayaguez
Spherical-Wave Expansions of Piston-Radiator Fields, Algorithm Derived

NIST to Apply Probe Position-Error Correction in New Near-Field Spherical Scanning Range 317
NIST Scientist Reports Findings of NASA's Airborne Arctic Stratospheric Expedition II
Fluid Equilibration in Low Gravity

NIST Radio Broadcasts to Support INSPIRE Program for High School Science Students 318
Ionospheric Receiver Technology Transferred to Industry
Observation of "Quantum Projection" Noise

Apparatus for Measuring Thermal Conductivity at Low Temperatures 319
Proposed Consortium on Casting of Aerospace Alloys
Electrodeposition of Compositionally Modulated Alloys
Technology of Glass-Ceramic Inserts Transferred to Dental Materials Industry
Predicting Performance of Adhesive Bonds

NIST Study of Staging Areas for Persons with Mobility Limitations 320
NIST Collaborates with the National Archives and Records Administration (NARA) on Optical Disk Technology
NIST Proposes Federal Information Processing Standard (FIPS) for Secure Hash Standard
Spatial Data Transfer Standard Implementation Workshop Attracts Large Turnout

International Workshop on Harmonizing Conformance Testing of Programming Language Standards Held 321

CALIBRATION SERVICES 321
Udated Calibration Services Users Guide Available

STANDARD REFERENCE MATERIALS 321
Easy Access to Materials Standards Offered

SRM Improves Lead Poisoning Diagnosis Accuracy 322
Sample Available for Human Hair Drug Analysis
Standard Reference Material 893 and 1295—Stainless Steel (SAE 405)
Standard Reference Material 2708—Zinc Sulfide Thin Film on Polycarbonate
Standard Reference Material 2034—Holmium Oxide Solution Wavelength Standard 240 to 650 nm

Reference Materials 8506 and 8507—Moisture in Transformer Oil and in Mineral Oil 323

STANDARD REFERENCE DATA 323
New PC Package Speeds Chemical Microanalysis

Calendar 325

Volume 97, Number 2, March-April 1992
Journal of Research of the National Institute of Standards and Technology

[J. Res. Natl. Inst. Stand. Technol. 97, 245 (1992)]

The Development of a Standard Reference Material for Calibration of the University of Pittsburgh Smoke Toxicity Method for Assessing the Acute Inhalation Toxicity of Combustion Products

Volume 97 | Number 2 | March-April 1992

Barbara C. Levin

National Institute of Standards and Technology, Gaithersburg, MD 20899

Yves Alarie and Maryanne F. Stock

University of Pittsburgh, Pittsburgh, PA 15261

and

Susannah B. Schiller

National Institute of Standards and Technology, Gaithersburg, MD 20899

A standard reference material (SRM 1049) has been developed for the University of Pittsburgh smoke toxicity method. SRM 1049 is a nylon 6/6 and has the molecular structure of $[-NH(CH_2)_6NHCO(CH_2)_4CO-]_n$. This SRM is for calibrating the apparatus and providing confidence that the method is being conducted in a correct manner and that the equipment is functioning properly. The certified figure of merit is a LC_{50} value plus its 95% prediction interval which were calculated and found to be 4.4 + 3.4 g. The 95% prediction interval indicates the range in which the next determined LC_{50} value would be expected to fall. Thus, if an investigator were to test this SRM under their laboratory conditions according to the specifications of the University of Pittsburgh test procedure and found the LC_{50} value fell within the certified 95% prediction interval, the probability is good that the test is being conducted correctly.

Key words: combustion; combustion products; inhalation; nylon; nylon 6/6; SRM; standard reference material; toxicity tests; University of Pittsburgh.

Accepted: February 10, 1992

1. Introduction

In 1973, The National Commission on Fire Prevention and Control issued the report "America Burning" [1] which noted that most fire victims die from inhaling smoke and toxic gases. This information served as one of the motivating forces in the development and testing of many smoke toxicity test procedures [2]. In 1983, 13 of these published methods were evaluated by Arthur D. Little, Inc. to assess the feasibility of incorporating combustion toxicity requirements for building materials and finishes into the building codes of New York State [3]. On the basis of seven different criteria, only two methods were found acceptable. These two methods were the flow-through smoke toxicity method developed at the University of Pittsburgh [4,5] and the closed-system cup furnace smoke toxicity method [6] developed at the National Institute of Standards and Technology (NIST).

Based on the results of the A. D. Little report, the state of New York under Article 15, Part 1120 of the New York State Fire Prevention and Building Code decided that building materials and finishes should be examined by the method developed at the University of Pittsburgh and that the results be filed with the state [7]. It is important to note, however, that although the results are filed, the state of New York does not regulate any materials or products based on the results of toxicity testing. It is also important to note that, at the present time, no smoke toxicity method has been accepted as a standard test by ASTM or any other national or international scientific or technical society designed

to develop standard test procedures. Thus, the development of other smoke toxicity methods is still being actively pursued.

Three methods currently under development are the University of Pittsburgh II radiant furnace method [8,9,10], a radiant furnace smoke toxicity protocol [11,12] which is being developed at NIST and the National Institute of Building Sciences (NIBS) toxic hazard test method [13,14]. Although these methods differ significantly in numerous characteristics, all three use radiant heat to decompose materials. Documentation of the relevance and accuracy of the radiant methodology may be found in Refs. [11] and [12].

Over the past decade, the number of smoke toxicity test apparatus users has increased. A number of Federal agencies, industrial laboratories, and testing companies are capable of conducting both the University of Pittsburgh and the cup furnace smoke toxicity test procedures. Although there are no state or federal regulations, the results of these smoke toxic potency tests, along with the results of other material flammability tests, are being used in the decision making process regarding material selection and overall fire hazard. Therefore, it is necessary to assure that such testing devices are installed and employed properly both by those laboratories currently conducting these tests and by new laboratories that enter the field. To help assure the reproducibility of results between laboratories, NIST has developed two standard reference materials (SRMs), one which can be used to calibrate the University of Pittsburgh smoke toxicity method (SRM 1049) and another SRM (SRM 1048) which can be used to calibrate the cup furnace smoke toxicity method [15]. *It is important to note that these SRMs were not selected to represent the toxic potency of the combustion products of an "average" material and are not designed to be used for the comparison of the relative toxic potency of the combustion products of test materials. Therefore, toxic potency of the smoke from a test material should not be compared to the toxic potency of the smoke from these SRMs.*

The following criteria were used in the selection process of the University of Pittsburgh smoke toxicity SRM:

1. The material should have reproducible burning characteristics (i.e., the material must be homogeneous),
2. The material should produce combustion products whose toxic potency values are within the range where the values for some other materials are found,
3. Upon combustion, toxic gases in addition to CO should be generated and contribute to the lethal atmospheres, and
4. The selected material should generate combustion products which cause deaths during the animal exposures. The University of Pittsburgh method does not specify the post-exposure observation of the test animals other than an immediate 10 min period following the exposure.

The polymer nylon 6/6, whose characteristics fit the above criteria, was selected for the University of Pittsburgh smoke toxicity SRM. An intralaboratory evaluation (performed at the University of Pittsburgh, Pittsburgh, PA) and an interlaboratory evaluation (carried out by Anderson Laboratories, Inc., Dedham, MA, Southwest Research Institute, San Antonio, TX, University of Pittsburgh, U.S. Testing Co., Inc., Hoboken, NJ, and Weyerhaeuser Co., Longview, WA) were conducted to determine the repeatability of results within a laboratory and reproducibility of results between laboratories, respectively. When the intra- and interlaboratory evaluations showed good repeatability and reproducibility of results with nylon 6/6, additional material of a single lot number was ordered for certification as an SRM. Further testing of the new lot was conducted by University of Pittsburgh and Anderson Laboratories to provide the data necessary for the development of the final certified SRM.

This paper documents the research and development of SRM 1049 which will be used to calibrate the University of Pittsburgh smoke toxicity test procedure and will help assure that the apparatus is performing correctly. To use SRM 1049 in the calibration of the test procedure, a laboratory would determine the LC_{50} value of the SRM according to the published University of Pittsburgh test procedure [4,5,7] and compare it with the certified LC_{50} value and its 95% prediction interval.[1] If the experimental value obtained by the laboratory falls within the 95% prediction interval of the certified LC_{50} value of this SRM, the investigator can be confident that the method is being conducted correctly.

[1] In the University of Pittsburgh smoke toxicity method, the LC_{50} is defined as the statistical estimate of the amount of material (in grams) which, when placed into the furnace, would cause 50% of the exposed mice to die within the 30 min exposure and the 10 min post-exposure observation period.

2. Materials and Methods

2.1 Materials

Two separate lots of nylon 6/6 [poly(hexamethylene adipamide)] with a molecular structure of $[-NH(CH_2)_6NHCO(CH_2)_4CO-]_n$ were obtained from Aldrich Chemical Co.[2] The first sample of nylon 6/6 (lot 80078; hereafter referred to as lot 1) was tested by the University of Pittsburgh and four other laboratories. Based on the results of this interlaboratory evaluation of the University of Pittsburgh smoke toxicity method, nylon 6/6 was found to be a suitable candidate for an SRM. A second batch of nylon 6/6 was ordered for certification purposes. The second batch of nylon 6/6 was in the same pellet form and had the same manufacturer specifications as the first batch, but had a different lot number (lot 08015; hereafter referred to as lot 2). Each bottle containing 1 kg of nylon 6/6 (lot 2) was randomly numbered when received at NIST. Samples of four bottles, Nos. 10, 20, 30, and 40, from lot 2 were used for certification purposes.

2.2 Animals

Swiss Webster mice weighing between 22 and 28 g were used for this study. They were allowed to acclimate to the laboratory conditions for approximately 1 week. Animals were group housed with free availability of food and water. Only animals appearing healthy were used for the study.

2.3 Experimental Method

The University of Pittsburgh smoke toxicity method to evaluate the acute inhalation toxicity of combustion products was developed by Alarie and Anderson [4,5]. The experimental arrangement is illustrated in Fig. 1. In this method, the sample is placed on a load sensor in the furnace at room temperature. The temperature is then increased at the rate of 20 °C/min. The temperature at which the sample begins to decompose, the rate at which the material decomposes as the temperature increases, and the time of ignition (i.e., flaming) of the sample are recorded.

Animal (head only) exposure to the thermal decomposition products is started when 1.0% mass loss of the material occurs. Four Swiss Webster male mice between 22 and 28 g in weight are exposed in each experiment. The exposure is 30 min in duration. The toxicological endpoint is death which occurs during the 30 min exposure period and a 10 min post-exposure observation period. The amount of material which releases enough smoke to cause either 0, 25, 50, 75, or 100% of the animals to die is used to calculate the LC_{50} values. During the animal exposures, the major combustion products, carbon monoxide (CO), carbon dioxide (CO_2), and reduced oxygen (O_2) are continuously monitored.

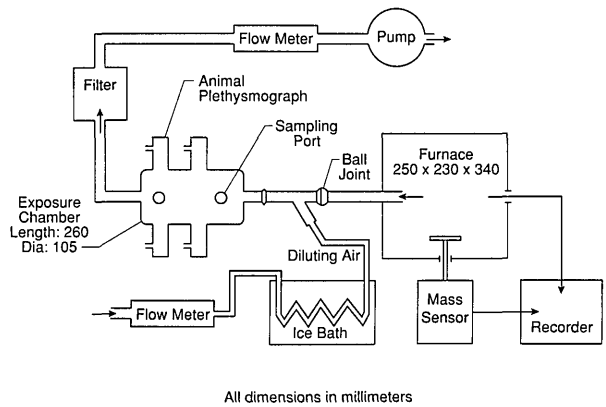

Fig. 1. Schematic of the experimental test system used to decompose the sample and expose the animals.

In the evaluation and development of SRM 1049 (i.e., data presented in this paper), the LC_{50} values and their 95% confidence limits were determined by the statistical method of Weil [16]. At the University of Pittsburgh, CO, CO_2, and O_2 were measured continuously by a Miran 1A infrared gas analyzer[3], a Beckman LB-2 medical gas analyzer, and a Beckman OM-11 oxygen analyzer, respectively. At Anderson Laboratories, CO and CO_2 were measured continuously by Horiba nondispersive infrared gas analyzers and O_2 was measured continuously by a Lynn electrochemical oxygen analyzer. Even though the material contained nitrogen, concentrations of hydrogen cyanide generated during these experiments were not measured.

[2] Certain commercial equipment, instruments, or materials are identified in this paper to specify adequately the experimental procedure. Such identification does not imply recommendation or endorsement by the National Institute of Standards and Technology, nor does it imply that the materials or equipment identified are necessarily the best available for the purpose.

[3] The absolute gas concentrations reported in this paper depend upon the analytical instruments used in measuring the specific gas species and the instruments' response times.

2.4 Comparison Factors in the Development of this SRM

2.4.1 Interlaboratory Evaluation To ascertain the reproducibility across different laboratories, four laboratories (in addition to the University of Pittsburgh) were asked to participate in an interlaboratory evaluation of nylon 6/6 (lot 1). These laboratories were Anderson Laboratories (Dedham, MA), Southwest Research Institute (San Antonio, TX), U.S. Testing Co., Inc. (Hoboken, NJ), and Weyerhaeuser Company (Longview, WA).

2.4.2 Intralaboratory Evaluation The University of Pittsburgh examined the repeatability of the LC_{50} for both lots of nylon 6/6. Three separate LC_{50} values were determined for nylon 6/6 (lot 1) and four LC_{50} values for lot 2. In addition, two separate samples from lot 2 were sent to Anderson Laboratories which determined two LC_{50} values.

2.5 Statistical Analysis of Results

For this SRM, two types of statistical uncertainties, a 95% *confidence* interval and a 95% *prediction* interval, were determined. The 95% confidence interval defines the precision with which the true endpoint (the LC_{50}) is known; whereas, the 95% prediction interval provides the numerical bound in which the next LC_{50} should fall if the experiments are conducted correctly. Unlike a 95% confidence interval, a 95% prediction interval does not get appreciably narrower if more laboratories participate in the study, since the 95% prediction interval will always be larger than the interlaboratory standard deviation. The difference between these two intervals is illustrated below for the simplified case in which each of "n" laboratories would determine one LC_{50} value.

The uncertainty based on a 95% confidence interval for the true LC_{50} is shown in Eq. (1).

$$t_{n-1}(0.025)\sqrt{\frac{\text{interlab variance}}{n}} \tag{1}$$

where $t_{n-1}(0.025)$ is the appropriate cutoff from the student's t distribution for a two sided interval with a 95% confidence level [17].

The uncertainty based on a 95% prediction interval, using data from the same simple case as above, would be determined by Eq. (2) [18]. This calculation incorporates the variance of a single new determination of the LC_{50} value plus the variance of the mean.

$$t_{n-1}(0.025)\sqrt{\frac{(n+1)}{n}\,\text{interlab variance}} \tag{2}$$

Since we had limited data on the SRM material (only two laboratories evaluated it), we estimated the variability in the certified LC_{50} using data from the interlaboratory study (on lot 1) as well as the data on the SRM (lot 2). Analysis of these data showed that the variability between laboratories was larger than the variability within the laboratories. These data could be pooled since the two lots of nylon 6/6 were considered fairly similar based on the material composition and the expectation that the measurement errors made by the laboratories would follow the same distribution for both lots. In addition, an Analysis of Variance indicated that there was no statistically significant difference between the mean LC_{50} of lot 1 and that of lot 2. The interlaboratory and intralaboratory variance components were estimated from an analysis of variance on both materials simultaneously. The variance of the mean LC_{50} value for the SRM is given in Eq. (3):

$$\frac{1}{2}\,\text{interlab variance} + \frac{3}{16}\,\text{within-lab variance} \tag{3}$$

and the effective degrees of freedom for this variance are 4.9. Therefore, the uncertainty based on a 95% confidence interval for the mean is shown in Eq. (4):

$$t_{4.9}(0.025)\sqrt{\frac{1}{2}\,\text{interlab variance} + \frac{3}{16}\,\text{within-lab variance}} \tag{4}$$

The variance of a single new LC_{50} plus the variance of the mean is shown in Eq. (5):

$$\frac{3}{2}\,\text{interlab variance} + \frac{19}{16}\,\text{within-lab variance} \tag{5}$$

and the effective degrees of freedom for this sum are 5.3. Therefore, the uncertainty based on a 95% prediction interval is seen in Eq. (6):

$$t_{5.3}(0.025)\sqrt{\frac{3}{2}\,\text{interlab variance} + \frac{19}{16}\,\text{within-lab variance}} \tag{6}$$

3. Results

3.1 Interlaboratory Evaluation

The toxicological data for nylon 6/6 (lot 1) provided by the participating laboratories in the interlaboratory evaluation are given in Table 1.

3.2 Intralaboratory Evaluation

The toxicological and chemical data for nylon 6/6 (lot 2) obtained at the University of Pittsburgh and Anderson Laboratories are given in Tables 2 and 3, respectively. The LC_{50} values of four separate samples (bottles 10, 20, 30, and 40) of lot 2 were determined by the University of Pittsburgh. Two additional LC_{50} values were obtained for two samples of lot 2 (bottles 20 and 30) by Anderson Laboratories. The material mass loss, evolution of CO and CO_2, and reduction of O_2 found in tests conducted by the University of Pittsburgh at or close to the LC_{50} values are illustrated in Figs. 2 to 5. These four figures also show the temperatures at which the material decomposition began and when flaming ignition occurred, and the temperatures at which animal exposure was initiated as well as the temperature at the time 50% of the animals died (LT_{50}).

Table 1. Interlaboratory evaluation of nylon 6/6 (lot 1) toxicological data

Laboratory	LC_{50} values (g)	Mean LC_{50} values (g)
Univ. of Pittsburgh	4.8 (4.2–5.3)[a]	5.2
	5.2 (4.8–5.7)	
	5.7 (5.3–6.2)	
1	3.6 (3.6–3.6)	3.8
	3.7 (3.1–4.6)	
	4.1 (3.3–5.0)	
2	6.1 (6.0–6.2)	6.6
	7.1 (6.7–8.0)	
3	5.4 (4.8–6.1)	
	5.4 (4.8–6.1)	
4	4.3 (3.6–5.4)	4.3
Overall mean ±95% confidence interval[b]		5.1 ± 1.2

[a] 95% confidence limits of the LC_{50} values.
[b] Mean of all the laboratories' mean values. The 95% confidence interval incorporates both the within-laboratory and the between-laboratory variation.

Table 2. Intralaboratory evaluation of nylon 6/6 (lot 2) toxicological data

Laboratory	Bottle No.	LC_{50} values (95% confidence limits) (g)	Mean LC_{50} value (g)
U. Pitt.	10	3.6 (ND)	
	20	3.9 (3.7–3.9)	3.7
	30	3.6 (3.5–3.7)	
	40	3.9 (3.9–4.0)	
Anderson	20	5.1 (4.5–5.8)	5.1
	30	5.15[a] (5.1[b]–5.2[c])	
Overall mean ±95% confidence interval			4.4 ± 1.9[d]

[a] Midpoint between values in parenthesis
[b] No deaths at this mass loading
[c] 100% deaths at this mass loading
[d] The overall mean is based on the mean values from the two laboratories; The 95% confidence interval incorporates both the within and between laboratory variation.
ND—not determined.

Table 3. Intralaboratory evaluation of nylon 6/6 (lot 2) physical and chemical data[a]

Laboratory	Bottle No.	Temp. initial exposure (°C)	Temp. during flaming (°C)	Time of flaming[b] (min)	Max CO (%)	Time max CO (min)	Max CO_2 (%)	Time max CO_2 (min)	Minimum O_2 (%)	Time minimum O_2 (min)
Univ. of Pittsburgh	10	410	431–513	1.5	0.64	3	7.5	3	13	3
	20	415	448–531	1.7	2.8	3.5	ND	ND	ND	ND
	30	410	447–536	2.0	0.90	3.5	ND	ND	ND	ND
	40	415	441–531	1.3	1.1	4.5	ND	ND	ND	ND
Anderson	20	409	434–612	NR	1.2	NR	7.0	NR	11.6	NR
	30	401	435–601	NR	1.2	NR	7.6	NR	11.8	NR

[a] Values in table are from experiments conducted at a concentration equivalent to the LC_{50} value.
[b] Time that material started flaming where the beginning of the animal exposure is 0 time.
ND—not determined.
NR—not reported.

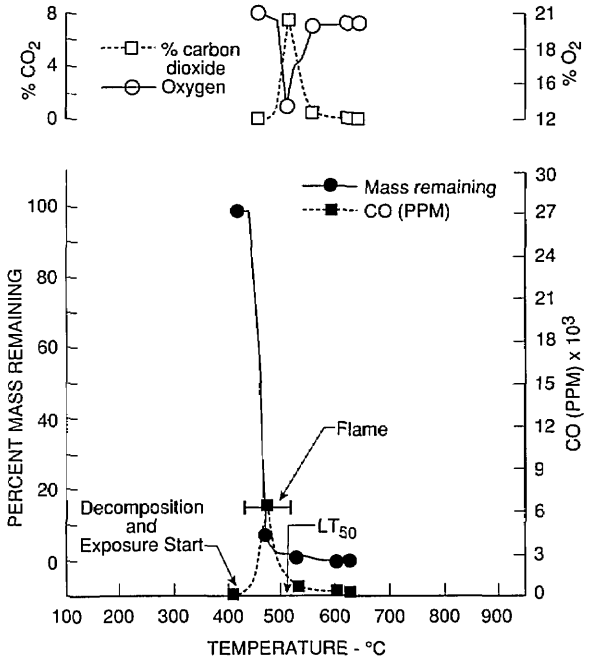

Fig. 2. Gas concentrations and percent mass remaining as furnace temperatures increased during the decomposition of nylon 6/6 (lot 2) from bottle No. 10. The initial mass of nylon 6/6 was 3.6 g (the LC_{50} value).

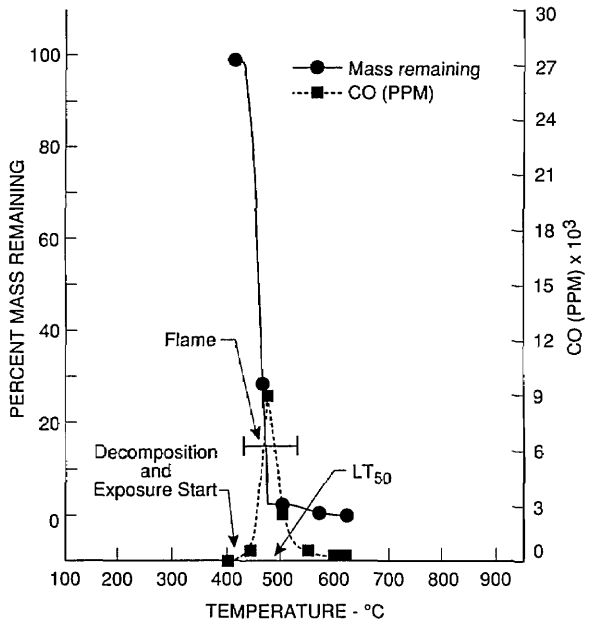

Fig. 4. Carbon monoxide concentrations and percent mass remaining as furnace temperatures increased during the decomposition of nylon 6/6 (lot 2) from bottle No. 30. The initial mass of nylon 6/6 was 3.6 g (the LC_{50} value).

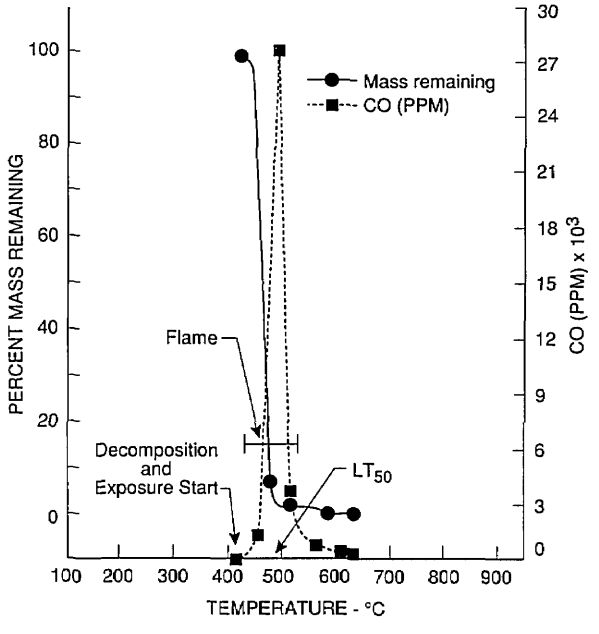

Fig. 3. Carbon monoxide concentrations and percent mass remaining as furnace temperatures increased during the decomposition of nylon 6/6 (lot 2) from bottle No. 20. The initial mass of nylon 6/6 was 3.9 g (the LC_{50} value).

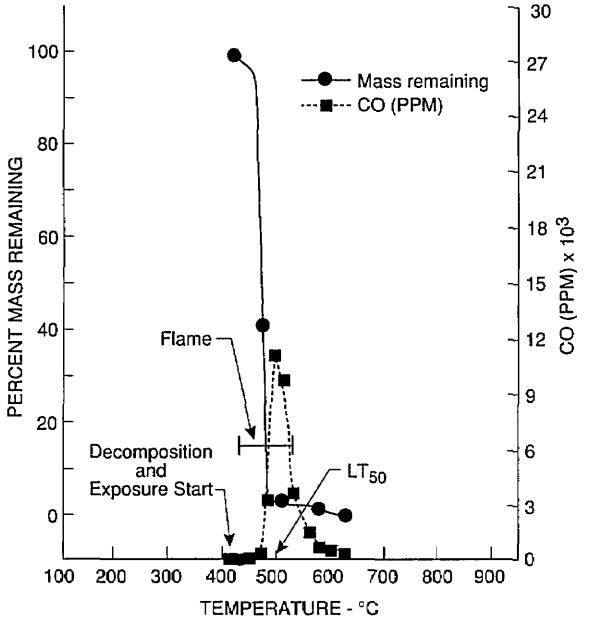

Fig. 5. Carbon monoxide concentrations and percent mass remaining as furnace temperatures increased during the decomposition of nylon 6/6 (lot 2) from bottle No. 40. The initial mass of nylon 6/6 was 3.9 g (the LC_{50} value).

4. Discussion

The development of a standard reference material requires the statistical determination of a certified value (in this case, the LC_{50} of the material) and an uncertainty which informs the user how well the certified value is known. For most standard reference materials, this uncertainty is defined by the 95% *confidence* interval, which, in the example of SRM 1049, would tell the user how precisely the true LC_{50} value is known (with 95% confidence). However, for this SRM, we have determined the 95% *prediction* interval rather than the 95% confidence interval. The 95% prediction interval tells the user the numerical bound in which the next LC_{50} value should fall assuming the experiments are conducted correctly and instruments are functioning properly. A confidence interval is narrower than a prediction interval and will get narrower as the number of participating laboratories increases. Even if the user's system is operating correctly and his precision is comparable to the precision found in the research reported here, the next LC_{50} value could reasonably fall in a much larger range than that given by the confidence interval. On the other hand, the 95% prediction interval will not get smaller than the precision of a single measurement and thus allows the user to judge if the next experimental value obtained in his laboratory is in the right range.

The mean LC_{50} value of SRM 1049 (nylon 6/6; lot 2) is 4.4 g; its 95% confidence interval is ± 1.9 g; whereas, its 95% prediction interval is ± 3.4 g. This 95% prediction interval incorporates the variability from both the within-laboratory experiments and the interlaboratory evaluation of nylon 6/6. Therefore, if the user's precision is comparable to the precision found in the data in this report and the test procedure is being conducted correctly, the 95% prediction interval should include the user's next LC_{50} measurement.

5. Conclusions

A standard reference material (SRM 1049) has been developed for calibration of the University of Pittsburgh smoke toxicity method for assessing the acute inhalation toxicity of combustion products. The certified material is a nylon 6/6 and the certified LC_{50} value was based on four series of tests conducted at the University of Pittsburgh and two series of tests conducted at Anderson Laboratories. The 95% prediction interval is based on the variability of results found in both interlaboratory and intralaboratory evaluations. The certified LC_{50} value and 95% prediction interval is 4.4 ± 3.4 g. If a laboratory were to test this SRM under their conditions in their apparatus and found the LC_{50} value to fall within the certified 95% prediction interval, the probability is good that their equipment is functioning appropriately and that the test is being conducted correctly.

Acknowledgment

The participation of Anderson Laboratories, Inc. (Dedham, MA), Southwest Research Institute (San Antonio, TX), University of Pittsburgh (Pittsburgh, PA), U.S. Testing Co., Inc. (Hoboken, NJ), and Weyerhaeuser Co. (Longview, WA) in the interlaboratory evaluation is greatly appreciated.

6. References

[1] America Burning, Report of the National Commission on Fire Prevention and Control, U.S. Government Printing Office, Washington, DC, 1973.

[2] H. L. Kaplan, A. F. Grand, and G. E. Hartzell, Combustion Toxicology, Principles and Test Methods, Technomic Publishing Co., Inc., Lancaster, PA (1983).

[3] R. C. Anderson, P. A. Croce, F. G. Feeley, III, and J. D. Sakura, Study to Assess the Feasibility of Incorporating Combustion Toxicity Requirements into Building Material and Furnishing Codes of New York State. Final report to Department of State, Office of Fire Prevention and Control, Albany, New York, From Arthur D. Little, Inc., Cambridge, MA, Ref. No. 88712, (May 1983).

[4] Y. C. Alarie and R. C. Anderson, Toxicologic and Acute Lethal Hazard Evaluation of Thermal Decomposition Products of Synthetic and Natural Polymers, Tox. Appl. Pharm. **51**, 341–362 (1979).

[5] Y. C. Alarie and R. C. Anderson, Toxicologic Classification of Thermal Decomposition Products of Synthetic and Natural Polymers, Tox. Appl. Pharm. **57**, 181–188 (1981).

[6] B. C. Levin, A. J. Fowell, M. M. Birky, M. Paabo, A. Stolte, and D. Malek, Further Development of a Test Method for the Assessment of the Acute Inhalation Toxicity of Combustion Products, NBSIR 82-2532, Natl. Bur. Stand. (U.S.) (1982).

[7] New York State Uniform Fire Prevention and Building Code, Article 15, Part 1120, Combustion Toxicity Testing and Regulations for Implementing Building Materials and Finishes; Fire Gas Toxicity Data File. New York State, Department of State, Office of Fire Prevention and Control, Albany, NY 12231 (December 16, 1986).

[8] D. J. Caldwell and Y. C. Alarie, A Method to Determine the Potential Toxicity of Smoke from Burning Polymers: I. Experiments with Douglas Fir, J. Fire Sci. **8**, 23–62 (1990).

[9] D. J Caldwell and Y. C. Alarie, A Method to Determine the Potential Toxicity of Smoke from Burning Polymers: II. The Toxicity of Smoke from Douglas Fir, J. Fire Sci. **8**, 275–309 (1990).

[10] D. J. Caldwell and Y. C. Alarie, A Method to Determine the Potential Toxicity of Smoke from Burning Polymers: III. Comparison of Synthetic Polymers to Douglas Fir

Using the UPitt II Flaming Combustion/Toxicity of Smoke Apparatus, J. Fire Sci. 9, 470–518 (1991).
[11] V. Babrauskas, R. H. Harris, Jr., E. Braun, B. C. Levin, M. Paabo, and R. G. Gann, The Role of Bench-Scale Test Data in Assessing Full-Scale Fire Toxicity, NIST Tech. Note 1284, Natl. Inst. Stand. Technol. (1991).
[12] V. Babrauskas, B. C. Levin, R. G. Gann, M. Paabo, R. H. Harris, Jr., R. D. Peacock, and S. Yusa, Toxic Potency Measurement for Fire Hazard Analysis, NIST Special Publication 827, Natl. Inst. Stand. Technol. (1991).
[13] J. C. Norris, National Institute of Building Sciences Combustion Toxicity Hazard Test, in Proceedings of the Joint Meeting of the Fire Retardant Chemicals Association and the Society of Plastics Engineers, Grenelefe, FL (March 1988) pp. 146–155.
[14] H. J. Roux, The NIBS SMOTOX WG Program, Proceedings of the 37th International Wire and Cable Symposium, Reno, NV (November 1988) pp. 543–545.
[15] B. C. Levin, M. Paabo, and S. B. Schiller, A Standard Reference Material for Calibration of the Cup Furnace Toxicity Method for Assessing the Acute Inhalation Toxicity of Combustion Products, J. Res. Natl. Inst. Stand. Technol. **96**, 741–755 (1991).
[16] C. S Weil, Tables for Convenient Calculation of Median-Effective Dose (LD_{50} or ED_{50}) and Instructions in Their Use, Biometrics **8**, 249–262 (1952).
[17] M. Natrella, Experimental Statistics. NBS Handbook 91, Natl. Bur. Stand. (U.S.) (1966).
[18] G. A.Whitmore, Prediction Limits for a Univariate Normal Observation, Am. Statistician **40**, 143–145 (1986).

About the authors: *Barbara C. Levin is a Project Leader and Toxicologist in the Fire Hazard Analysis Group in the Building and Fire Research Laboratory at the National Institute of Standards and Technology. She is also an Adjunct Professor in the Fire Protection Engineering Department at the University of Maryland, College Park, Maryland. Yves Alarie is a Full Professor of Respiratory Physiology and Toxicology in the Department of Environmental and Occupational Health, University of Pittsburgh Graduate School of Public Health. Maryanne F. Stock is a Senior Research Specialist in Combustion and Inhalation Toxicology in the Department of Environmental and Occupational Health at the University of Pittsburgh Graduate School of Public Health. Susannah B. Schiller is a statistician in the Computing and Applied Mathematics Laboratory at the National Institute of Standards and Technology. The National Institute of Standards and Technology is an agency of the Technology Administration, U.S. Department of Commerce.*

Volume 97, Number 2, March–April 1992
Journal of Research of the National Institute of Standards and Technology

[J. Res. Natl. Inst. Stand. Technol. 97, 253 (1992)]

Certification of NIST SRM 1962: 3 μm Diameter Polystyrene Spheres

Volume 97 | Number 2 | March–April 1992

Arie W. Hartman, Theodore D. Doiron, and Joseph Fu

National Institute of Standards and Technology,
Gaithersburg, MD 20899

This report describes the certification of SRM 1962, a NIST Standard Reference Material for particle diameter. It consists of an aqueous suspension of monosize 3 μm polystyrene spheres. Two calibration techniques were used: optical microscopy and electron microscopy. The first one gave a mean diameter of $\bar{D} = 2.977 \pm 0.011$ μm and a standard deviation of the size distribution $\sigma_D = 0.020$ μm, based on measurement of 4600 spheres. The second technique gave $\bar{D} = 2.990 \pm 0.009$ μm, based on measurement of 120 spheres. The reported value covering the two results is $\bar{D} = 2.983$ μm with a maximum uncertainty of 0.016 μm, with $\sigma_D = 0.020$ μm.

Key words: electron microscopy; microspheres; optical microscopy; particle sizing; polystyrene; standard reference materials.

Accepted: September 16, 1991

1. Introduction and Summary

This report contains the procedures, measurement results, and error analysis for the certification of SRM 1962, a Standard Reference Material (SRM) for particle diameter. The SRM consists of a 0.5% aqueous suspension of monosize polystyrene microspheres with a mean diameter of nominal 3 μm.

The calibration was carried out by two independent methods: specialized forms of optical and electron microscopy. The two methods are described in Sec. 2, the measurement results are shown in Sec. 3, and the error analysis is given in Sec. 4.

The results of the calibration are as follows:

Optical microscopy:

Mean diameter: $\bar{D} = 2.977 \pm 0.011$ μm

Diameter distribution: Gaussian from 10 to 90%

Standard deviation $\sigma_D = 0.020$ μm

Number of outliers (defined here as $|D - \bar{D}| > 4\,\sigma_D$):

< 0.5% for oversize

nil for undersize

Seven samples totaling over 4600 spheres were measured.

Electron microscopy:

Mean diameter: $\bar{D} = 2.989 \pm 0.009$ μm

Reported mean diameter value: $\bar{D} = 2.982 \pm 0.016$ μm.

2. Methods

The two methods used in the calibration of SRM 1962 are described in this section.

2.1 Optical Microscopy (CDF)

A drop of microsphere suspension is placed on a microscope slide, and allowed to flow out and dry.

During drying the drop breaks up into numerous smaller droplets that dry individually. The spheres that these droplets contain are pulled together by surface tension forces, resulting in strands and small clusters of contacting spheres (Fig. 1). The contacting spheres are illuminated in the microscope by near-parallel light (condenser stopped down), and a number of small and circular "focal spots" form in the common back focal plane, as shown in Fig. 2. When a photomicrograph is taken of this back-focal plane, each recorded spot marks a sphere center. The distances C between adjacent spots represent the sum of two sphere radii. If the sphere diameters D are distributed normally (Gaussian), the C-values will also be distributed normally. The mean value $\bar{C}$ then equals $\bar{D}$ and the standard deviation σ_C of the C-distribution equals $\sigma_D/\sqrt{2}$. In this way $\bar{D}$ and σ_D are found. This technique is called Center Distance Finding, or CDF [1].

The photographed focal spots are small (about 0.5–0.6 μm in the object plane), uniform and circular, permitting center distances C to be measured with high precision: a few hundredths of a micrometer in the object plane. It thus allows a measurement of the diameter distribution, which would be difficult to do from measurements of the sphere images themselves.

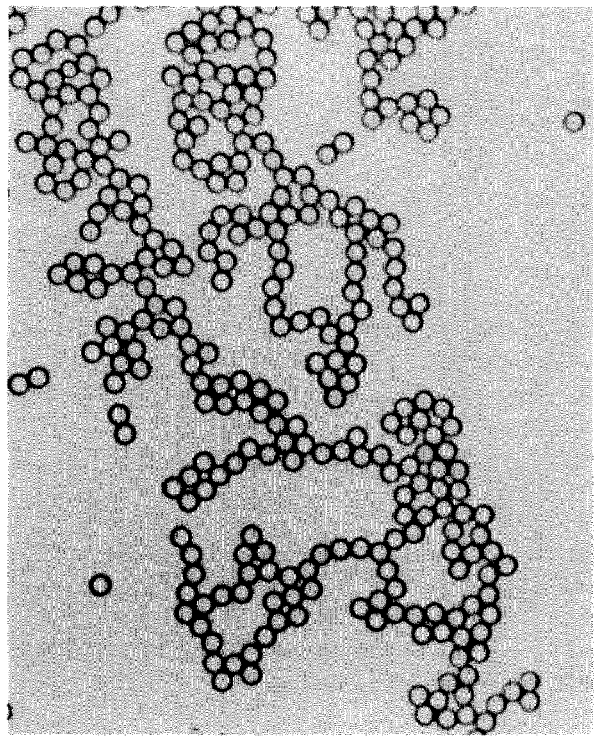

Fig. 1. Strands and clusters of 3 μm spheres.

To make the CDF measurements a number of microsphere slides are prepared and photographed. A large number of photographs are measured under computer control (see Appendix A). The film scale (image magnification) is measured, as outlined in Appendix B. The image distortion, which for high-quality optics is a function of off-axis distance only, is measured also (see Appendix B). The computer then applies a radial correction to each measured focal spot position. The corrected center distances C are determined, which leads to $\bar{D}$ and σ_D.

2.2 Electron Microscopy (MEM)

With this method, called Metrology Electron Microscopy or MEM, the focused beam of a scanning electron microscope (SEM) is held stationary while a single-axis scanning stage with interferometric position readout moves the specimen such that the focused electron beam traverses the distance between leading and trailing edge of the sample to be measured. In our case the sample consists of a straight row of equal-size microspheres.

An interferometer system measures stage travel versus time during a constant-speed scan, and the secondary electron detection system measures the electron output varying with time, all under computer control. The two data streams are combined resulting in a value for the length of the measured microsphere row, from which an average sphere diameter is found. The operation resembles that of an optical measuring microscope, where a set of crosshairs defines a stationary reference point in the field of view and a micrometer screw measures stage travel. See also Refs. [2] and [3].

3. Measurements

In this section details are given of the specimen preparation, data collection and reduction, and the measurement results. Section 3.1 covers optical microscopy, Sec. 3.2 treats electron microscopy.

3.1 Optical Microscopy (CDF)

Four samples were taken from one vial of SRM 1962 microsphere suspension, and one sample from each of three other vials. The vial contents were homogenized by rolling and shaking for 2 min, prior to dispensing a drop of suspension for analysis.

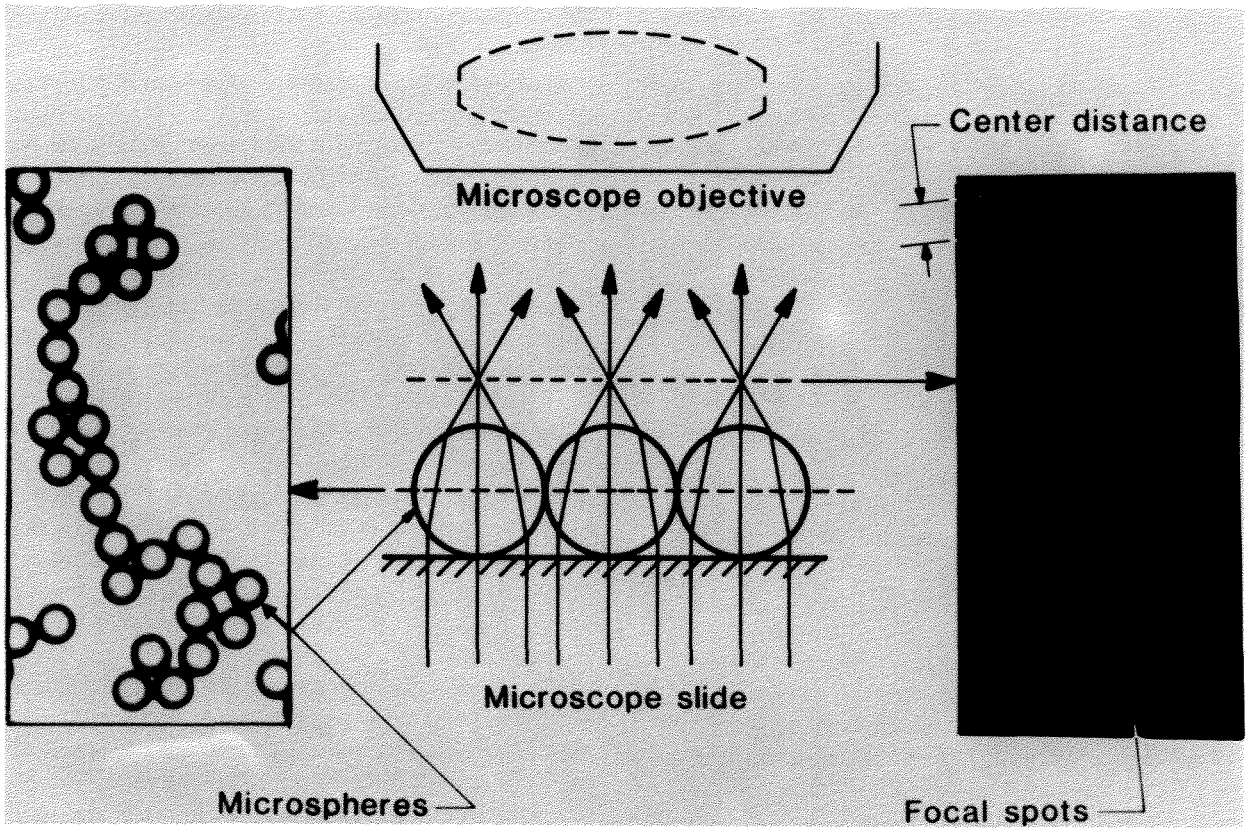

Fig. 2. The CDF microsphere sizing scheme.

The microscope used was an Olympus Model BH-2[1] with a 100×/0.90NA objective, producing images with 1000× magnification on 4×5 in Polaroid sheet film.

Focal-spot patterns from the contacting microsphere structures were photographed on Type 57 positive film. This high-speed material (3000 ASA) has adequate dimensional stability [1] and low granularity, permitting its use for this SRM calibration. Seventy-six photographs were measured, containing over 4600 measured focal spots. The measurement path through each microsphere grouping was selected such that each sphere was measured only once. The groupings of contacting spheres were examined first for overdeterminedness, to indicate where small air gaps between apparently contacting spheres could have formed during the drying process. Such gaps have minimum widths ranging from zero to typically one σ_D.

[1] Certain commercial equipment, instruments, or materials are identified in this paper to specify adequately the experimental procedure. Such identification does not imply recommendation or endorsement by the National Institute of Standards and Technology, nor does it imply that the materials or equipment identified are necessarily the best available for the purpose.

Air-gap formation can occur in contacting microsphere groupings, such as hexagonal arrays where six neighboring spheres surround a center sphere while the spheres have slightly different diameters [4,5]. Such overdetermined sphere groupings were avoided in the measurement phase. An example of a selected measurement path is given in Fig. 3.

The measured photographs had a print magnification of nominal 1000×. The measured focal spots had 0.5–0.6 mm diameters, their 3 mm center spacings were measured with 0.01 mm resolution. The microscope image calibration for magnification and image distortion is detailed in sec. 4.1.1 and in Appendix B.

Measurement results are given in Table 1 and in Fig. 4. The data were originally plotted with center distances as the horizontal axis. This was then converted into a diameter scale by compressing the horizontal scale by $\sqrt{2}$ to reflect the fact that for normal distributions $\sigma_D = \sigma_C \sqrt{2}$, and by centering the D-scale such that the mean diameter $\bar{D}$ coincides with the mean center distance $\bar{C}$. The resulting "diameter distribution" of Fig. 4a already implies that this distribution is considered a normal one. The information extracted from Fig. 4 is:

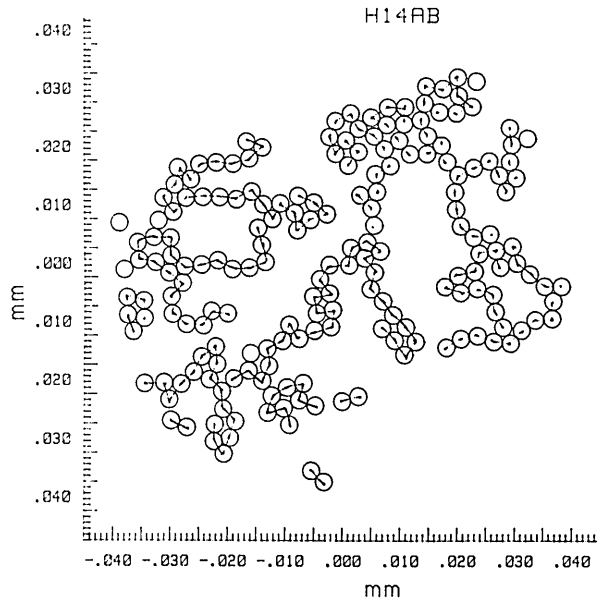

Fig. 3. Measurement path for a sphere grouping.

a) the median diameter (which corresponds with the average diameter $\bar{D}$ if the distribution is normal), b) the diameter range over which it actually is normal, and c) the value for the standard deviation σ_D associated with that diameter range.

3.2 Electron Microscopy (MEM)

The contents of an SRM 1962 vial were homogenized by rolling and shaking for 2 min. Then a drop was taken from the vial, diluted in 50 ml of 18 MΩ cm deionized water, and washed three times to reduce the amount of dissolved material remaining (biocide). Each washing cycle involved low-power ultrasonication, settling and decanting four-fifths of the clear liquid. A small drop of the final suspension was placed on three microscope slides and air dried, causing formation of single-layer arrays with hexagonal ordering. The slides were then coated with about 30 nm of amorphous carbon to minimize charging in the electron beam. With this technique the formation of sphere arrays was sought, as opposed to the case of CDF (see Sec. 4.2.1).

The electron microscope used for the microsphere diameter measurements is a Vacuum Generators VG HB-50A scanning electron microscope. It has in the secondary electron imaging mode an edge resolution of 0.03 μm at 30 keV and a 25 mm working distance. The interferometer is a single-pass polarization Michelson type, mounted in the SEM vacuum on the fixed and moving parts of a piezo-electric scanning stage. The two reflectors are corner cube prisms to accommodate the relatively long distance (some 80 cm) from the stage inside the SEM column to the interferometer readout system outside. The scanning stage is placed on top of the X-Y stage in the SEM. The X-Y stage is used for searching.

The interferometer readout is a Hewlett-Packard Model 5526A, utilizing a two-frequency stabilized He-Ne laser and a heterodyne scheme for measuring optical path differences. The two reflectors are mounted in the SEM vacuum on the fixed and moving parts of the piezo-electric one-axis scanning stage. The reflectors are corner cube prisms, to accommodate any misalignment over the relatively long distance (some 80 cm) from the stage inside the SEM column to the interferometer readout system outside. A block diagram of the MEM system is given in Fig. 5.

Forty microspheres were measured on each of three slides, selecting array rows that were essentially parallel to the scanning stage axis. The rows were at least 12 spheres long allowing measurement of the spacing between two contact planes separated by 10 spheres, from which an average sphere

Table 1. Measurement results with optical microscopy[a]

Vial #	Sample #	Sphere diameter (μm)	# of measurements	# of photographs
1	1	2.975	1092	15
1	2	2.972	571	9
1	3	2.974	475	11
1	4	2.975	501	17
1	1 to 4	2.974	2639	52
2	5	2.978	720	11
3	6	2.975	214	4
4	7	2.975	1061	9
all	all	2.975	4634	76

[a] Diameter distribution is approximately normal for 10 to 90%. Standard deviation over this interval: 0.021 μm.

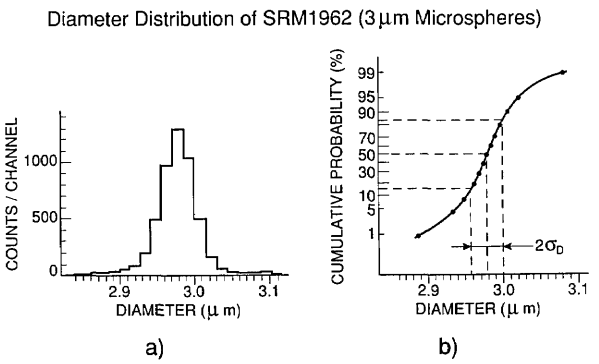

Fig. 4. SRM 1962: a) diameter distribution; b) cumulative distribution.

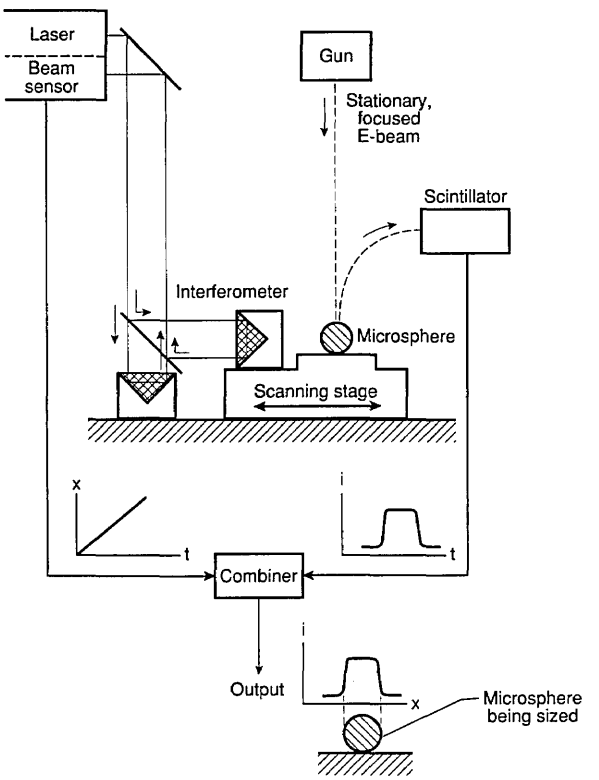

Fig. 5. Diagram of the Metrology Electron Microscope (MEM).

diameter was calculated. Visibly obvious outliers were excluded from the measurements. After each computer-controlled scan along a microsphere row the microscope was reverted to scan mode (SEM mode) and the next sphere row positioned manually for a line scan (spot mode). The scans were 60 μm long, with the secondary electron intensity profile being sampled at 2000 equispaced points. Each minimum in SEM output current signals the passing of a contact plane between two touching spheres (see Fig. 6). Each minimum fell within one data point spacing. Measurement results are given in Table 2.

4. Error Analysis

In this section sources of uncertainty (called "errors" for short) are identified and evaluated for the two microsphere size measurement techniques. They are expressed as "3 σ" or "maximum" errors as indicated, the individual independent contributions are summed in quadrature, and the total systematic and random errors are added linearly to form "the uncertainty" of the measurement process (see also Tables 3 and 4).

4.1 Errors in Optical Microscopy

The errors in measuring the average diameter can be arranged in three groups: errors associated with finding the image magnification of the measured photographs, errors associated with measuring photographed focal spot spacings (center distances between contacting spheres), and errors associated with the diameter distribution. To find estimates for the first two errors, five repeat photographs were taken. Averaging of the repeat data was done to find the magnification at lower uncertainty, while comparison between the photographs was used to find scatter in measured focal spot spacings from which uncertainties in the magnification and in a single measurement of center distance can be derived. The three groups of errors are discussed separately.

4.1.1 Errors Associated with Image Magnification The print magnification was found by photographing an interferometrically calibrated chrome-on-glass stage micrometer (NIST No. 5525). The line center spacings were measured on a SGIP Universal Measuring Machine, Model MU-214B. The measured and averaged lengths are corrected for image distortion which had been measured separately (Appendix B). The result was an image magnification value valid over the whole field of view, this value is equal to the on-axis value prior to image distortion removal. A number of error sources affected the result, as detailed below.

a) The object micrometer.

A length 2.10–2.20 mm of the micrometer mentioned before was used. The length of segment 0–2.11 mm is 2100.58 μm with a maximum error of 0.17 μm, that of segment 0–2.20 mm was 2199.51 ± 0.11 μm, giving for 2.11–2.20 mm a

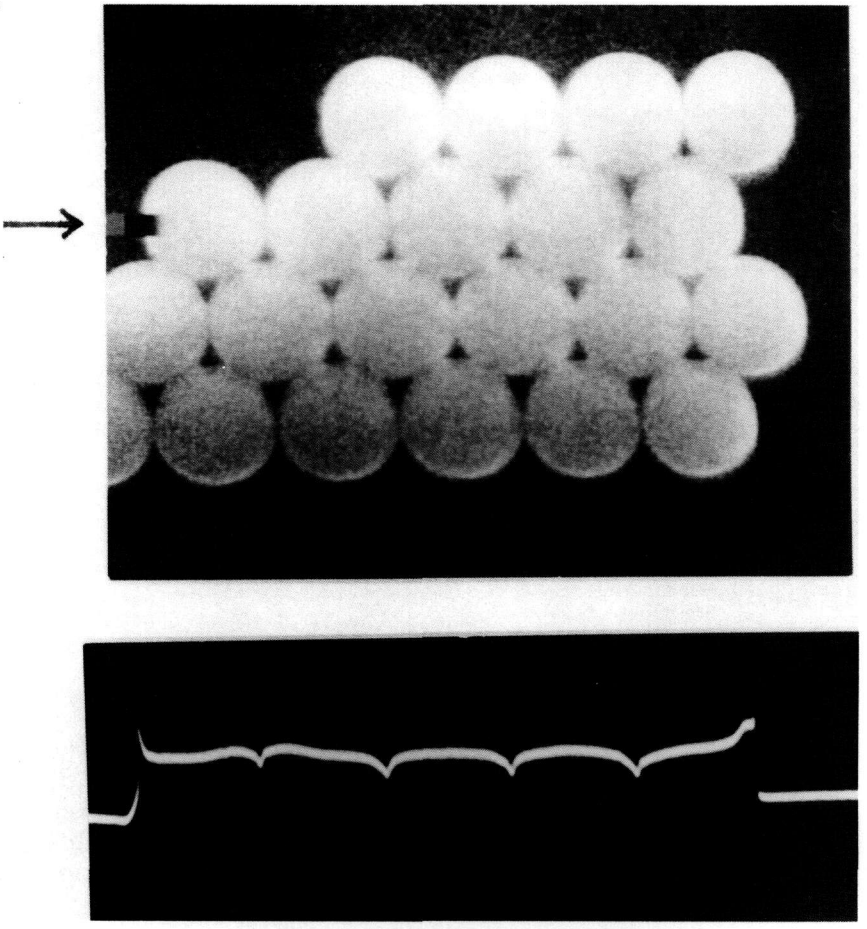

Fig. 6. Measuring microspheres with MEM.

Table 2. Measurement results with electron microscopy

Microsphere row #	Average diameter (μm)
1	3.008
2	3.000
3	3.000
4	2.998
5	3.003
6	2.993
7	2.996
8	2.997
9	2.997
10	2.981
11	2.994
12	2.996
Average	2.997

length 88.93 ± 0.20 μm. This corresponds to $\pm 0.227\%$ or 0.0068 μm for a 3 μm length in the object plane, a systematic error.

b) The SGIP film measuring machine.

The scale error amounted to approximately 1.3 μm maximum per setting, or about 2 μm for a difference between two settings. For the measured film distances (89.271 mm mean value) this amounts to about 0.002% or 0.0001 μm in the object plane, a systematic error.

c) Film emulsion shifts, image magnification scatter, and film readout errors.

Polaroid Type 57 positive film exhibits local random emulsion shifts, like most photographic emulsions. These lateral shifts are caused by non-uniform film processing and drying.

Magnification scatter is caused by slight changes in film position in the cassette (measured along the optical axis) when exposed film is replaced by a new film sheet.

Film readout errors reflect the precision with which one can visually pinpoint the center position of the scale division lines of the photographed object micrometer.

The combined contribution by these three error sources was found as follows. The utilized 0.09 mm section of the calibrated object micrometer was photographed five times at 1000×, giving image lengths (in mm): 89.807, 89.924, 89.863, 89.903, and

Table 3. Error budget for a single 3 μm center distance measurement, using CDF[a]

Category	Error source	Error contribution (μm) Systematic	Random
On-axis magnification	Stage micrometer calibration	0.0068	
	Film measuring machine calibration	0.0001	
	Film readout, emulsion shifts, and magnification scatter (5 exposures)	0.0053	
	Image distortion uncertainty	0.0020	
		0.0089	
Center distance measurement	Film readout and emulsion shifts		0.017
	Magnification scatter		0.008
	Image distortion-worst case		0.025
	Sphere flattening on contact		0.002
	Non-sphericity		0.030
	Subtotals	0.0089	0.043
Finite sample size ($N = 4600$)	Diameter distribution width		0.095
	Totals	0.0089	0.104

[a] Uncertainty in $\bar{D}$/$0.0089 + 0.104/\sqrt{4600} = 0.011$ μm. Measured $\bar{D}$ (after correction, see Sec. 4.1.2): 2.977 μm.

Table 4. Error budget for an average diameter measurement of 3 μm spheres, using MEM[a]

Category	Error source	Error contribution (μm) Systematic	Random
Microsphere sensing	Imperfect scan conditions:		
	scan direction		0.0011
	unequal-size spheres		0.0002
	E-beam exposure	0.0009	
	SEM resolution and E-beam wander		0.0008
Row length measurements	Stage travel sampling		0.0009
	interferometer least count		0.0005
Microsphere grouping	Sphere flattening on contact	0.0020	
	air gaps between spheres	0.0020	
Sample size ($N = 120$)	Small sample with non-zero σ_D		0.0055
	Totals	0.0030	0.0057

[a] Uncertainty in $\bar{D}$: $0.0030 + 0.0057 = 0.009$ μm. Measured $\bar{D}$ (after corrections, see Sec. 4.2.5): 2.990 μm.

89.607. The mean was 89.837, with a 3 σ scatter of 0.142 mm or 0.159%. This total scatter contributes a 0.0048 μm error to a 3 μm center distance measurement. After correction for image distortion, see d) below, the mean becomes 89.271 mm, giving an on-axis image magnification $M_o = 89.271$ mm/ 88.93 μm = 1004×.

d) Image distortion.

The microscope used exhibits radial image distortion: each off-axis image point is shifted radially by a small amount from its intended position. In our case each end point of the 89 mm measured length was shifted outwards by 0.30 mm typically, with an estimated maximum uncertainty of 0.030 mm (Appendix B). This amounts to a combined 0.060 mm uncertainty in the measured length (the two error contributions are correlated), or 0.067%, corresponding to 0.0020 μm in the object plane.

The error contributions a) through d) combine to a total systematic error of 0.0089 μm (see Table 3).

4.1.2 Errors Associated With the Determination of Microsphere Center Distances The accuracy of center distance measurements is affected by various uncertainties: those associated with (a) pinpointing the positions of focal spot centers in the film, (b) with the correction of measured focal spot positions due to image distortion, (c) with the fluctuations in print magnification when new film is inserted in the cassette, (d) with possible distortion of the spheres at the contact areas, and (e) with the possibility that the individual spheres might be slightly deformed (showing a non-circular cross section when measured perpendicular to the line of sight).

a) The combined effect of film readout (pinpointing sphere centers) and emulsion shifts was found by taking three repeat exposures of a hexagonal array of the 3 μm spheres, and measuring each time the same 17 distances between adjacent sphere centers in a selected microsphere row, under computer control as described in Appendix A. All 17 sets of three center distance readings each were scaled down to the same average value (nominally 3.0 mm, as a result of 1000× magnification of the 3 μm sphere objects). The 51 values were then pooled, resulting in a 3 σ scatter of 17.3 μm which amounts to 0.017 μm in a 3 μm object distance, a random error. As can be seen, this procedure reduced the effects of magnification scatter and avoided the effects of off-axis magnification changes due to image distortion and of unequal-size spheres.

When pinpointing the center positions of the focal spot recordings in the film the utilized coordinate measuring machine with TV-microscope probe exhibited a reproducibility of better than 0.5 μm at 1 σ (see Appendix A). This translates to a maximum error of 2 μm in film distances between two focal spots, or 0.002 μm in distances between microsphere centers. This random error is included in the above error discussion, and does not noticeably increase the 0.017 μm random error calculated.

b) The effect of image distortion in our case (see Appendix B) is maximum for a sphere pair at the edge of the measured field of view. At 40 mm off-axis distance the maximum error in the measured image distortion is about ±20 μm, at 37 mm it is ±16 μ. Assuming as a worst case that these errors are uncorrelated, the resultant maximum error for 3 mm center distances near the edge of the 80 mm field of view will be ±25 μm or 0.025 μm in the object plane, a random error. For center distances closer to the optical axis this error will be considerably less, and for those on the axis the error will be zero.

c) Magnification scatter, occurring when replacing sheet film in the cassette, was measured as 0.27% at 3 σ for the central area of a single exposure (see Appendix B). This value is considerably larger than can be expected from the data in c) of Sec. 4.1.1. A reason is that c) relates to measurements near the edges of the film sheet (the imaged object micrometer segment filling the field of view), where it is clamped by the cassette mechanism and consequently flexes much less. The corresponding maximum error for a 3 μm center distance measurement is 0.008 μm, an essentially random error. It has been applied to all areas in the film, as a worst case.

d) One can adapt the model that two polystyrene spheres approaching each other during the drying process will finally be in intimate contact over a circular area, the extent of which is controlled by a balance between van der Waals attraction and elastic deformation. This model has been analyzed by Derjaguin et al.; they have derived an expression for the resultant sphere flattening [6]. For the present case the two-sided flattening would amount to a shortening ΔC of the measured center distance C given by

$$\Delta C = \frac{1}{8}\left[\frac{6(1-\eta^2)^2 DA^2}{\epsilon^4 E^2}\right]^{1/3}, \text{ in which}$$

η = Poisson constant, 0.3 for polystyrene
D = sphere diameter, 3×10^{-4} cm
A = Hamaker constant, 1×10^{-12} erg for polystyrene
E = Young's Modulus, 3×10^{10} dyne/cm^2 for polystyrene
ϵ = distance of closest approach, 3×10^{-8} cm.

This gives $\Delta C = 1.3$ nm $= 0.0013$ μm, lowering the measured diameter. If the selected values for A and E are each uncertain by a conceivable factor 2, then ΔC could change by a factor whose maximum value is $3\sqrt{16} = 2.5$. The ΔC estimate then ranges from 0.0005 to 0.003 μm.

Although this model for sphere flattening on contact is not the only one [7] available, experimental data (comparison with other calibration techniques for various monosize microsphere Standard Reference Materials) support the Derjaguin model. Therefore the measured diameter values in Table 1 are corrected afterwards by a somewhat arbitrary increase of 0.002 μm, and a systematic error 0.002 μm is entered in the Error Analysis.

e) If a microsphere is elongated perpendicular to the line of sight, its focal spot will be elongated by the same amount [1]. The photographed focal spots are almost all very uniform and circular, with a diameter of 0.4–0.5 mm in the film plane corresponding to 0.5 μm in the object plane. A non-circularity of 0.03 mm is visually detectable, and any residual non-sphericity will then not exceed 0.030 μm – a random error.

The random contributions combine to a maximum random error of 0.043 μm.

4.1.3 Errors Associated With the Microsphere Diameter Distribution Figure 4b shows that the diameter distribution is not quite normal. Of the measured population 98% covers the size range 2.89 to 3.08 μm. The maximum error contribution to a single center distance measurement can be set at ±0.095 μm – a random error.

4.1.4 Combining the Various Error Contributions for the $\bar{D}$ Measurement From Table 3 the total random error amounts to $0.104/\sqrt{4600} = 0.0015$ μm, the total systematic error is 0.0091 μm, therefore the total error in $\bar{D}$ is 0.011 μm, giving $\bar{D} = 2.977 \pm 0.011$ μm.

4.1.5 Finding the Standard Deviation σ_D of the Size Distribution Figure 4 shows that the diameter distribution is normal from 10 to 90% (3700 spheres), and the calculated value of σ_D for that population is 0.021 μm with a statistical uncertainty in σ_D of ±14% at 3 σ, or 0.003 μm.

Subtracting in quadrature the 1 σ random uncertainty in a single measurement of center distance (equal to 0.043/3 μm or 0.014 μm, see Table 3) would lower σ_D to 0.017 μm, but the uncertainty in this value will increase correspondingly.

The reported value for σ_D has been set at 0.020 μm.

4.2 Errors in Measuring Microsphere Average Diameter by Electron Microscopy

These error contributions can be divided into four groups: errors associated with the microsphere sensing process, errors associated with the measurement of scanning stage travel, errors associated with the kind of grouping the measured microspheres are in (single-layer microsphere arrays with hexagonal ordering), and errors associated with the microsphere diameter distribution width.

4.2.1 Errors Associated With Microsphere Sensing

a) Imperfect scan conditions.

Referring to Fig. 7, path 1 represents a possible scan path, while path 2 produces deeper minima of SEM output at the contact plane position midway of the line segments AB. When measuring contact plane spacings scan 2 gives no additional errors over scan 1.

When the scan path makes a small angle α (radians) with the center line, a cosine error occurs and the measured spacing is too large by a fraction $1/2\ \alpha^2$. A 10-sphere scan beginning at 1/2 R above the center line and ending at 1/2 R below it (a worst case), has $\alpha = 0.05$ and will have an error in the calculated scan length of 0.125% or 0.0375 μm. For 12 such scans, covering all 120 measured spheres, the random error in the calculated average diameter $\bar{D}$ is then $(0.0375\sqrt{12})/120$ μm, or 0.0011 μm.

If as a worst case two unequal-size contacting spheres have diameters 2% smaller than $\bar{D}$ and 2% larger than $\bar{D}$ respectively, the midpoint of the segment AB in Fig. 7 shifts a calculated $0.0014\bar{D}$ or 0.0042 μm. If this happens at both ends of the measured contact plane spacing containing N spheres, the maximum error in the calculated value for $\bar{D}$ is $0.0028\ \bar{D}/N$. In the present case all 12 measured rows contained 10 spheres each. When all data are pooled the resulting random maximum error in $\bar{D}$ will be $0.0028\ \bar{D}/(10\sqrt{12}) = 0.0002$ μm.

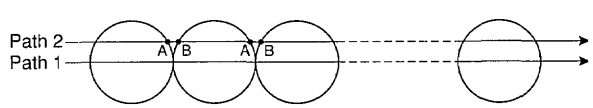

Fig. 7. Row length errors (see text).

b) E-beam exposure.

If E-beam exposure causes the polystyrene spheres to swell or shrink uniformly, the spheres could conceivably move with respect to each other and with respect to the substrate. A uniform swelling causes in principle increased contact area (sphere flattening) without changing sphere center distances, giving no measurement errors. A uniform shrinking causes in principle no errors if each sphere remains anchored to the substrate, while errors will occur if a sphere can move laterally (either by rolling over the substrate and sliding against its neighbor, or by sliding over the substrate while being in fixed contact with its neighbor).

Lateral sphere motions were not observed, and in a few cases development of a tiny "neck" or "bridge" was found between adjacent spheres, indicating that a uniform shrinking might be taking place there. Tentatively an upper limit of $0.005D$ has been placed on row end point shifts caused by sphere motions, leading to a maximum error of $0.01D$ in the measurement of a 10-sphere contact plane spacing and a systematic error of $0.01\bar{D}/(10\sqrt{12})$ or 0.0009 μm in the calculated $\bar{D}$-value covering 120 spheres.

c) SEM-resolution and E-beam wander.

The combined effect is estimated at 0.02 μm when pinpointing an individual contact plane or $0.02\sqrt{2}$ for a 10-sphere contact plane spacing. This gives for 120 spheres a random error in $\bar{D}$, equal to $0.02\sqrt{2}\times\sqrt{12}/120 = 0.0008$ μm.

4.2.2 Errors Associated With Stage Travel (Row Length) Measurements

a) Stage travel sampling.

Each scan is 60 μm long, and covers 2000 equally spaced data points for a least count of 0.033 μm. This gives a sampling error of 0.033 μm when measuring contact plane spacings. For 10-sphere rows and a total of 12 rows the resultant error in $\bar{D}$ becomes 0.0009 μm.

b) Interferometer digitizing.

The interferometer has a least count of $\lambda/40$, giving an error in contact plane spacing of $\lambda/40$ and a resultant error in $\bar{D}$ (using $\lambda = 0.6328$ μm, 10-sphere rows, and 12 rows total) equal to 0.0005 μm.

The errors associated with the electronics of SEM, interferometer, and computer, are considered negligible.

4.2.3 Errors Associated With Contacting Microsphere Groupings

a) Sphere deformation at the contact areas.

At the contact areas sphere flattening can occur as discussed in Sec. 4.1.2. It is in effect a change in scale, leading to a correction in the measured $\bar{D}$ set at +0.002 μm, and a systematic error of 0.002 μm.

b) Air gaps between spheres.

Hexagonal arrays of slightly unequal-size spheres exhibit small air gaps throughout the array; the average gap width for normal size distributions is about 0.46 times the standard deviation of the diameter distribution [2,3]. For this microsphere SRM $\sigma_D = 0.020$ μm as found in Sec. 3.1, leading to a diameter correction of $-0.46\ \sigma_D = -0.0090$ μm with an estimated systematic uncertainty of 0.0020 μm.

4.2.4 Errors Associated With Sample Size The maximum error in the measurement of average diameter of a microsphere material with $\sigma_D = 0.020$ μm based on a sample of 120 spheres, will be equal to $3\sigma_D/\sqrt{120} = 0.0055$ μm—a random error.

4.2.5 Combining the Various Error Contributions to $\bar{D}$ The total random error is found as a linear sum of the sampling and digitizing errors, plus an rms sum of the other random contributions, for a total of 0.0057 μm. The total systematic error is an rms sum of the individual contributions, amounting to 0.0030 μm. The reported total uncertainty in $\bar{D}$ is then 0.009 μm. The mean diameter itself, after applying the corrections for sphere flattening (+0.0020 μm) and air gaps (−0.0090 μm), is 2.990 μm.

5. Diameter Calibration Final Results

Optical Microscopy

Average diameter of SRM 1962 microspheres:

$\bar{D} = 2.977 \pm 0.011$ μm	(optical microscopy)
$\sigma_D = 0.020$ μm	(central peak)

Electron Microscopy

$\bar{D} = 2.990 \pm 0.009$ μm	(electron microscopy)

Because the two methods gave noticeably different $\bar{D}$-values and have almost the same total uncertainty, the reported value for the average diameter was set at $\bar{D} = 2.983 \pm 0.016$ μm.

The quoted uncertainties are maximum values.

6. Sample Uniformity

From Table 1 an impression of sample uniformity can be obtained: the within-vial variation in the measured mean diameter is less than ±0.1%,

and the between-vial variation amounts to a slightly larger (±0.10%) amount. Therefore, we take as an upper limit for the SRM non-uniformity: ±0.1% for within-vial and between-vial sampling.

7. Outliers

As with the sample uniformity, only upper limits could be set to the percent oversize and undersize of the measured 2000 spheres. When outliers are defined as spheres with sizes more than $4\sigma_D$ different from the average diameters, there are about 1% oversize and about 1% undersize (Fig. 4b). Spheres that were outsize by some 10% or more would be detectable by visual inspection of the photomicrographs. No such spheres were found.

8. Appendix A. Measuring Microsphere Center Distances From Photomicrographs

The relative positions of the photographed microsphere focal spot positions are read out with a coordinate measuring machine (CMM). Its probe is a microscope containing a high-resolution image sensor (vidicon) and circuitry to pinpoint the center of each focal spot, which produces steering signals to the X-Y CMM drives to bring the focal spot center to the boresight axis (center of the microscope's field of view). The CMM's X-Y coordinates are then stored.

Next, for each photograph being measured a decision is made as to what measurement path will be selected from one focal spot to the next, in order to make sure that each sphere is measured only once and that each sphere in the grouping was free to assume its contacting position with its neighbors during drying (no mechanically overdetermined sphere arrangement). The path selection is done by an operator using an interactive graphics routine. The CRT display shows all focal spots in their relative positions with circles drawn around each one, to simulate the actual microsphere scene rather than the focal spot representation of it. It also shows the keyed-in measurement path (see Fig. 3). The result is a string of X-Y coordinates in which each increment represents a center distance (CD) between two adjacent (contacting) spheres.

Before the CDs are computed each focal spot position is first corrected for image distortion of the microscope (this distortion can be determined as in Appendix B). Because the distortion is a radial function these position corrections take the form of small radial shifts. Their magnitudes depend on the initial off-axis distances, and are found by means of a stored function or lookup table.

An impression of the repeatability and accuracy of the film measuring system can be obtained from the following information:

1. The CMM is normally used for the calibration of precision grid plates. It has been extensively studied, and its positional accuracy is better than 0.1 μm over the area of interest [8].
2. Each focal spot was centered to the same point of the camera field, and all the spots were about the same size. Therefore any geometrical errors in the camera scan can have only secondary effects on the measurement.
3. A photograph selected at random was run a number of times without being moved. The center distances (3 mm nominally, the print magnification being 1000×) showed a repeatability with standard deviation less than 0.5 μm.
4. One other photograph was measured repeatedly while the microscope focus was varied in both directions. Since the focal spot brightness was not completely isotropic, the focus settings changed the apparent size and shape of the focal spots by small amounts. The resultant changes in focal spot positions were very small and uncorrelated, with an estimated standard deviation of less than 0.5 μm.
5. A few photographs were reexamined after all had been measured in order to check for any process changes during the measurements. No changes larger than the measured repeatability were found.

The CMM used was a five-axis Moore V from Moore Special Tools Company. The TV camera system consisted of a Dage-MTI Inc. high-resolution vidicon camera Model 65, with a Bausch & Lomb lens type Mono Zoom 7 and a vision system from Videometrix VPU, Model 101110-501-14. The scene illumination was a diffuse one, using a fiber-optic ring illuminator from Titan Tool Company.

9. Appendix B. Measuring the Print Magnification (Film Scale) and Image Distortion

To set the scale of the photographs a section of a calibrated object micrometer is photographed and measured. To maximize resolution the photographed length is made to span the whole field of view. The measured length is then corrected for

the effects of image distortion which causes off-axis image points to be radially shifted from their intended positions. The corrected length now shows the image magnification in the absence of image distortion. In other words: one has found the on-axis image magnification value.

For the determination of image distortion the microscope magnification itself is not needed. In the following is shown how these properties were measured.

a) Image distortion.

Following a scheme outlined in Ref. [1] this goes as follows. A row of microspheres is placed such that it crosses the center of the field of view. Its row of focal spots is photographed. Then the row is shifted in-line by four sphere diameter ($4D$) and its focal spots are recorded again. All distances between adjacent sphere centers are measured in both photographs; it will be seen that some center distances will have decreased while others increased. These changes are so small that an in-line shift of $4D$ rather than D was chosen in order to make the center distance changes stand out from measurement noise (see Fig. 8a).

Assuming a $4D$ shift from left to right, and starting with the far left (first) sphere pair, one finds the accumulated length changes when the center distance length D is shifted in-line by $4D$ at the various points in the field of view. A second data set is found by repeating the length change calculations starting at the next left sphere pair. A third data set is obtained from the third left sphere pair, and likewise for the fourth set. The four data sets belong to a common curve, and a best fit of all four sets is obtained as shown in Fig. 8b.

Figure 8b therefore shows by what percentage a center distance D will vary as it is shifted all across the field of view (this is equal to the percent change in magnification for radial objects as a function of off-axis distance). A graphic integration then yields the radial shifts of off-axis image points as a function of their off-axis distance, that is, the image distortion as shown in Fig. 8c.

b) Film scale.

With the image distortion known, the film scale or on-axis magnification M_0 is found next as shown in Fig. 8b. If M_0 is measured a number of times the results will show data scatter, typically 0.3% at 3 σ. This is caused by small changes in axial position when fresh sheet film is inserted in the cassette. The corresponding scale changes can be reduced by averaging over a number of repeat exposures, for instance five, of the object micrometer.

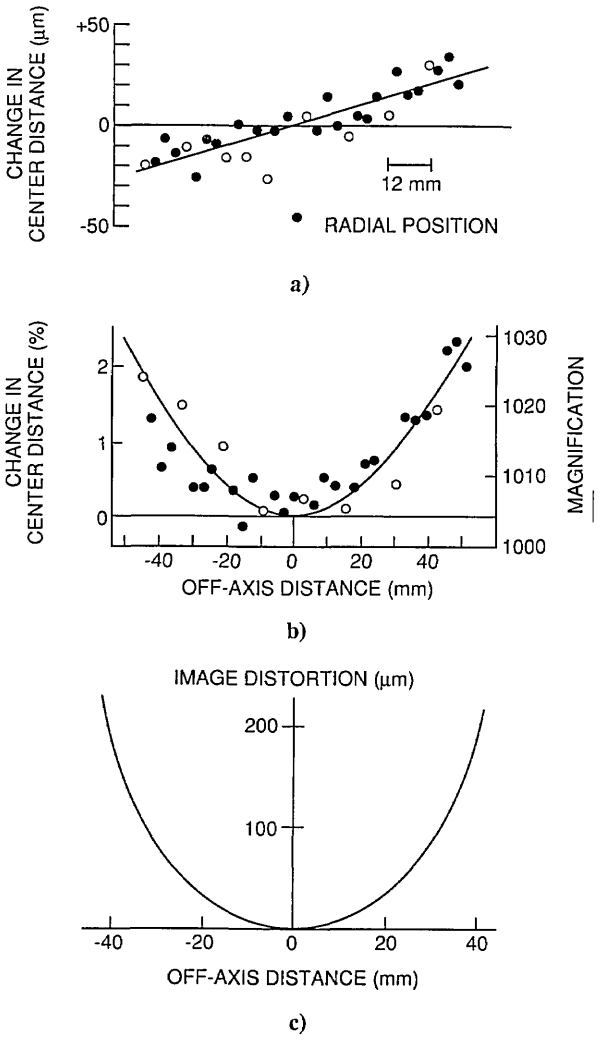

Fig. 8. Finding microscope image distortion and magnification.

The effect of inserting fresh sheet film in the cassette can be measured by placing a row of microspheres such that it crosses the center of the microscope's field of view, taking five repeat photomicrographs, and measuring a number of sphere center distances in all photographs. The scatter found in these lengths contains the combined effects of film readout, local emulsion shifts and changes in film scale. As shown in Fig. 9 these data approximate a straight line through the origin; the slope of that line represents the scatter in film scale or magnification (0.09% at 1 σ in our case), for areas near the center of the photographs. For this experiment a 10 μm microsphere array was centered in the field of view, and the various lengths in Fig. 9 were realized by summing the lengths of a number of adjacent microsphere rows. The found magnification scatter was indicative of film flexure at the central area of the film frame.

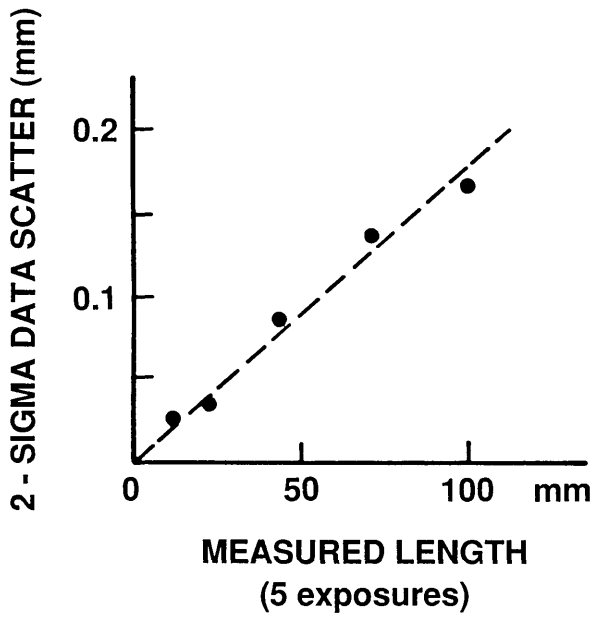

Fig. 9. Scatter in image magnification.

10. References

[1] A. W. Hartman, Powder Technol. **46**, 109 (1986).
[2] G. G. Hembree, Proc. 44th Ann. Meeting, G. W. Bailey, ed., San Francisco Press, San Francisco (1986) p. 644.
[3] D. A. Swyt and S. W. Jensen, Prec. Eng. **3**, 11 (1981).
[4] H. E. Kubitschek, Nature **192**, 48 (1961).
[5] A. W. Hartman, Powder Technology **42**, 269 (1985).
[6] B. V. Derjaguin, V. M. Muller, and Yu P. Toporov, J. Coll. Interf. Sci. **53**, 414 (1975).
[7] K. L. Johnson, K. Kendall, and A. S. Roberts, Proc. Roy. Soc. Lond. **A324**, 301 (1971).
[8] R. J. Hocken et. al., Ann. C.I.R.P., Vol. 26 (1977).

About the authors: A. Hartman, T. Doiron, and J. Fu are physicists in the Precision Engineering Division at NIST. The National Institute of Standards and Technology is an agency of the Technology Administration, U.S. Department of Commerce.

Volume 97, Number 2, March-April 1992
Journal of Research of the National Institute of Standards and Technology

[J. Res. Natl. Inst. Stand. Technol. 97, 267 (1992)]

Optical Calibration of a Submicrometer Magnification Standard

Volume 97 | Number 2 | March-April 1992

Jon Geist, Barbara Belzer, Mary Lou Miller, and Peter Roitman

National Institute of Standards and Technology,
Gaithersburg, MD 20899

The calibration of a new submicrometer magnification standard for electron microscopes is described. The new standard is based on the width of a thin thermal-oxide film sandwiched between a silicon single-crystal substrate and a polysilicon capping layer. The calibration is based on an ellipsometric measurement of the oxide thickness before the polysilicon layer is deposited on the oxide. The uncertainty in the derivation of a thickness for the layer from the ellipsometric parameters is also derived.

Key words: calibration; electron microscope; magnification standard; scanning electron microscope; transmission electron microscope.

Accepted: January 13, 1992

1. Introduction

It was recently proposed [1] that the same calibration technique [2] used to produce the NIST 2530 Standard Reference Material (SRM) series of oxide thickness standards could be used as the basis for a new submicrometer magnification standard. The key ideas for the new standard are the following: 1) A thin thermal oxide is grown on a 76.2 mm (3 in diameter) silicon wafer, 2) the thickness of the oxide is measured at the center of the wafer with the NIST High-Accuracy Ellipsometer [3], 3) the variation in oxide thickness is measured at nine points over the wafer using a high-precision reflectometer, and 4) a polysilicon cap is deposited over the oxide layer subsequent to certification of the oxide thickness. Sections of the resulting wafer can be used as submicrometer magnification standards when viewed edge on. For use in a Scanning Electron Microscope (SEM), the cleaved edge must be dipped in a weak solution of HF for a few seconds before viewing in order to create topographic features. For use in a Transmission Electron Microscope (TEM), the standard can be sectioned in the usual way.

This paper describes the calibration of this new standard and the associated uncertainty analysis. There are two very different types of uncertainty associated with this standard. The first is the uncertainty in the thickness of the oxide at any point on the wafer. This uncertainty, which is reported in the calibration certificate, is described here. The second is the uncertainty associated with the resolution of the oxide-silicon interfaces in an electron microscope. This uncertainty will vary depending upon the machine and the operating conditions, and must be estimated by the user. With some SEMs, this uncertainty will be much larger than the calibration uncertainty, and with some TEMs, it may be smaller than the calibration uncertainty. In either case, these two uncertainties are added in quadrature because they are uncorrelated. This paper is concerned only with the calibration of the oxide thickness, and does not address the uncertainty associated with the actual use of the standard in an electron microscope.

A model of the optical properties of the magnification standard is needed to extract the thickness

of the oxide layer from the measured ellipsometric parameters. The model used for the silicon/silicon dioxide system consists of three layers as shown in Fig. 1: 1) a homogeneous, isotropic top layer characterized by a film thickness t_f and a real index of refraction n_f; 2) a homogeneous, isotropic interlayer characterized by an interlayer thickness t_i and a real index of refraction n_i; and 3) a homogeneous, isotropic substrate characterized by a complex index of refraction n_s. The three-layer model is used because Taft and Cordes showed that a two-layer model produces an oxide index of refraction that depends upon oxide thickness, which is clearly unphysical [4]. The bottom layer is interpreted as single-crystal silicon and the top layer as amorphous silicon-dioxide. The interpretation of the interlayer in terms of a physical structure is less straightforward, and is discussed in detail later in this paper.

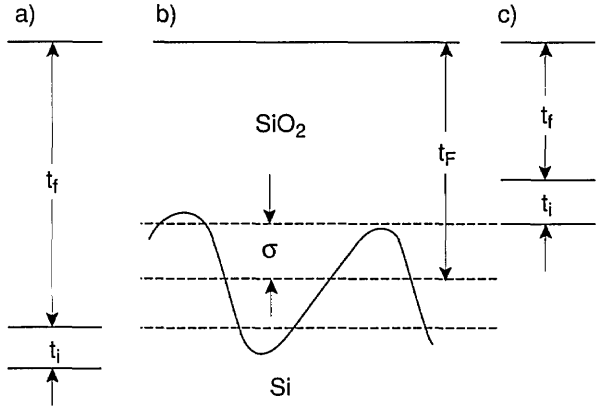

Fig. 1. Optical model of a thermal oxide on a single-crystal silicon substrate that was used to derive an oxide thickness from measurements of ellipsometric Δ and ψ data for the principal angle at 633 nm.

It is not possible to determine t_f, t_i, n_f, n_i, and n_s from measurements of the ellipsometric parameters [2] Δ and ψ on a single wafer. The derivation of the values reported in the certificate of calibration for this new standard is carried out on a lot of wafers as described in Ref. [2]. The remainder of this paper describes in more detail how a lot of wafers is measured, how the oxide thickness is calculated, and how the uncertainty in the oxide thickness is estimated. The details provided here complement those presented in Ref. [2], with the exception that t_f+t_i is used as the oxide thickness in Ref. [2], whereas $t_f+t_i/2$ is used for the oxide thickness for this magnification standard. The main reason for this change is that the ellipsometric standard is concerned with the thicknesses of layers defined by an optical model, whereas this standard is concerned with the thickness of a physical layer, and $t_i/2$ is more consistent with alternative physical models of the optically determined interlayer. This point is explained in more detail later in this paper.

2. Definition of a Batch and a Lot of Wafers

For the purposes of this magnification standard, a batch of wafers is defined as a set of at least five wafers that were put into an oxide-growth furnace at the same time, so all of the wafers in the batch have the same growth conditions and same nominal oxide thickness. A batch of wafers is processed and measured in the following steps:

1) The wafers are cleaned and dried immediately before loading into an oxide-growth furnace.
2) A nominal thickness oxide is grown on the wafers.
3) The relative variation of the oxide thickness is measured at nine points on the surface of each wafer as shown in Fig. 2.
4) A simple model of the variation in oxide thickness with position on the wafer is fit to the data measured in Step 3 above, as discussed later in this paper.
5) The ellipsometric parameters Δ and ψ at the center of each wafer for the principal angle of incidence are measured at 633 nm with the NIST High-Accuracy Ellipsometer [3].
6) A layer of polysilicon is deposited over the oxide.

A lot of wafers is defined to be a set of at least three batches of wafers. To qualify as a lot, 1) at least one batch must consist of wafers with nominal 50 nm oxides, another with nominal 100 nm oxides, and a third with nominal 200 nm oxides, and 2) all oxides must have been grown at the same temperature with the same gas-flow conditions in the same furnace. Batches of wafers with nominal 12 and 25 nm oxides may also be included in a lot on a fairly routine basis, and batches of other thicknesses may be included on occasion. The thicknesses of 50, 100, and 200 nm were chosen for consistency with Ref. [2]; the restrictions on lots and batches of wafers are required because n_f and either n_i or t_i have been determined to depend upon growth conditions [4].

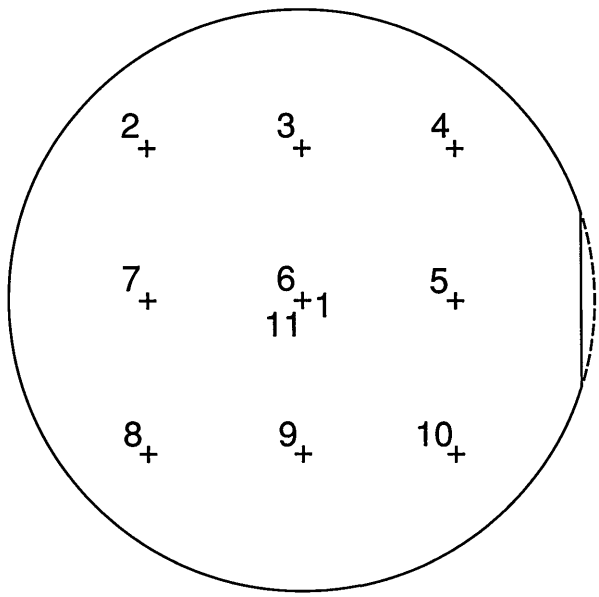

Fig. 2. Order in which the thickness of the oxide is measured relative to the center of the wafer at the points denoted by crosses. The crosses are on 2 cm centers. The center is measured as points 1, 6, and 11.

When all of the wafers in all of the batches constituting a lot have been measured, the thicknesses t_f of the oxide films on the individual wafers in the lot are adjusted in a least-squares fit [2,5] to the experimental Δ and ψ data based on the model shown in Fig. 1. The extinction coefficient k_s of the silicon substrate at 633 nm is assumed to be the same for all of the wafers in the lot, and is fixed at 0.0156 ± 0.0003 [6]. The indices of refraction n_s, n_f, and n_i of the silicon substrate, the silicon-dioxide film, and the interlayer, respectively, are assumed to be the same for all wafers in the lot, and are adjusted to produce the best fit. The thickness t_i of the interlayers is also assumed to be the same for all wafers, and is also adjusted in the fit [4].

3. Oxide Thickness and Uncertainty

The thickness of the oxide at any point (x,y) on the wafer for which -2 cm $\leq x \leq 2$ cm, and -2 cm $\leq y \leq 2$ cm can be calculated from the values of t_f, t_i, α, and β reported on the certificate of calibration for the new magnification standard by using

$$t(x,y) = t_f + t_i/2 + \alpha x + \beta y. \quad (1)$$

The point (0,0) is the center of the circular extension of the circumference of the wafer as shown in Fig. 2. Equation (1) assigns $t_f + t_i/2$ as the oxide thickness at the center of the wafer. The reason for this choice is associated with the interpretation of the interlayer, and is described in the sections of this paper devoted to that topic.

The estimated standard deviation of $t(x,y)$ is given by

$$\Delta t = (\Delta t_f^2 + \Delta t_i^2 + t_i^2 + t_i^2 + \Delta t_{map}^2 + \Delta t_{poly}^2)^{1/2}. \quad (2)$$

The quantity Δt is the uncertainty in the oxide thickness, and it is reported in the calibration certificate. The uncertainties in α and β are so small that they do not contribute significantly to the overall uncertainty, and they are not reported. The nature of the uncertainties contributing to Δt and how they were calculated is described below.

The quantities Δt_f and Δt_i in Eq. (2) are the uncertainties associated with the adjustment of t_f and t_i in the fit referred to in the previous section. In principle, Δt_f and Δt_i vary from wafer to wafer, but in fact they are dominated by systematic errors that are common to all of the ellipsometric measurements, so Δt_f and Δt_i are the same for all wafers, even from different lots and batches. The first t_i in Eq. (2) is an uncertainty associated with the use of the model of Fig. 1. The second t_i is an uncertainty that accounts for any microscopic roughness of the oxide-silicon interface and any microscopic variations in the oxide thickness. Microscopes are sensitive to these variations, but the High-Accuracy Ellipsometer is not, due to its macroscopic beam size, which is measured in millimeters. The uncertainty Δt_{map} is the residual standard deviation of the fit of the model of Eq. (1) to the measured data on the variation of oxide thickness over the surface of the wafer, and Δt_{poly} is an uncertainty associated with assigning a thickness to the oxide under the polysilicon on the basis of measurements carried out before the polysilicon was deposited.

4. Film and Interlayer Thickness

The uncertainties Δt_f and Δt_i are determined as described in Ref. [2]. They are one-sigma estimates for the sum in quadrature of the uncertainties associated with both the random errors and the systematic errors in the measured values of Δ and ψ for the individual wafers in the lot under the assumption that the model in Fig. 1 accurately describes the wafers. The problem with this assumption is that different interpretations of the interlayer require that it be apportioned differently between the top oxide layer and the silicon substrate.

5. Interpretation of Interlayer

The physical interpretation of the interlayer shown in Fig. 1 is not straightforward because different experimental results reported in the literature do not appear to be consistent. The interlayer has been interpreted as a graded layer of SiO_x where the x value varies from 0 on the silicon side of the interlayer to two on the oxide side of the interlayer [4]. This interpretation is consistent with the fact that the optically derived thickness for the interlayer varies from 0.5 to 2.0 nm, depending upon the particular samples constituting a lot of wafers. This interpretation is also supported by x-ray photoemission spectroscopy (XPS) measurements that detect silicon in every allowed oxidation state at the interface [7]. According to this interpretation, most of the interlayer (if not all of it) should be considered part of the oxide.

On the other hand, TEM [8] and grazing incidence x-ray scattering measurements [9] on thermal oxides grown between room temperature and 900 °C on (100) silicon surfaces detect only a single atomic layer of silicon that is not bonded either like single-crystal silicon or like silicon dioxide. This result is not necessarily inconsistent with the XPS results. Some of the dangling bonds associated with the specially bonded layer of silicon atoms could be dimerized or tied up by bridging oxygen atoms to create the various XPS peaks associated with the remaining oxidation states. (It does not seem possible to determine the concentrations of different species from the heights of the XPS peaks.)

Even though the TEM and grazing-incidence x-ray scattering results are not necessarily inconsistent with the XPS results, the former strongly suggest that the interlayer should be 0.5 nm thick, and should not vary from lot to lot. These results also predict that the interlayer should be considered part of the silicon in some experiments such as TEM measurements, but part of the oxide in other experiments such as those in which etches remove the atypically bonded atomic layer of silicon atoms as well as the oxide.

A possible resolution of this paradox is that some portion of the optically derived width of the interlayer is an artifact that produces a better fit to the experimental data because it involves an extra free parameter, but does not correspond exactly to any real structure at the interface. For example, the interlayer in the optical model might be compensating for the polarization properties introduced by the roughness of the silicon surface and the microscopic variations in thickness of the oxide layer [10]. This situation is illustrated in Fig. 3.

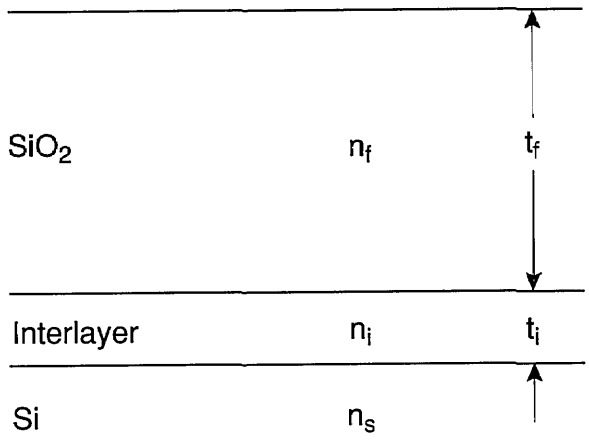

Fig. 3. Schematic illustration of plausible worst-case limits a) and c) between the film and interlayer thicknesses t_f and t_i in the optical model and the average oxide thickness t_F if the interlayer is an artifact that describes the change in polarization induced by the roughness at the oxide-silicon interface as shown in b). If this is the case, t_f and t_i are adjusted to produce the same polarization of the radiation leaving the oxide surface as is produced by the roughness and t_F, and t_F need not equal t_f.

6. Microscale Roughness

Figure 3b represents a rough interface between the oxide and the silicon substrate for spatial frequencies great enough so that the top surface of the oxide is not conformal with the interface under the assumption that such spatial frequencies exist. The average oxide thickness is denoted by t_F and the root-mean-square (rms) roughness is denoted by σ, and it is assumed that the ellipsometric parameters $\Delta(\sigma)$ and $\psi(\sigma)$ depend upon σ. Therefore, t_f and t_i, which are obtained by fitting the optical model to the measured Δ and ψ data for a wafer, also vary with σ. In fact, there is no reason that t_f should be identical to t_F even though this result would be intuitively satisfying.

The only way to definitively determine the dependence of t_f and t_i on σ is to solve Maxwell's equations for oblique incidence on a rough surface. This is not within the scope of this paper. However, there is some evidence that $t_i \simeq \sigma$ for $\sigma < 5$ nm [11], and Figs. 3a and 3c shows worst-case estimates for the limits of variation of t_f with σ. For one limit, the average film thickness is given by

$$t_F = t_f + t_i + \sigma, \tag{3}$$

and for the other limit it is given by

$$t_F = t_f - \sigma. \tag{4}$$

This range is covered by

$$t_F = t_f + t_i/2 \pm (t_i/2 + \sigma). \quad (5)$$

This is the justification for the first two terms in Eq. (1).

The range $\pm(t_i/2+\sigma)$ represents a limit of error. What is needed for Eq. (2) is something more like a one-standard deviation estimate. This can be obtained by multiplying the range by 2/3. If we now use t_i as an approximation to σ as suggested in Ref. [11], the uncertainty becomes $\pm t_i$. This is the first t_i appearing in Eq. (2).

The uncertainty just described accounts only for the model uncertainty. An additional $\pm\sigma$ must be added to allow for the possibility that the microscope might sample the oxide thickness at a crest, a trough, or or any other part of the micro-rough oxide-silicon interface illustrated in Fig. 3. Once again, we approximate σ by t_i, and obtain the second t_i appearing in Eq. (2). Interpretation of the entire interlayer as an artifact of roughness as shown in Fig. 3 is a worst-case scenario. The other interpretations of the interlayer that were discussed above are all described by Eq. (5), and the stated uncertainties should be sufficiently conservative.

7. Variations in Oxide Thickness

Before the polysilicon is deposited on the wafer, the thickness t_n of the oxide on each wafer is measured with a reflectometer for the points $n = 1, 2, 3, \ldots, 11$ indicated in Fig. 2. The parameters α, β, and t in the equation

$$t_n = t + \alpha x_n + \beta y_n \quad (6)$$

are adjusted in a least-squares fit to the measured data points, where x_n and y_n are given in Table 1. The parameters α and β describe the variation of oxide thickness about the thickness at the center of the wafer, and are reported in the calibration certificate. The residual standard deviation of the fit is used as Δt_{map} in the calculation of the uncertainty in Eq. (2), and if any single residual is larger than 0.6 nm, the wafer is rejected for use as a standard. The value t is not reported, since $t_f + t_i/2$, which is derived from the measurements made with the High-Accuracy Ellipsometer, is a more accurate estimate of the thickness of the oxide at the center of the wafer.

The symmetric location of the points in Fig. 2 about the wafer center greatly simplifies the least-squares analysis [12], so

$$\alpha = \frac{(\Sigma x_n t_n)}{24\ \text{mm}^2}, \quad (7)$$

$$\beta = \frac{(\Sigma y_n t_n)}{24\ \text{mm}^2}, \quad (8)$$

and

$$\Delta = \Delta t_{map} / 9.4\ \text{mm},$$

where Δ is the uncertainty in the coefficients α and β.

Table 1. Relation of position coordinates x and y to measurement number in uniformity map of oxide thickness

Measurement No.	x (cm)	y (cm)
1	0.0	0.0
2	−2.0	2.0
3	0.0	2.0
4	2.0	2.0
5	2.0	0.0
6	0.0	0.0
7	−2.0	0.0
8	−2.0	−2.0
9	0.0	−2.0
10	2.0	−2.0
11	0.0	0.0

8. Thickness of the Oxide Under the Polysilicon

The following experiment was conducted to set an upper limit on the change in thickness of the oxide caused by deposition of the polysilicon layer. Seven wafers with oxides with nominal 100 nm oxides were selected, and the oxide thicknesses were measured at the center of each wafer with the High-Accuracy Ellipsometer. A layer of polysilicon similar to that used on the new submicrometer magnification standard was deposited over the oxide on each wafer, and was removed after the wafer cooled to room temperature by etching in 14 *M* KOH for 30 min at room temperature [13]. The wafers were then rinsed for 15 min in deionized H_2O at room temperature. The thicknesses of the oxides were then remeasured. The average value of the difference between the oxide thickness before and after the deposition and etch was 0.6 nm with a standard deviation of the mean of seven measurements of 0.1 nm. The difference is used for Δt_{poly} in Eq. (2). This is a conservative estimate because the decrease in thickness of the oxide layer is more likely associated with the removal of the polysilicon than with its deposition.

9. Conclusion

Typical values of Δt and of the terms in Eq. (2) that contribute to it are listed in Table 2. It is clear that the uncertainties of magnitude t_i completely dominate the other uncertainties listed in Table 2 in their contribution to Δt through addition in quadrature. As far as this standard is concerned, there is no reason to attempt to decrease any of the other uncertainties listed in Eq. (2) until the physical meaning of the interlayer derived from the optical model is clearly understood, so that these uncertainties can be replaced by smaller values. Nevertheless, the uncertainty Δt in the calibration of the oxide thickness is quite satisfactory for many applications, and will, in fact, be much smaller than the errors associated with the use of the standard in many electron microscopes.

Table 2. Typical values for the uncertainties in the oxide thickness

Error term	Value (nm)	Source of error
Δt_f	0.5	t_f from fit
Δt_i	0.4	t_i from fit
t_i	1.4	meaning of interlayer
t_i	1.4	possible roughness of interface
Δt_{map}	0.3	variation in oxide thickness
Δt_{poly}	0.6	deposition of polysilicon
Δt	2.2	sum in quadrature

10. References

[1] P. Roitman, unpublished.
[2] G. A. Candela, D. Chandler-Horowitz, J. F. Marchiando, D. B. Novotny, B. J. Belzer, and M. C. Croarkin, Natl. Inst. Stand. Technol., SP 260-109 (1988).
[3] G. A. Candela and D. Chandler-Horowitz, SPIE **480**, 2 (1984).
[4] E. Taft and L. Cordes, J. Electrochem. Soc. **126**, 131 (1979).
[5] J. F. Marchiando, Natl. Inst. Stand. Technol., SP 400-83 (1989).
[6] J.Geist, A. R. Schaefer, J-F. Song, Y. H. Wang, and E. F. Zalewski, J. Res. Natl. Inst. Stand. Technol. **95**, 549 (1990).
[7] M. Niwano, H. Katakura, Y. Takeda, Y. Takakuwa, and N. Miyamoto, J. Vac. Sci. Technol. **A9**, 195 (1991).
[8] A. Ourmazd, D. W. Taylor, J. A. Rentschler, and J. Bevk, Phys. Rev. Lett. **59**, 213 (1987).
[9] G. Renaud, P. H. Fuoss, A. Ourmazd, J. Bevk, B. S. Freer, and P. O. Hahn, Appl. Phys. Lett. **58**, 1044 (1991).
[10] T. Yamaguchi, J. Lafait, A. Bichri, and K. Driss-Kodja, Appl. Opt. **30**, 489 (1991).
[11] J. R. Blanco and P. J. McMarr, Appl. Opt. **30**, 3210 (1991).
[12] N. R. Draper and H. Smith, Applied Regression Analysis, Wiley, New York (1966) p. 58.
[13] D. L. Kendall, Ann. Rev. Mater. Sci. **9**, 373 (1979).

About the authors: *Jon Geist and Peter Roitman are physicists, Barbara Belzer is a physical science technician, and Mary Lou Miller is an electronics technician in the Semiconductor Electronics Division of the NIST Electronics and Electrical Engineering Laboratory. The National Institute of Standards and Technology is an agency of the Technology Administration, U.S. Department of Commerce.*

Volume 97, Number 2, March-April 1992
Journal of Research of the National Institute of Standards and Technology

[J. Res. Natl. Inst. Stand. Technol. 97, 273 (1992)]

Probe-Position Error Correction in Planar Near Field Measurements at 60 GHz: Experimental Verification

Volume 97 | Number 2 | March-April 1992

Lorant A. Muth

National Institute of Standards and Technology,
Boulder, CO 80303

This study was conducted to verify that the probe-position error correction can be successfully applied to *real* data obtained on a planar near-field range where probe position errors are known. Since probe position-error correction is most important at high frequencies, measurements were made at 60 GHz. Six planar scans at z positions separated by 0.03 λ were obtained. The correction technique was applied to an error-contaminated near field constructed out of the six scans according to a discretized periodic error function. The results indicate that probe position errors can be removed from *real* near-field data as successfully as from *simulated* data; some residual errors, which are thought to be due to multiple reflections, residual drift in the measurement system, and residual probe position errors in all three coordinates, are observed.

Key words: error correction; experimental verification; planar near fields; probe-position errors.

Accepted: December 24, 1991

1. Introduction

In this study I establish the correctness and effectiveness of the probe-position error correction using *real* rather than *simulated* data. All of the required theory has been thoroughly discussed in [1] and [2] for the *planar* and *spherical* error correction, respectively. In these publications we demonstrated that computer simulations using *exact* near fields and computer-generated error-contaminated near fields successfully produced error-corrected near fields that agree with the original error-free near fields within fractions of a decibel in amplitude and to within a fraction of a degree in phase. The method has been shown to work for errors as large as 0.2 λ at 3.3 GHz. Similar results were obtained with theoretical computer simulations at 60 GHz in the context of this study. Such results indicate that the theoretical formalisms appearing in [1] and [2] are correct, independent of the frequency or the near-field pattern.

However, an important aspect of the correction problem has not yet been addressed. We must examine the error correction procedure in the presence of

(a) *multiple reflections* in measured near fields
(b) *residual drift* in measured near fields, and
(c) *residual errors* in the probe's position,

which are experimental factors not taken into account in the theory nor in the numerical simulations. In addition, any probe position error function used with real data is necessarily discretized rather than continuous, and the extent to which this effects the success of the correction procedure is not immediately apparent. Therefore, the technique must be robust and stable enough that the introduction of these additional uncertainties (experimental effects) into the procedure does not destroy its usefulness. For example, the uncertainties due to multiple reflections are of the order of or larger than the

uncertainties due to probe position errors [3]. We can consider these two effects to be independent and, therefore, expect that the error correction technique will not fail with real data.

This work completes a long series of studies. It establishes the theoretical correctness of the error-correction formalism, even when used with data contaminated by experimental effects, and demonstrates the *practical* usefulness of the error-correction procedure.

We first present a brief overview of the theoretical concepts needed to understand probe-position error correction. Next, we describe the experimental design and measurements we obtained to correctly implement the error correction, and, finally, we observe what effects the experimental contaminations, as described in (a), (b) and (c) above, have on the results.

2. Theoretical Review

In planar near-field measurements, data are, in reality, taken on an *irregular* plane on an *irregular* grid. We denote an irregular grid on which measurements are taken by $x+\delta x$, where $x=x(x,y,z)$ is an exact set of grid points separated by constant increments in x and y, $z=z_0$ is a constant, and $\delta x(x,y,z)$ is the deviation of the position of the probe from the exact grid position at (x,y,z_0). We assume that the probe-position error function $\delta x(x,y,z)$ is known at every point of measurement. If the near field that exists at the exact grid positions is denoted by $b(x)$ and the *measured* near field is denoted by $b(x+\delta x)$, then we can write

$$b(x+\delta x)=(1+T)b(x), \tag{1}$$

where $(1+T)$ is the infinite Taylor series operator taking a continuous function from a point to a neighboring point. An *error-contaminated* near-field function can now be defined as

$$\hat{b}(x;\delta x)\equiv b(x+\delta x), \tag{2}$$

which means that the error-contaminated near field exists on a *regular* grid x, and computations using fast Fourier transforms can be performed on it. Equations (1) and (2) yield

$$\hat{b}(x;\delta x)=(1+T)b(x). \tag{3}$$

The error-correction technique can be stated mathematically as

$$b(x)=(1+T)^{-1}\hat{b}(x;\delta x), \tag{4}$$

which implies that the *error-free* near field on a *regular* grid can be obtained from the error-contaminated (measured) near field by obtaining the inverse of the operator $1+T$, and applying this inverse to the measurements. This leads to the well-ordered small parameter expansion (to fourth order),

$$b(x)=(1-t_1-t_2-t_3-t_4+t_1t_1+t_1t_2+t_1t_3+t_2t_1+t_2t_2$$
$$+t_3t_1-t_1t_1t_1-t_1t_2t_1-t_1t_1t_2-t_2t_1t_1+t_1t_1t_1t_1)\hat{b}(x;\delta x), \tag{5}$$

where $t_n=1/n!(\delta x_k)^n(\partial/\partial x_k)^n$, the nth-order term of the Taylor series for the coordinate x_k. For further details and in-depth discussions see [1,2], wherein the method of computing the required derivatives and the structure of the individual terms in Eq. (5) are discussed further. Also, for a thorough documentation of the the software package developed to implement the error-correction technique see [4].

3. Experimental Design and Measurements

To enhance the high-frequency calibration capability at NIST, we decided to test the probe correction procedure at 60 GHz using a center-fed Cassegrain parabolic reflector antenna of 0.5 m in diameter. Since the wavelength $\lambda\approx 5$ mm at this frequency, a probe-position error as small as 1 mm $\approx 0.2\,\lambda$ can lead to significant errors in the measured near fields, and, consequently, in the far fields obtained from such error-contaminated near fields. For example, the phase error would be an unacceptable 72° for a plane wave.

A schematic of the sequence of measurements and the experimental design parameters is shown in Fig. 1. Given planar near-field scans labelled with indexes $0\ldots N$, and separated by small distances δz, we can construct any number of error-contaminated near fields by selecting a near-field value at each (x,y) point in the scan area according to the scan plane index. The index can be specified using any criteria that uniquely assigns the integers 0 to N at each point in the scan plane. When the corresponding near-field values are thought of as part of a single scan, an error-contaminated near field is obtained. This field can be arbitrarily assigned to exist at z_0, without loss of generality.

For the error-correction study we have used the index function

$$j=\mathrm{int}[N\cos^2(3\alpha x)\cos^2(3\alpha y)+0.5],$$

where $\alpha=2\pi/L$, L is the length of the scan plane in centimeters, and int is the fortran truncate-to-

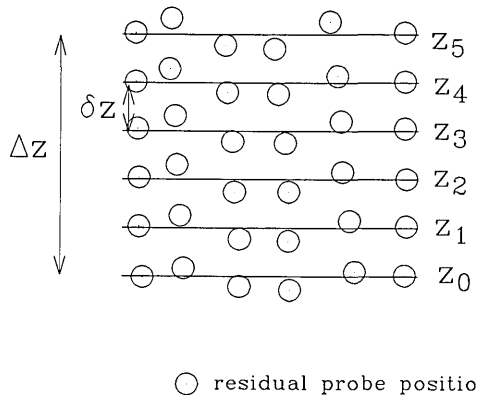

Fig. 1. The experimental design used to verify the probe position error-correction technique at 60 GHz. The six scan planes z_0 to z_5 were separated by $\delta z = 0.03\lambda$, so that the maximum possible probe position error is $\Delta z = 0.15\lambda$. The residual errors are shown schematically.

integer function. The discretized probe position-error function is then $[z] = j\delta z$, and the maximum probe position error $\Delta z = N\delta z$. Previous simulations using the continuous probe position-error function $z = \Delta z \cos^2(3\alpha x)\cos^2(3\alpha y)$ have demonstrated the success of the error-correction technique at 3.3 GHz [1] for $\Delta z = 0.2\lambda$. The choice of periodic error functions was motivated by the fact that periodic position errors induce high sidelobe errors in the far field.

The magnitudes of the experimental parameters δz and $\Delta z = N\delta z$, where $N+1$ is the number of scan planes, were chosen to ensure that system imperfections do not overwhelm the experimental results sought. Residual system drift during a tie-scan [5] and repeatability of the laser positioning system used to locate the scan planes are the relevant experimental factors here. If $\delta\phi$ denotes the system phase drift during δt, the time needed to complete a tie scan, and $\Delta\phi$ is a typical phase difference between the near fields at successive scan planes, then we must have $\Delta\phi \gg \delta\phi$ to be able to isolate position error effects. Similarly, phase errors due to repeatability must be much less than $\Delta\phi$.

3.1 System Drift

Figure 2 shows the phase as a function of time at the normalization point in a scan plane over a period of a few hours. The crucial experimental parameter here is the maximum expected phase shift $\delta\phi$ during $\delta t \approx 2$ min, which was the time required to obtain a single tie-scan. Less stringently, an average or most probable phase shift can be used. From Fig. 2 we estimate that $\delta\phi \approx 4°$. Hence, $\delta z = 0.03\lambda$, which represents a phase error of $\Delta\phi = 10.8°$ in a plane wave, was chosen as the distance between the individual scans (see Fig. 1). This distance is also greater than the residual position errors of ≈0.04 mm known to exist on the accurately aligned planar near-field range at NIST [6].

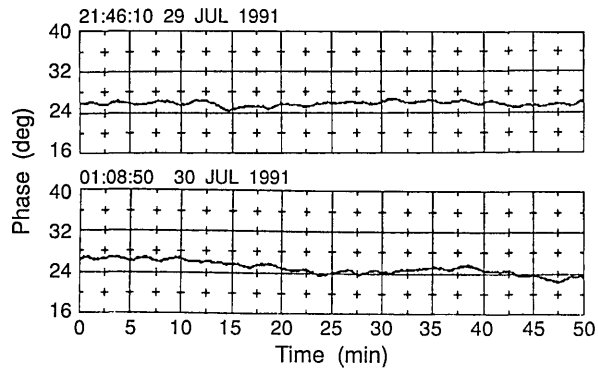

Fig. 2. The phase drift in degrees as a function of time as observed at the normalization point. Each horizontal box represents 20 min. The residual drift is estimated to be ≈4°.

3.2 Repeatability of the Laser Positioning System

The scan planes were located using a laser positioning system that could measure translations in the z direction accurately at the normalization point of the scan. The initial point was located in the z_0 scan plane, and the distance between the probe and the antenna was increased manually by δz (read on a digital display) seven times. This whole cycle was repeated eight times. As shown in Fig. 3 the relative normalization values in each scan plane were recorded at the time the scan plane was located. We observe that as the probe is moved from the z_0 scan plane, the variability in the amplitude of the signal increases, until at z_5 the variability begins to be large enough to compete with the variations as we step from scan plane to scan plane. Hence, the scan plane at z_5 was chosen to delineate the maximum acceptable probe position error Δz under the prevailing experimental conditions, giving $\Delta z = 5\delta z = 0.15\lambda$. An examination of the repeatability of the phase reveals no additional problems with this choice. The variability observed here can be attributed to system drift and to human error in positioning the probe. These two effects cannot be separated without further study, and no attempt was made to do this. Figure 3 also shows *theoretical* normalization values in each scan plane. This is further discussed in Sec. 6 when multiple reflections are considered.

Figure 4 shows the amplitude of the near field measured at z_0. The scan area was 1×1 m^2, and data were taken at 2 mm intervals in both the x and y directions. The resulting 501×501 data matrix was zero-filled to get a 512×512 dataset, which was then used in all subsequent analysis. The near-field amplitudes obtained in the scan planes z_1 to z_5 are almost indistinguishable from the one shown; hence they are not included here.

Figure 5 shows composite plots of the far fields obtained from the six near fields. By definition, error-free near-field measurements should yield the same far field; hence, the *vertical spread* among the lines in the plots is a measure of the

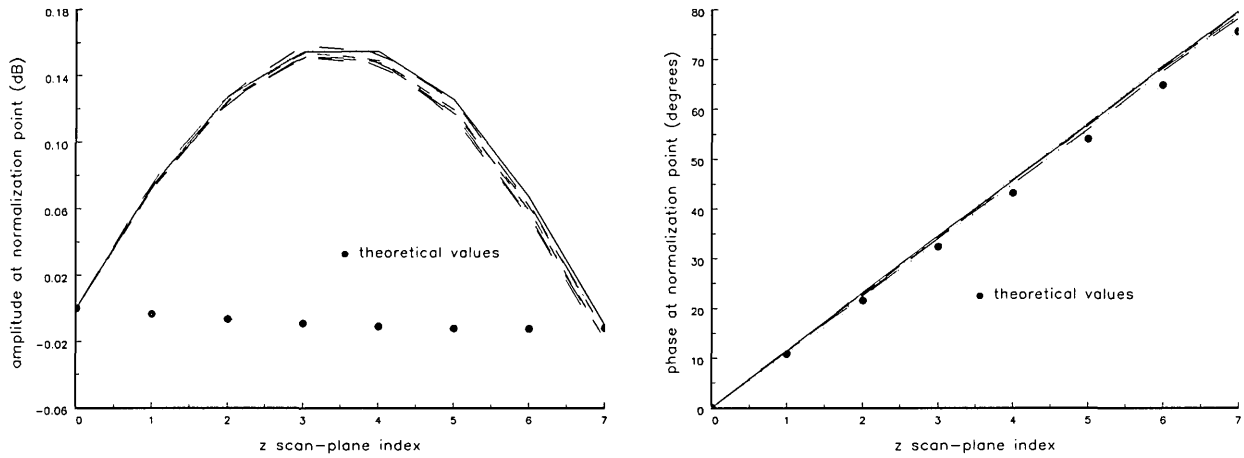

Fig. 3. The repeatability of measurements. The set of measurements show the relative amplitudes (left) and phases (right) at the normalization point as a function of z scan-plane index. Errors increase as z increases. Theoretical normalization points, partially eliminating multiple reflection effects, are also shown.

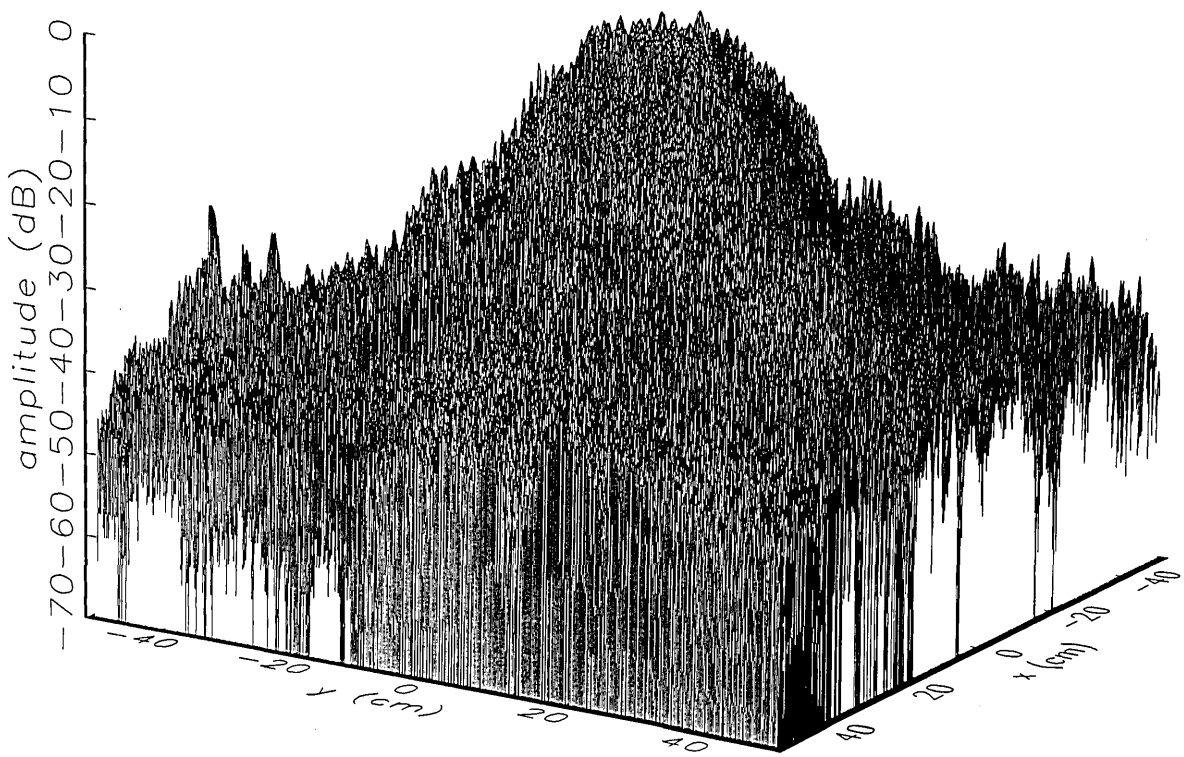

Fig. 4. The near field of the center-fed Cassegrain parabolic reflector antenna used in the experiment. The antenna was 0.5 m in diameter and operates at 60 GHz.

experimental factors present, as discussed in Sec. 1. Of these, *multiple reflections* are thought to be the most significant, but an independent verification of this interpretation at 60 GHz has not been pursued. We also observe greater vertical spread in Fig. 5a than in Fig. 5c, indicating that errors in the x coordinates might be greater than in the y coordinates.

4. Error-Contaminated Near Fields

We want to establish to what extent error correction is effected when it is applied to real rather than simulated data. To accomplish this we compare two error-contaminated fields created computationally (which contain no experimental contamination) and the error-contaminated fields obtained experimentally.

Figures 6 and 7 show the continuous and discrete probe position-error functions used to obtain simulated error-contaminated near fields. We performed simulations using the discrete error function to observe any possible significant consequence to the error-correction technique due to discretization, although no serious differences were expected.

Figure 8 shows the amplitude and phase of the ratio of the error-contaminated and error-free near fields when the continuous error function was used to generate the error-contaminated field; Fig. 9 shows the corresponding fields when the discrete error function was used. The nine-lobe structure of the error function is clearly discernible in each of these plots. In the case of discrete errors the error-contaminated region is more sharply delineated from the background, where the error in the amplitude ratio is 0 dB, and the phase errors show up in discrete steps rather than as a continuous surface. These features were expected, as they mirror the structure of the error function. As is shown in the next section, these differences in the error-contaminated fields do not effect the success of the error correction to any significant degree.

We constructed an error-contaminated near field from the measurements according to the technique described in Sec. 3. The amplitude and phase of the ratio of this field to the error-free near field obtained at z_0 are shown in Fig. 10. There seems to be more rapid and pronounced oscillations in the amplitude errors when compared to the errors shown in Fig. 9. We cannot tell at this point to what extent such a difference will degrade the effectiveness of the error correction.

To further observe the differences between simulated and measured error-contaminated near fields discussed in the preceding paragraphs, we enlarged the center (main beam) region of the plots shown in Figs. 8–10. Some small-scale features in these plots are worthy of observation. We observe that the simulated error amplitude ratios (Figs. 11a and 12a) differ little, but that the measured error amplitude ratio (Fig. 13a) is significantly different when compared to simulations. Further the steps in the discrete phase plots are a lot smoother for the simulated field (Fig. 12b) than for the field constructed from data (Fig. 13b). Each of the effects listed in the introduction, *multiple reflections, residual drift,* and *residual probe position errors*, has probably contributed to this difference. We anticipate that this difference in the phase will effect the accuracy of the error correction, since near-field phase errors are the most significant source of errors in the far field. We cannot, however, predict to what extent the error correction will be effected, since the whole procedure is a nonlinear function of the error fields and of the position errors [see Eq. (5)].

5. Error-Corrected Fields

We applied the error-correction technique [Eq. (5)] to the error-contaminated near fields discussed in the previous section. Again, a comparison of the results of the error correction applied to simulated and to measured data will reveal the extent to which experimental effects in the data confirm the success of the technique. We also transformed all near fields to obtain the corresponding far fields. As will be seen in the subsection below, comparison of the far fields demonstrates that the error-correction technique is successful for real data both in the main beam and sidelobe directions. In the sidelobe directions, however, the simulated data yield slightly better results.

5.1 Error-Corrected Near Fields

In Figs. 14 and 15 we show the main beam portion of the ratios of *simulated* error-corrected near fields to the error-free near field for the continuous and the discrete probe position-error functions, respectively. Both the amplitude and phase surfaces seem to be well defined with a few minor irregular features, and the magnitudes are very close to 0 (a case which would indicate no residual errors). The structure of the residual error surfaces clearly reflect the continuous or discrete nature of the position error function. The phase surface in Fig. 15b clearly brings out the nonlinearity of the correction, since each step in the error-contaminated field is of equal height originally (see Fig. 13b).

Figure 16 shows the result of the error correction when measured data are used. The well-defined structures observed in Figs. 14 and 15 are no longer present. When the error-contaminated amplitude ratio (Fig. 13a) is compared with the error-corrected amplitude ratio (Fig. 16a), we observe some improvements, but the success of the error correction is not obvious. The well-defined residual error surface observed with the simulated data is not apparent. Comparing the error-contaminated phase differences (Fig. 13b) with the error-corrected phase differences (Fig. 16b), we see that the discrete phase structure has been altered to what is essentially a random surface made up of single point ridges and spikes. The residual error surface obtained with simulated data is not discernible; most likely it is buried beneath the spikes. Nevertheless, the lack of a discrete structure, together with a decrease in the maxima of the phase plots, indicates that phase correction has occurred.

5.2 Error-Corrected Far Fields

In Figs. 17–19 we show the results of near-field to far-field transformations. In these center-cut plots we superimposed the error-contaminated, error-corrected and error-free far fields. (These datasets are drawn with solid circles connected with dotted line, open circles connected with a solid line, and a solid line, respectively.) Figure 17 shows these results obtained from measured data for the full range of k_x and k_y; because of the density of points, essential details of the results are not discernible, except at maxima and minima of the cuts, where the success of the error correction is apparent. To observe more detail, we enlarged these center cuts between $k_x = k_y = \pm 0.3$ both for simulated and measured data

In Fig. 18 we compare the results of the error correction using simulated error-contaminated fields. Here only single solid lines connecting the open circles are observed. This is readily interpreted to show that the error-corrected and error-free values overlap on the scale of this plot; that is, the error correction fully succeeds. Indeed, the maximum error in the spectrum [7] that appears at $k_x = k_y = (12\pi/L)k = 0.03k$ induced by the periodic error function used in this simulation is fully removed.

In Fig. 19 we compare the results of the error correction using error-contaminated fields obtained from real measured data. We now see two solid lines, one with open circles, that do not overlap everywhere, and solid circles connected with dotted lines. We observe the difference between the error-free and error-corrected lines to be much less than the difference between the error-free and error-contaminated data at most of the data points. We thus conclude that we can *almost* recover the error-free far field from measured error-contaminated near fields by applying the probe-position error correction, but *residual errors will be present*. We again observe that the maximum error in the spectrum at $k_x = k_y = (12\pi/L)k = 0.03k$ is removed, as in Fig. 18, but a very small residual error is visible in this region. The magnitudes of these residual errors, and those elsewhere, are at acceptable levels.

6. Suggestions for Further Study

The residual errors observed in Fig. 19 are due to the experimental factors enumerated in the introduction. Further reduction of these errors could be obtained by altering the measurement and/or data analysis process with such sources of experimental errors in mind. Some steps that need or could be taken to improve accuracy of measured near fields will be briefly examined here.

6.1 Multiple Reflections

Standard near-field measurement seeks to minimize multiple reflections by appropriately choosing the distance between the probe and the antenna under test. Residual multiple reflections, still present in the data, could possibly be removed by some filtering and/or averaging technique. In Fig. 3 we have shown theoretical normalization values, which were derived by transforming the near field at z_0 to obtain the far field, filtering the evanescent modes, and then transforming back to the various near-field scan planes. This procedure provides normalization values for a *fictitious* near field that is a composite of the actual *(filtered)* near field of the antenna and the real modes of the multiple reflections present in the data. When such near-field data are transformed from scan plane to scan plane, the transformations occur in a *reflectionless environment*. Alternatively, the far fields obtained from the various near fields can be averaged and transformed back to a near-field plane. In this manner some of the multiple reflections can be removed from the data, and the effect of multiple reflections on the error correction technique can be studied. Neither of these approaches, however, removes all of the multiple reflections, since multiple reflections are not treated as a realistic function of x and y. Currently, no manageable analytic technique that can accomplish this is known.

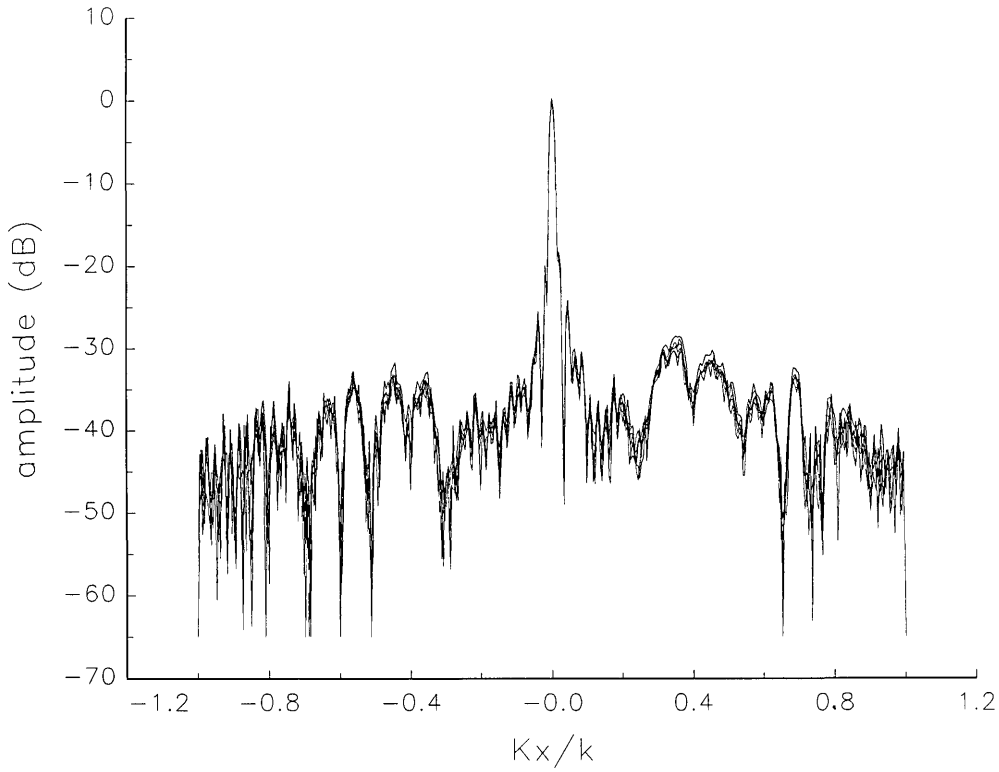

Fig. 5a. *Nonoverlapping* far fields as functions of k_x derived from the near fields measured on six scan planes z_0 to z_5. Theoretically, the far fields should be exactly the same, so the differences can be safely attributed to experimental effects as discussed in the text.

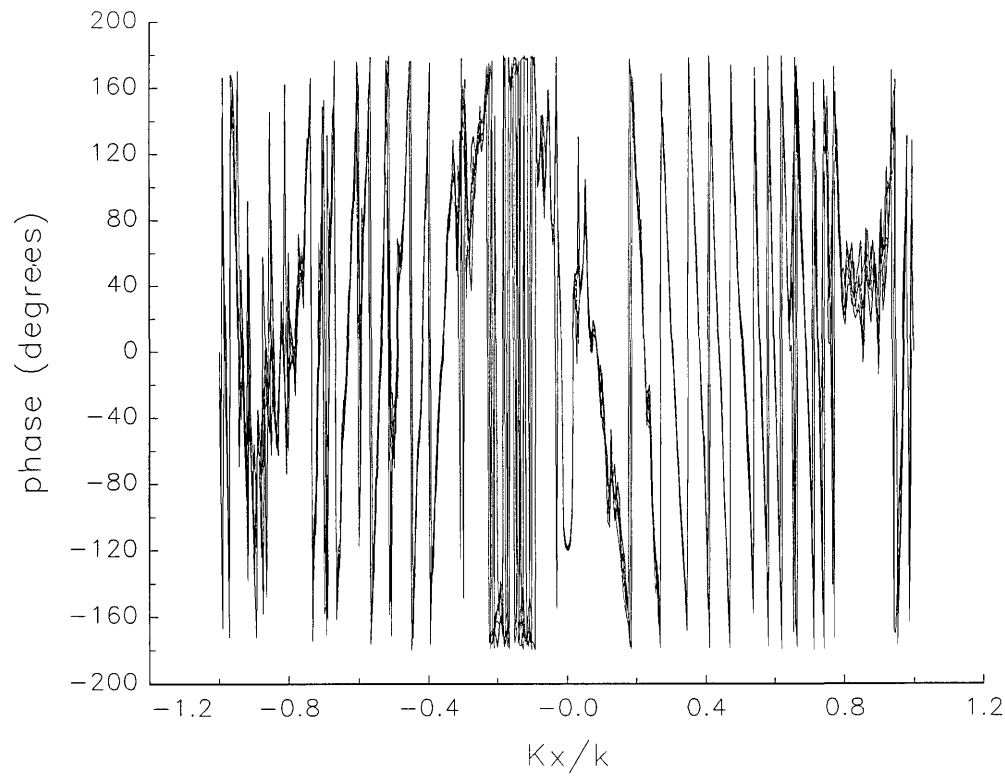

Fig. 5b. The phases of the *nonoverlapping* far fields shown in Fig. 5a.

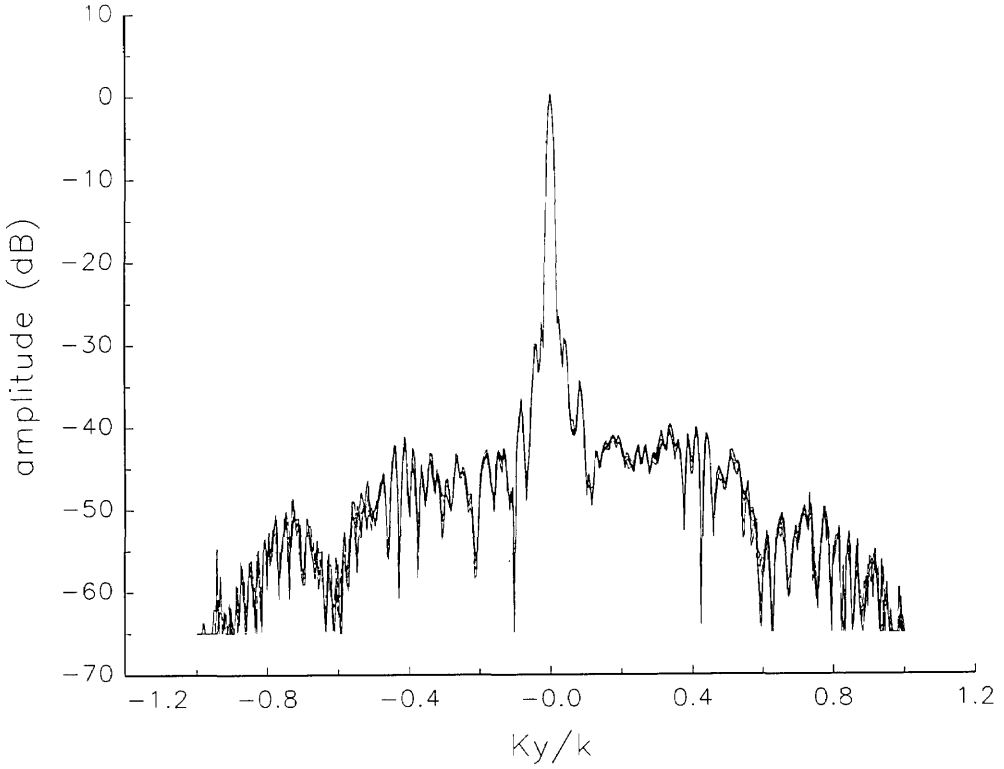

Fig. 5c. The amplitudes of the *nonoverlapping* far fields as functions of k_y (see Fig. 5a).

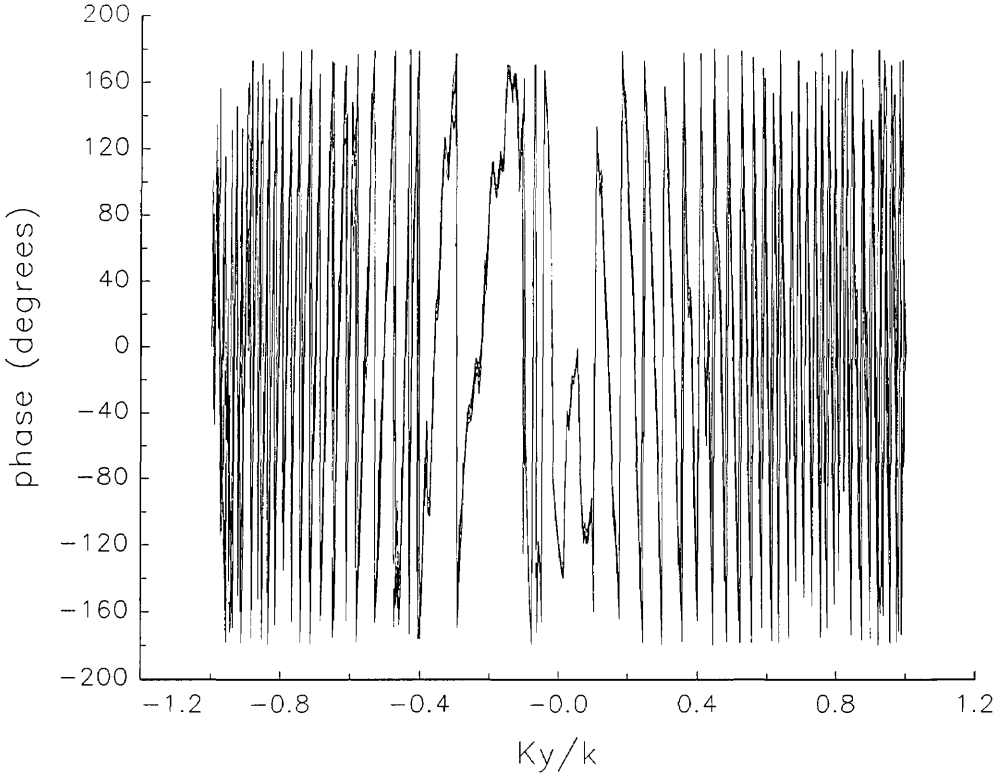

Fig. 5d. The phases of the *nonoverlapping* far fields as functions of k_y (see Fig. 5a).

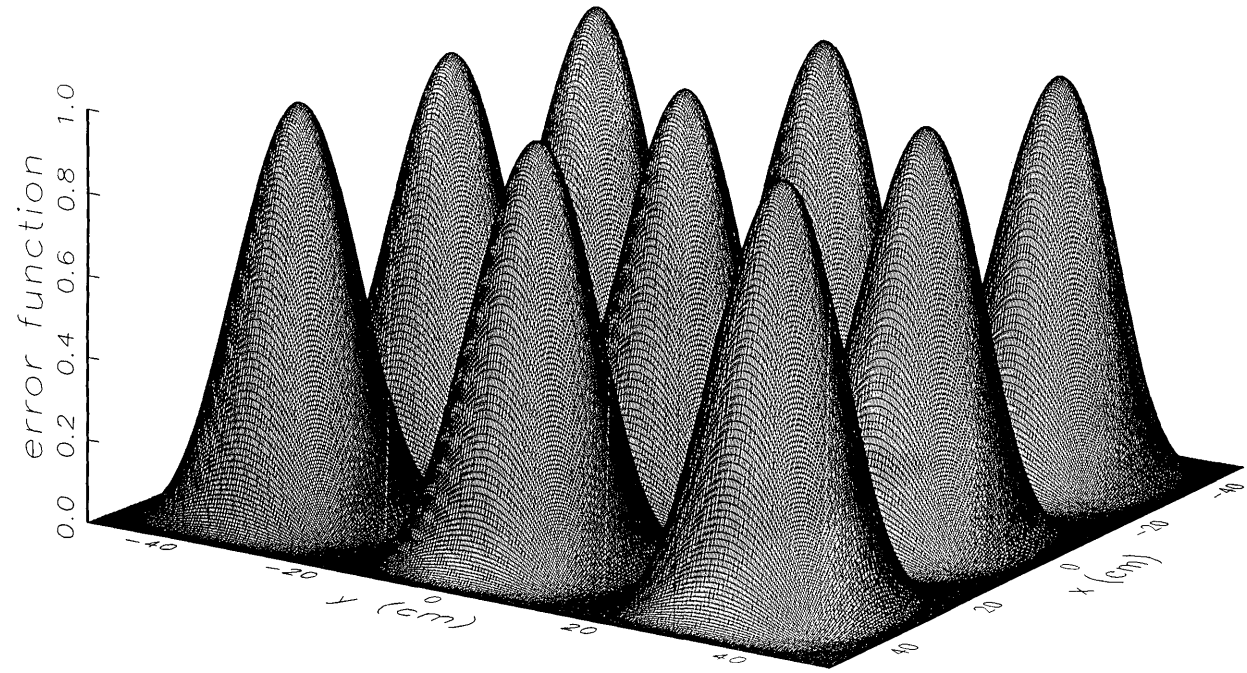

Fig. 6. The theoretical probe position-error function used in the simulations. The error surface is given by $z = \Delta z \cos^2(3\alpha x)\cos^2(3\alpha y)$, where $\alpha = 2\pi/L$.

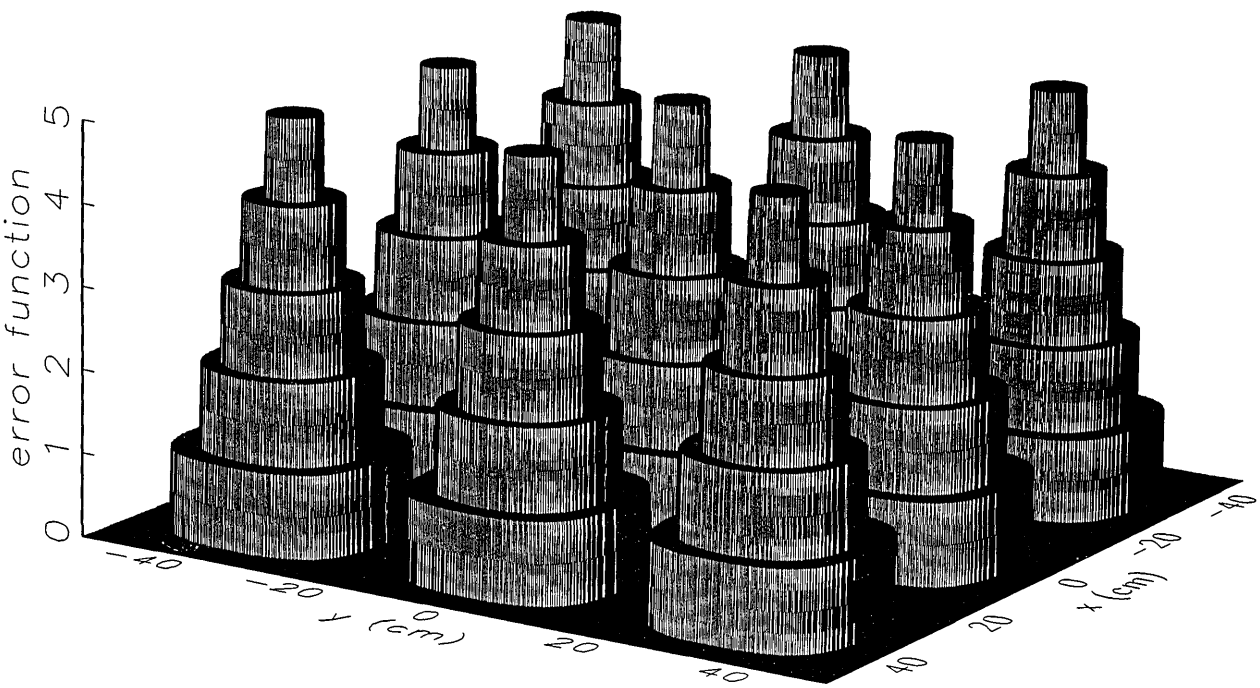

Fig. 7. The discrete probe position error function. The discrete error surface is given by $z = \delta z\ \mathrm{int}[N\cos^2(3\alpha x)\cos^2(3\alpha y) + 0.5]$, where $N = 5$ is the maximum scan plane index, int is the fortran *truncate-to-integer* function, and $\alpha = 2\pi/L$.

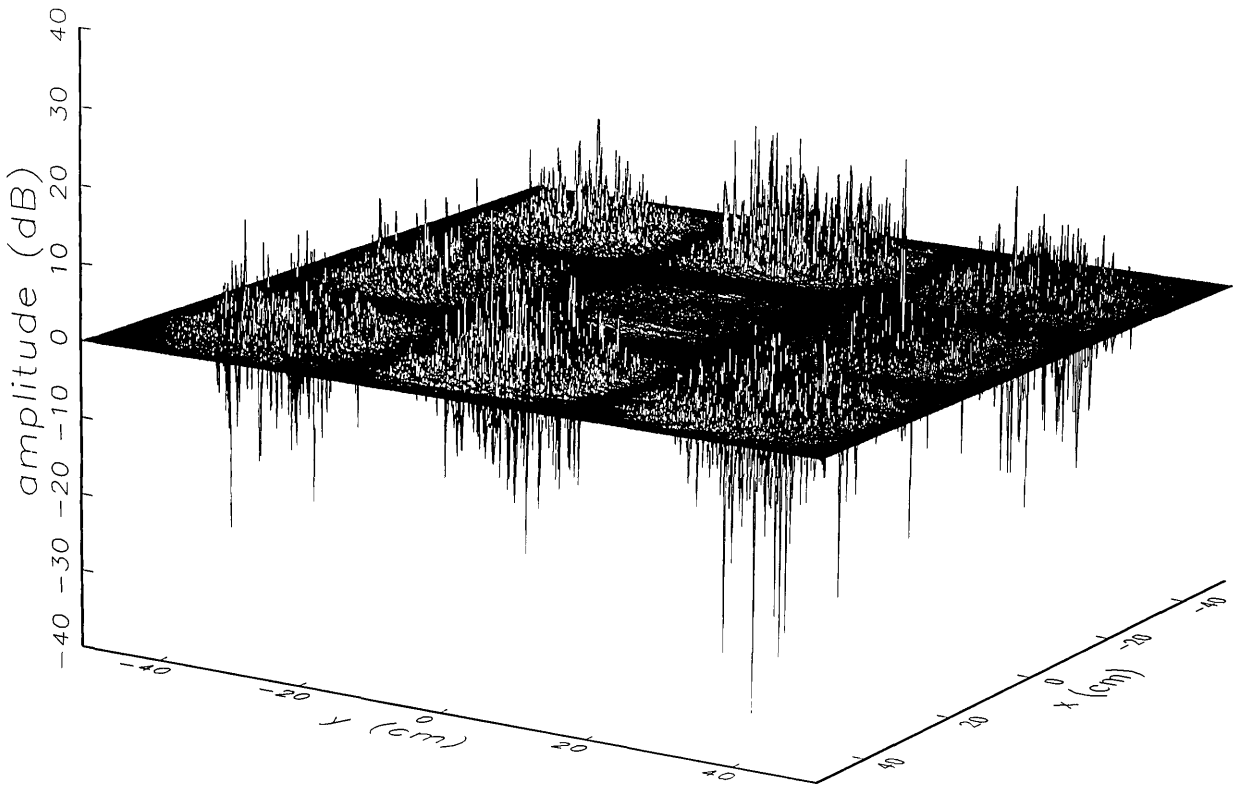

Fig. 8a. The ratio of the *simulated* error-contaminated and error-free near-field amplitudes when the *continuous* error function in Fig. 6 is used.

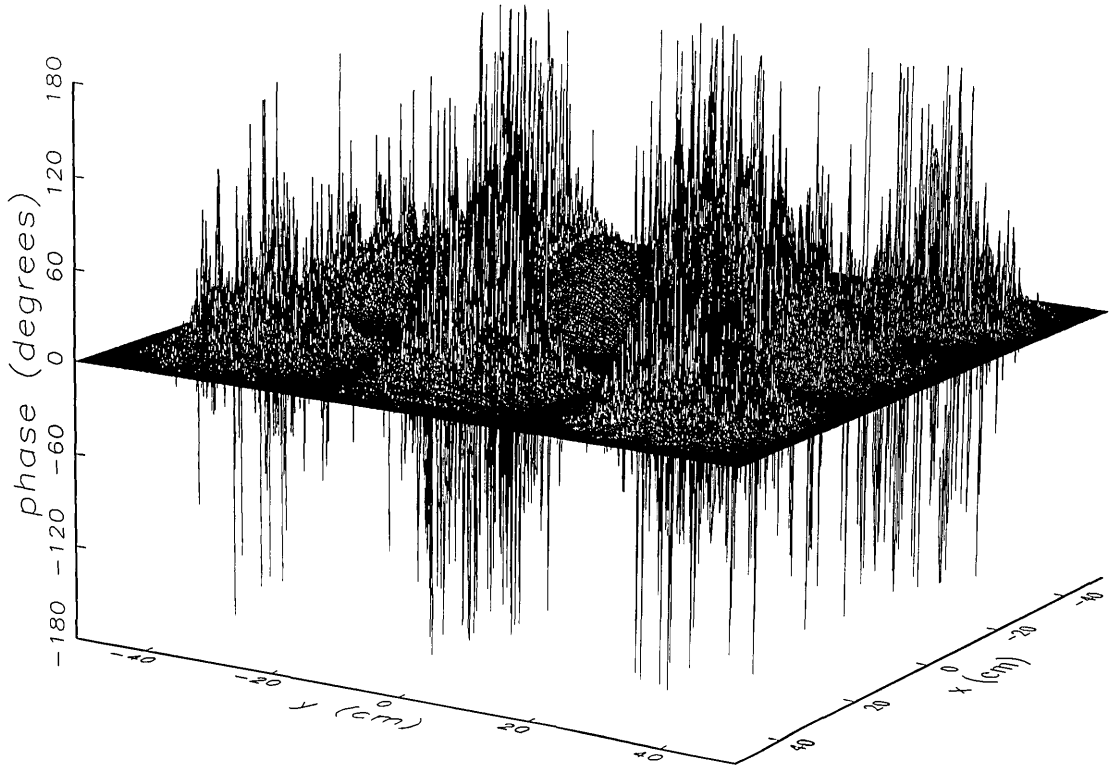

Fig. 8b. The phase difference between the *simulated* error-contaminated and error-free near fields when the *continuous* error function in Fig. 6 is used.

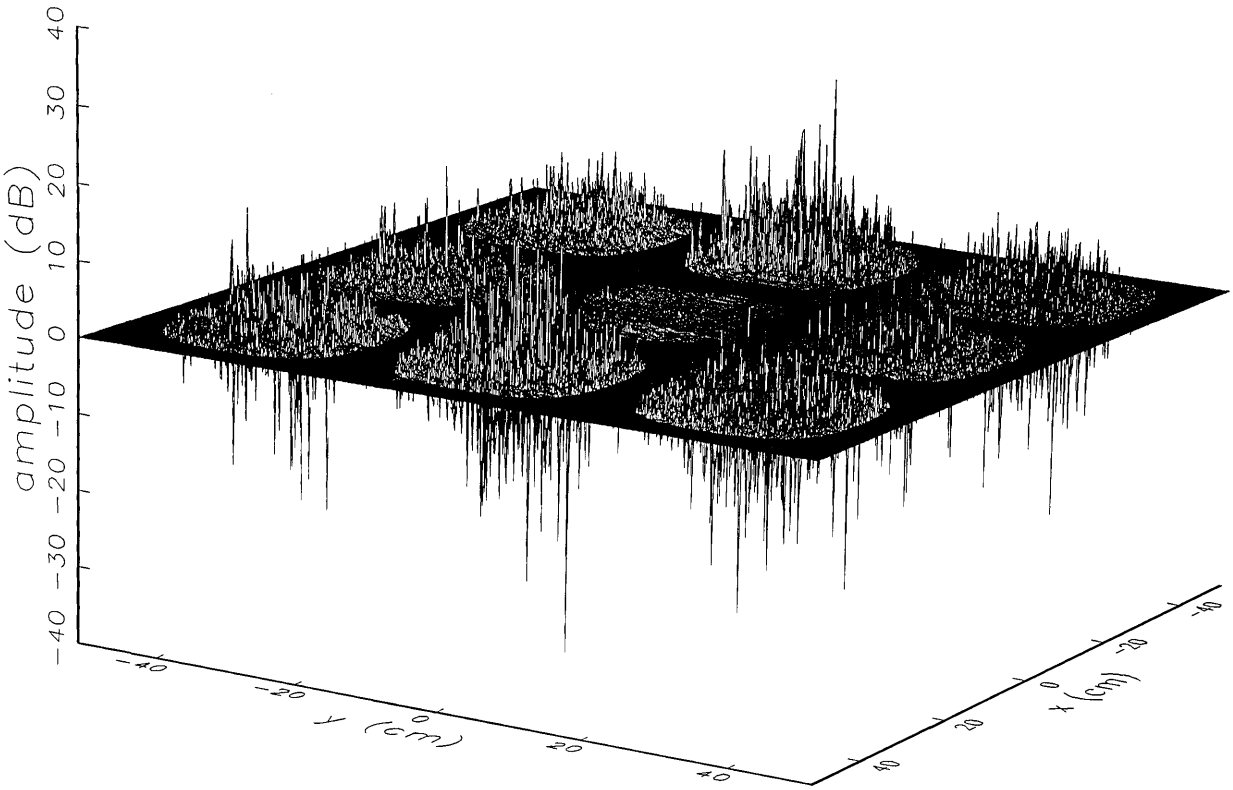

Fig. 9a. The ratio of the *simulated* error-contaminated and error-free near-field amplitudes when the *discrete* error function in Fig. 7 is used.

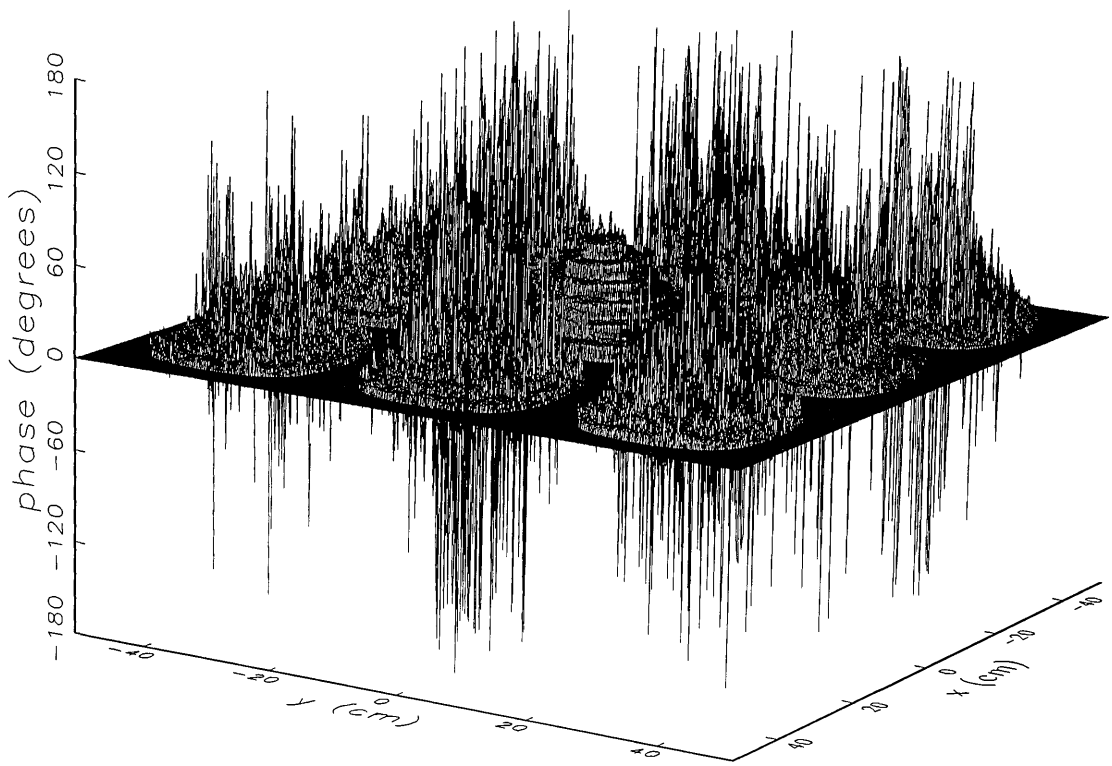

Fig. 9b. The phase difference between the *simulated* error-contaminated and error-free near fields when the *discrete* error function in Fig. 7 is used.

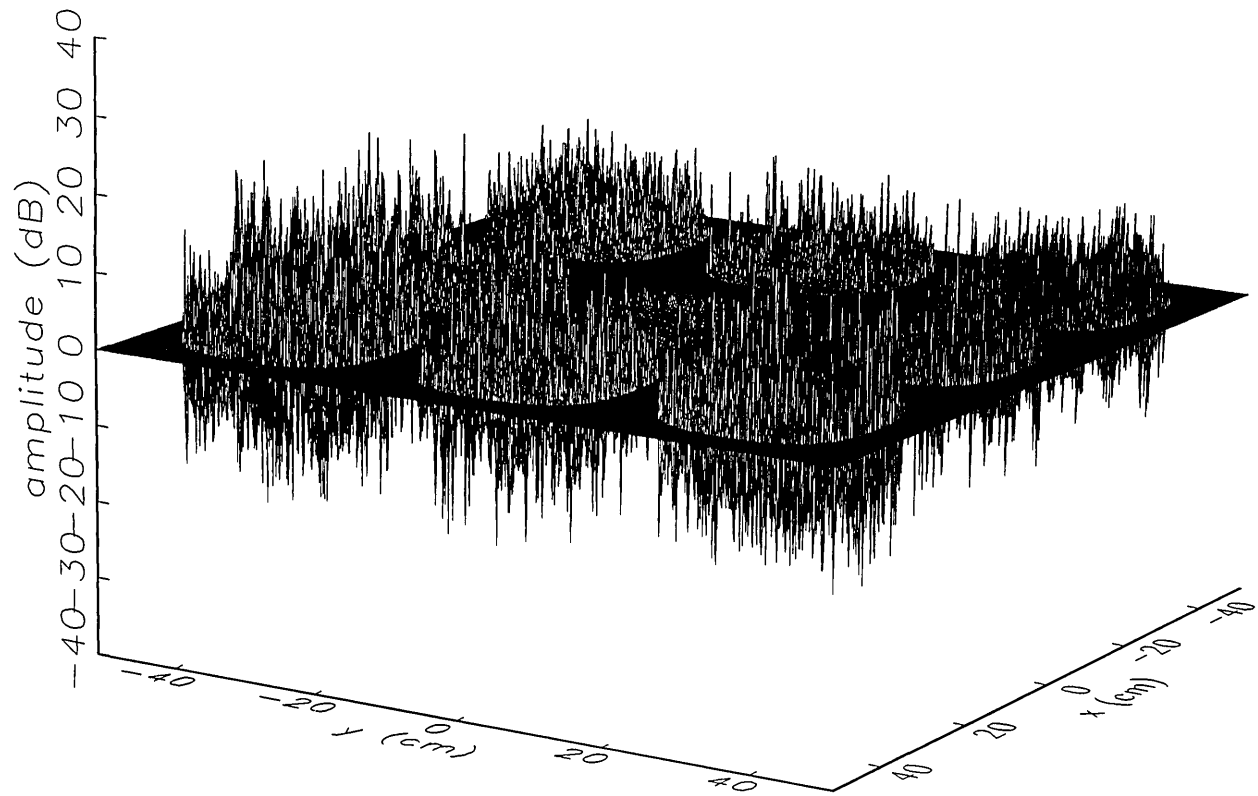

Fig. 10a. The ratio of the error-contaminated and the error-free near-field amplitudes when the *discrete* error function in Fig. 7 is used to construct the error-contaminated near field from measurements.

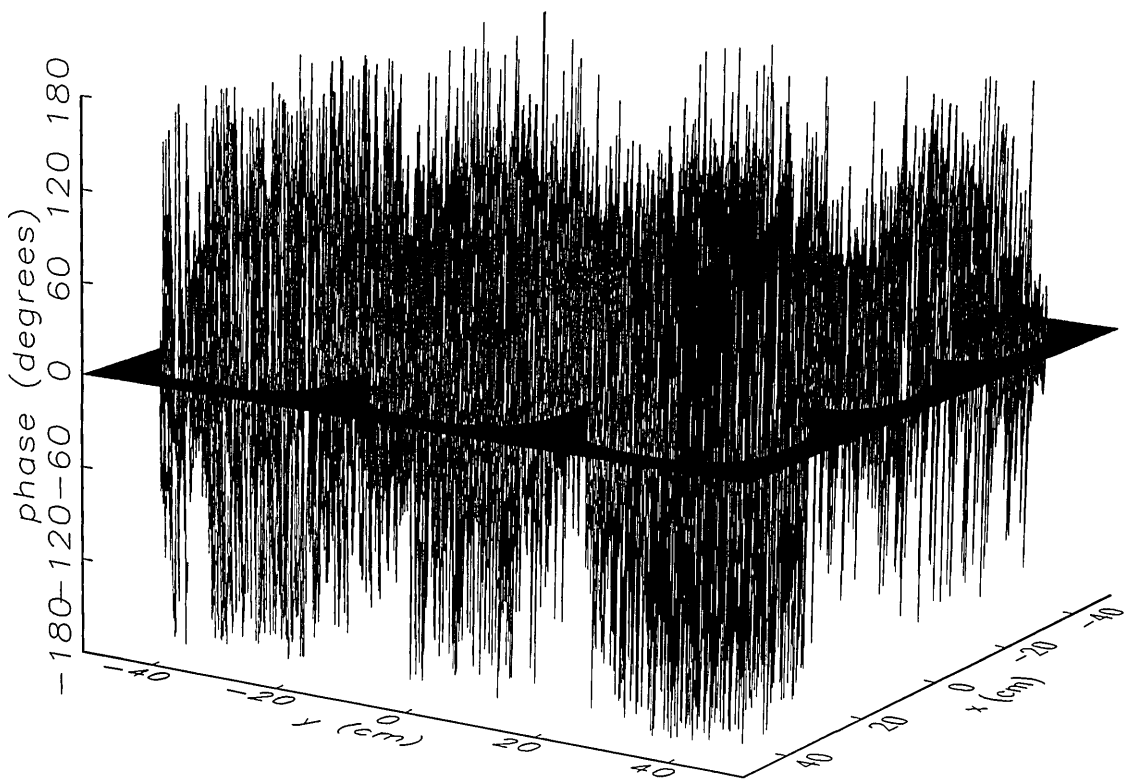

Fig. 10b. The phase difference between the error-contaminated and the error-free near-fields when the *discrete* error function in Fig. 7 is used to construct the error-contaminated near field from measurements.

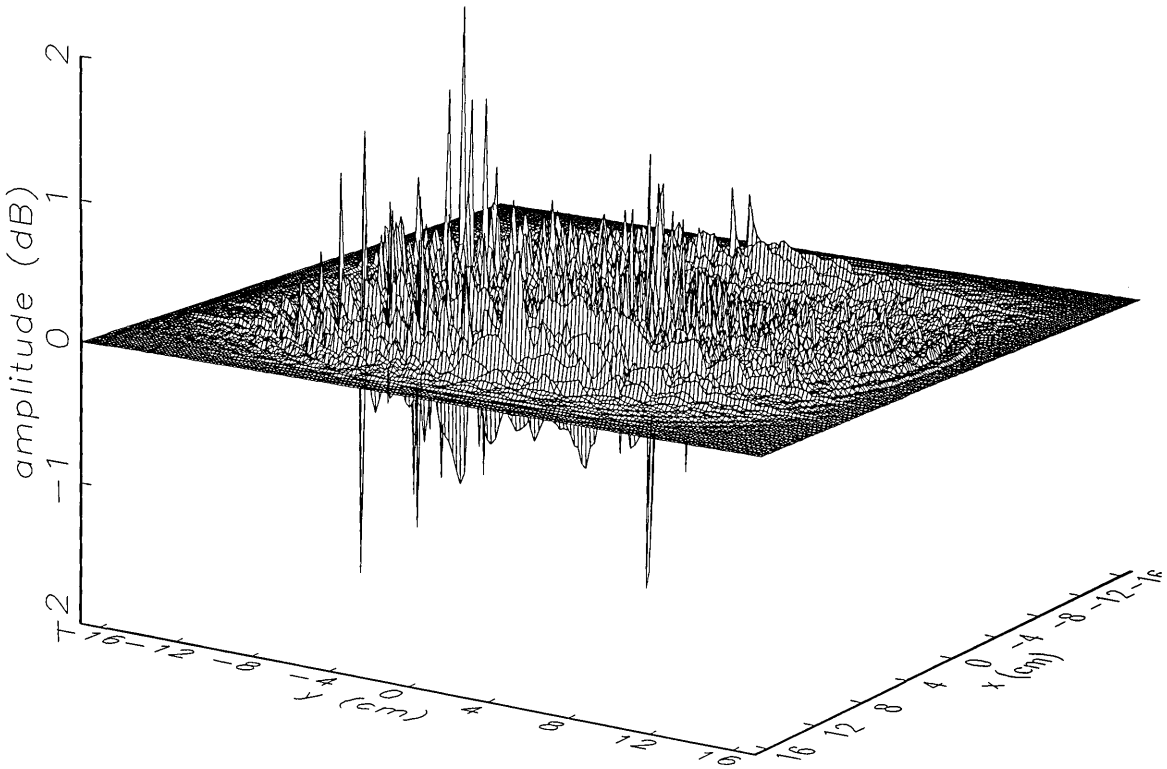

Fig. 11a. The center (main beam) portion of the the ratio of the *simulated* error-contaminated and error-free near-field amplitudes when the *continuous* error function in Fig. 6 is used (see Fig. 8a).

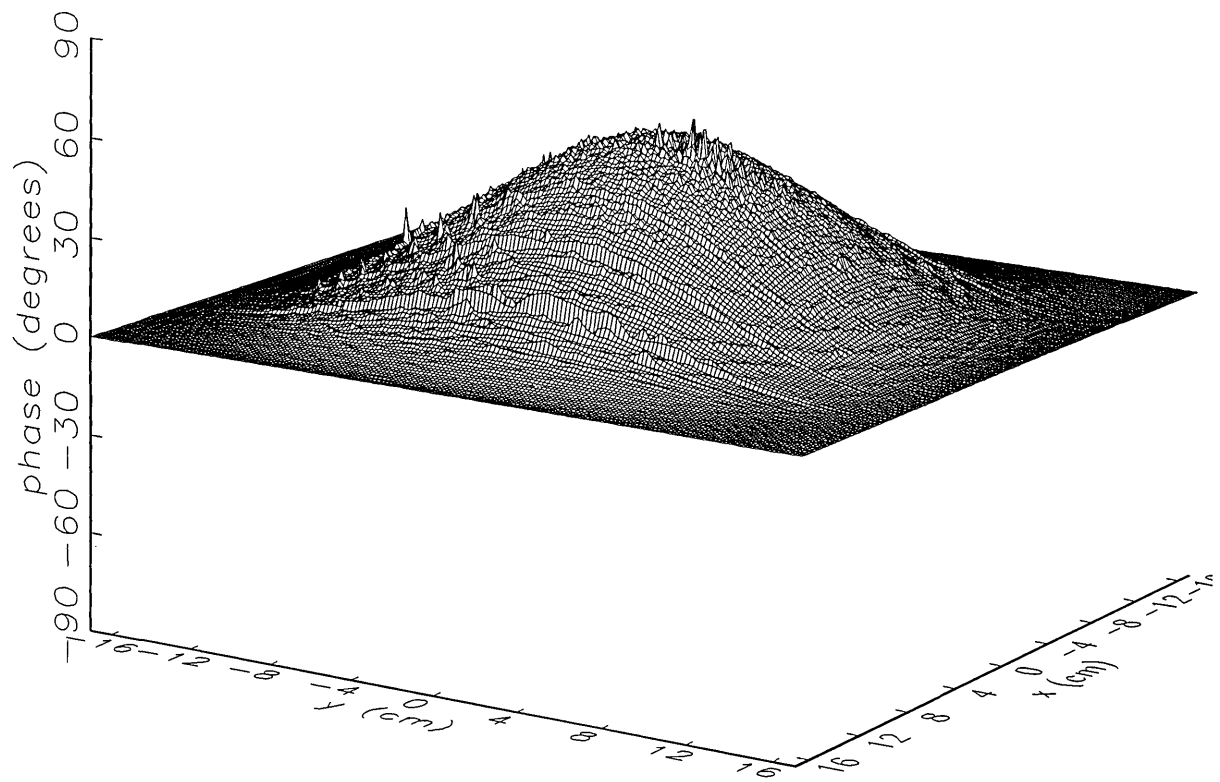

Fig. 11b. The center (main beam) portion of the phase difference between the *simulated* error-contaminated and error-free near fields when the *continuous* error function in Fig. 6 is used (see Fig. 8b).

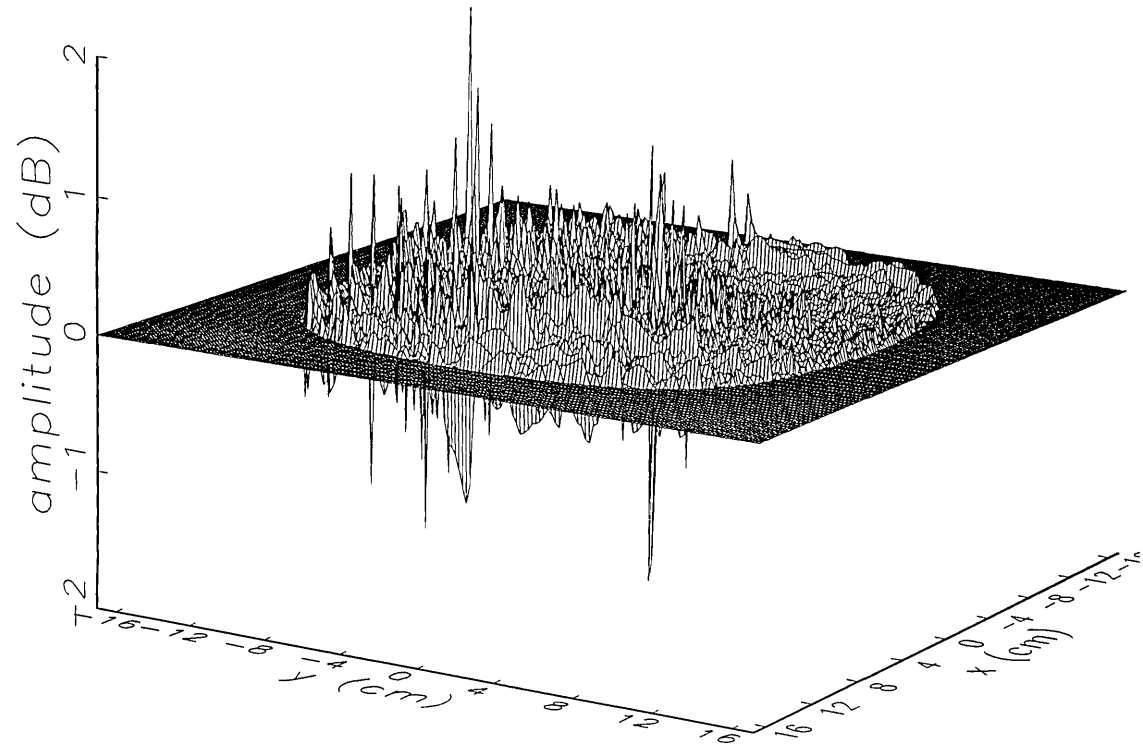

Fig. 12a. The center (main beam) portion of the ratio of the *simulated* error-contaminated and error-free near-field amplitudes when the *discrete* error function in Fig. 7 is used (see Fig. 9a).

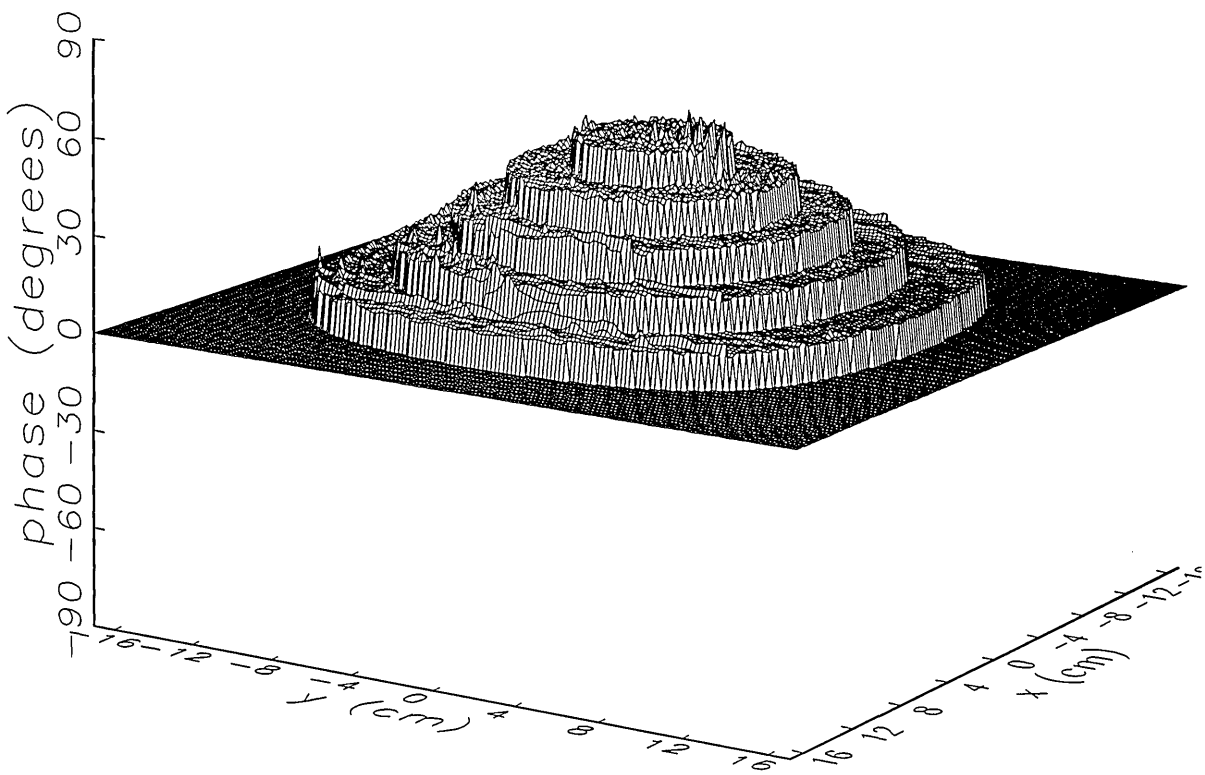

Fig. 12b. The center (main beam) portion of the phase difference between the *simulated* error-contaminated and error-free near fields when the *discrete* error function in Fig. 7 is used (see Fig. 9b).

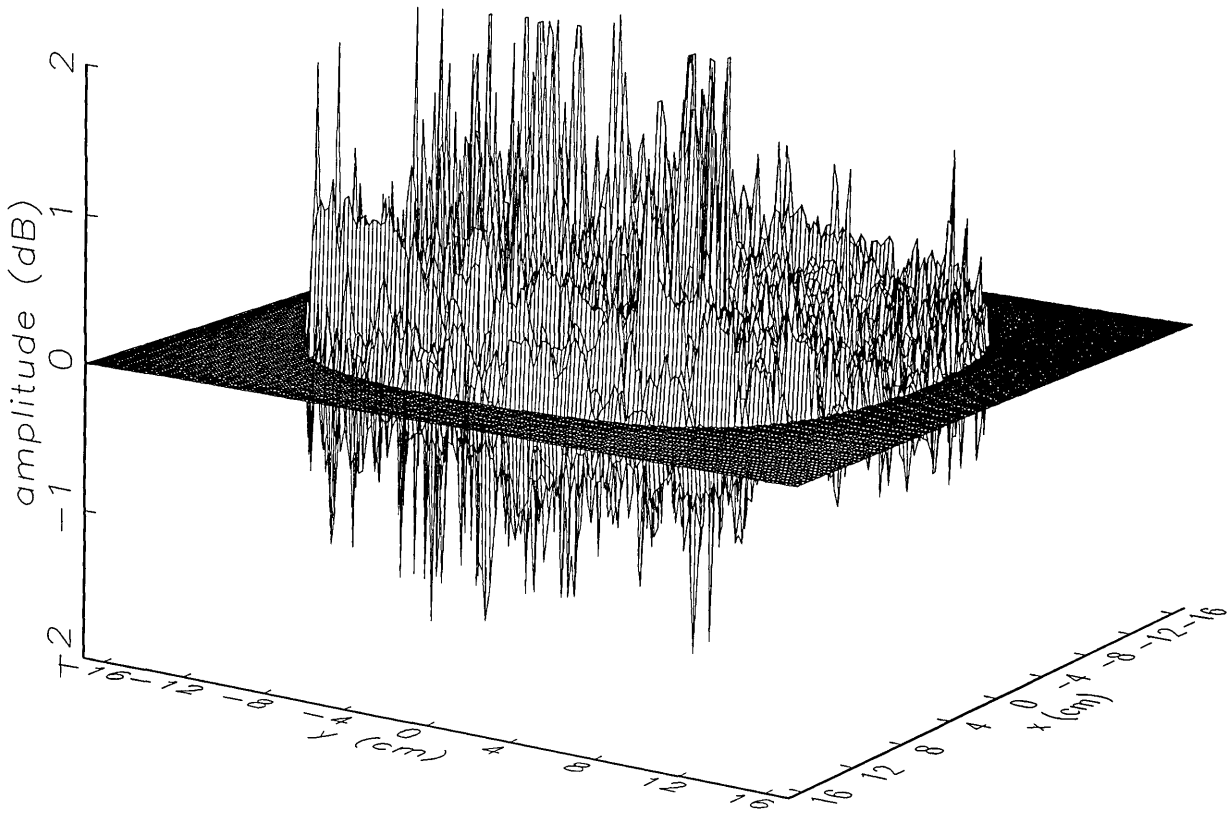

Fig. 13a. The center (main beam) portion of the ratio of the error-contaminated and the error-free near-field amplitudes when the *discrete* error function in Fig. 7 is used to construct the error-contaminated near field from measurements (see Fig. 10a).

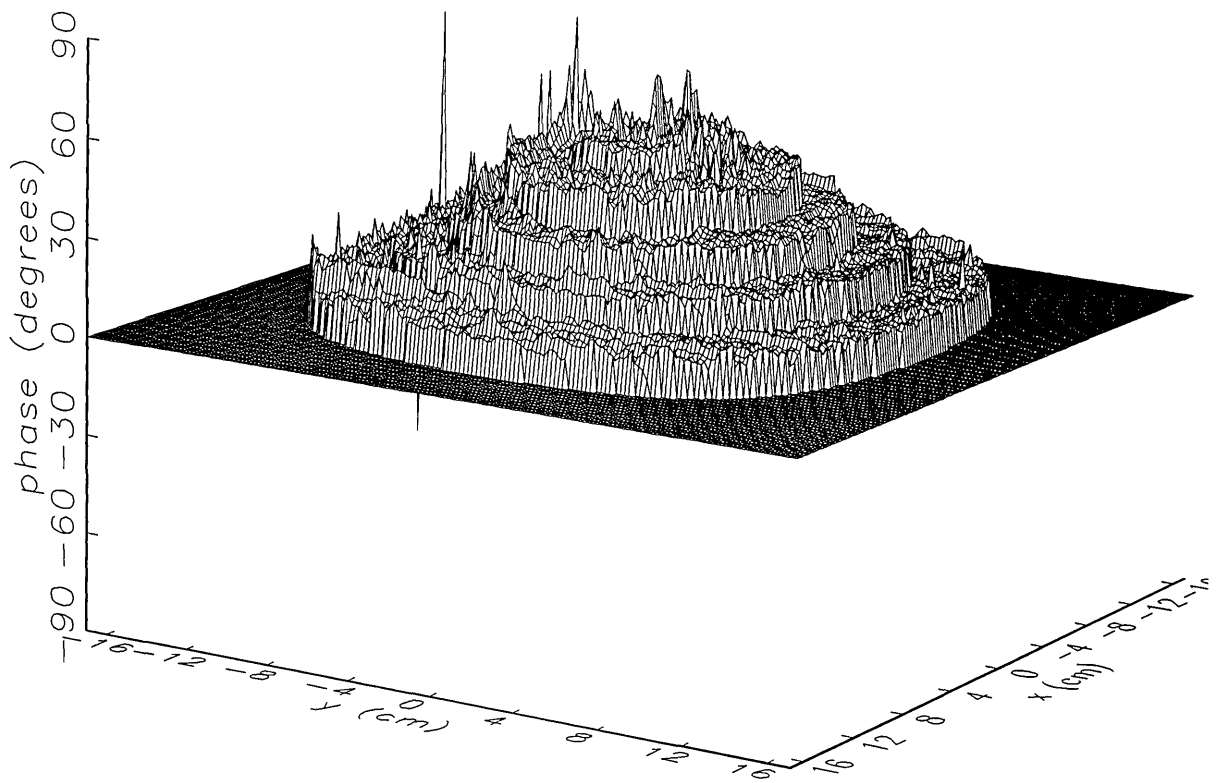

Fig. 13b. The center (main beam) portion of the phase difference between the error-contaminated and the error-free near-fields when the *discrete* error function in Fig. 7 is used to construct the error-contaminated near field from measurements (see Fig. 10b).

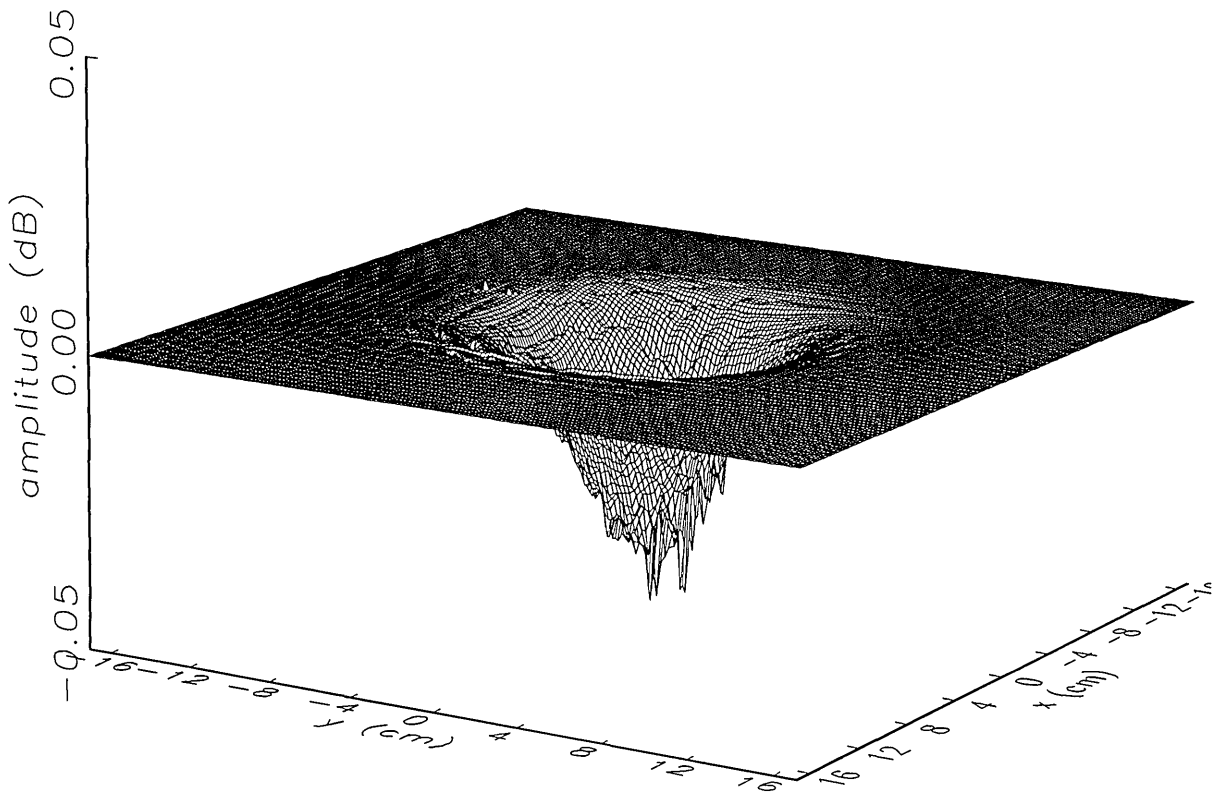

Fig. 14a. The center (main beam) portion of the ratio of the *simulated* error-corrected and error-free near-field amplitudes when the *continuous* error function in Fig. 6 is used.

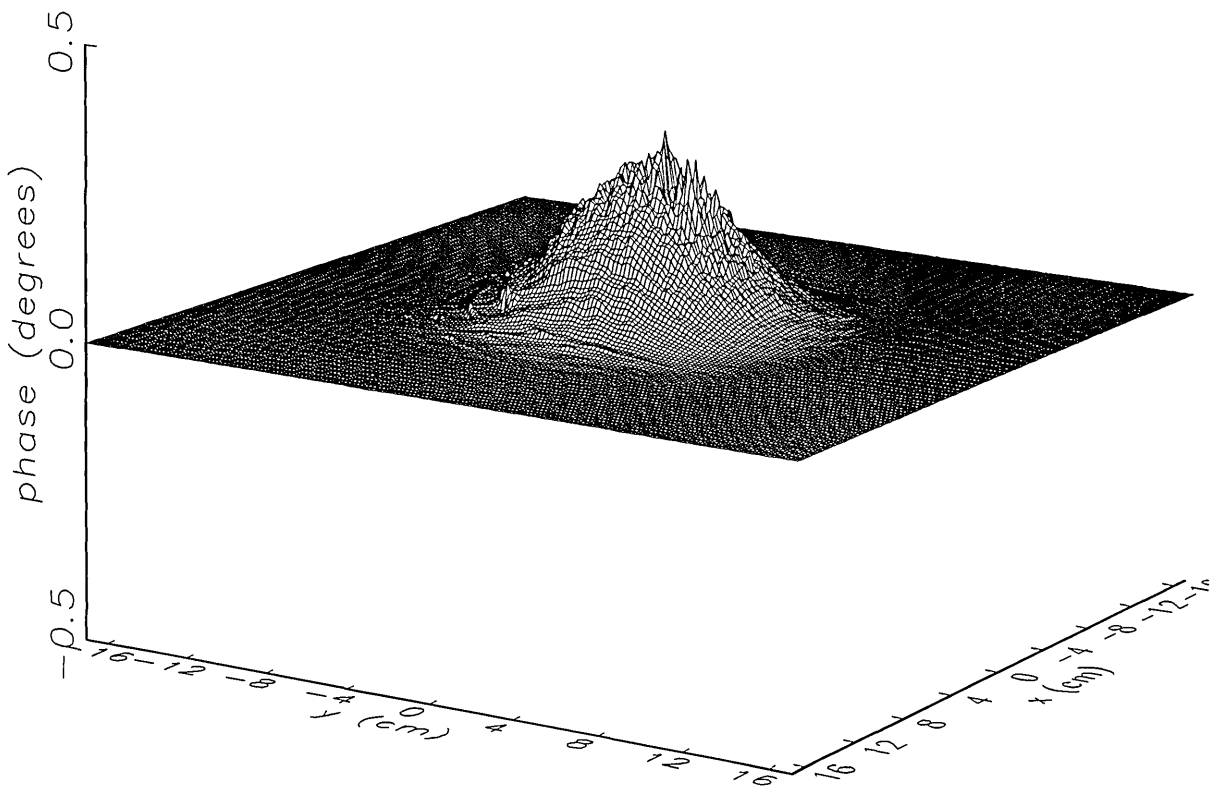

Fig. 14b. The center (main beam) portion of the phase difference between the *simulated* error-corrected and error-free near fields when the *continuous* error function in Fig. 6 is used.

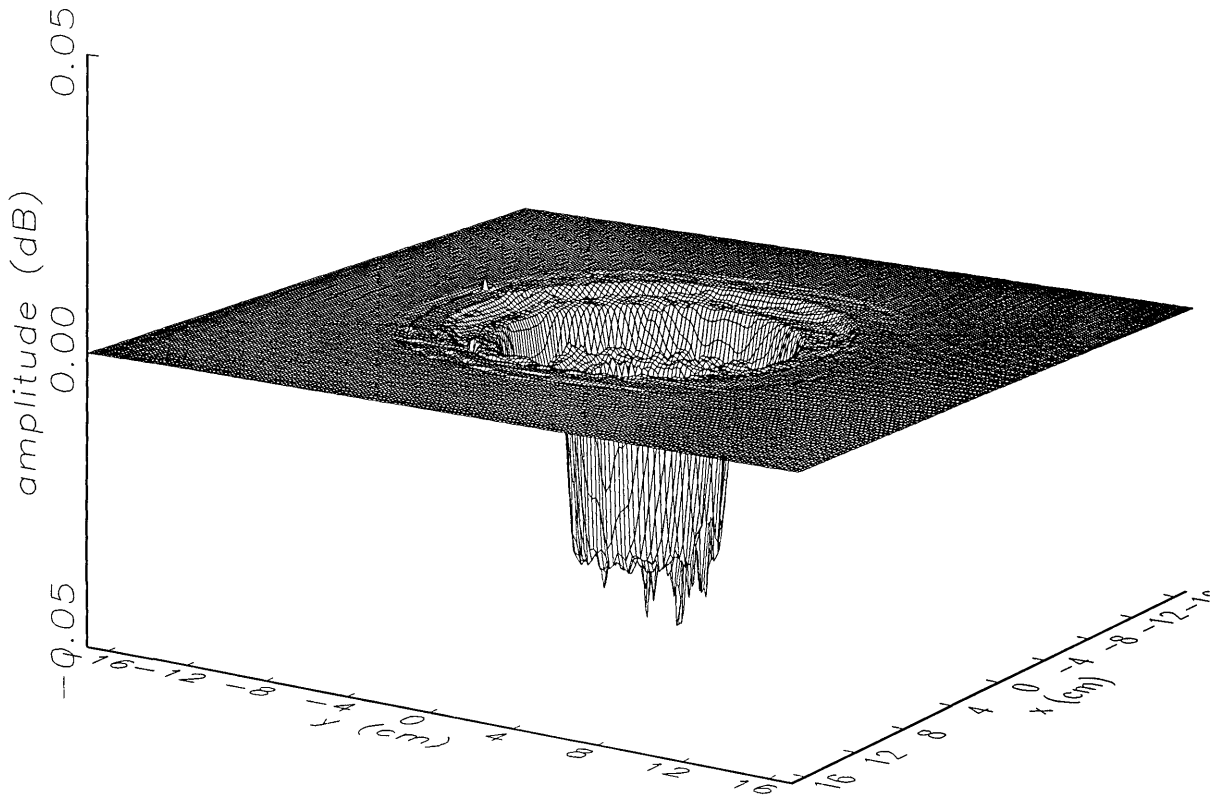

Fig. 15a. The center (main beam) portion of the ratio of the *simulated* error-corrected and error-free near-field amplitudes when the *discrete* error function in Fig. 7 is used.

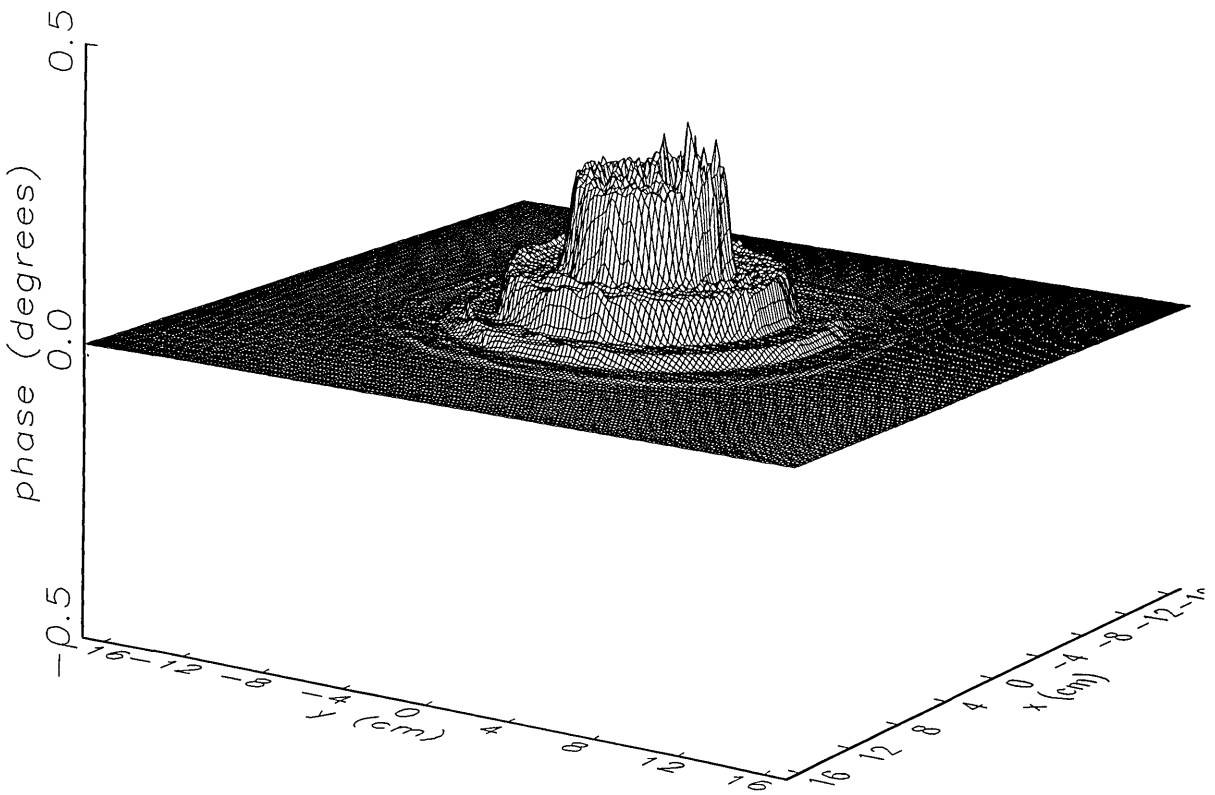

Fig. 15b. The center (main beam) portion of the phase difference between the *simulated* error-corrected and error-free near fields when the *discrete* error function in Fig. 7 is used.

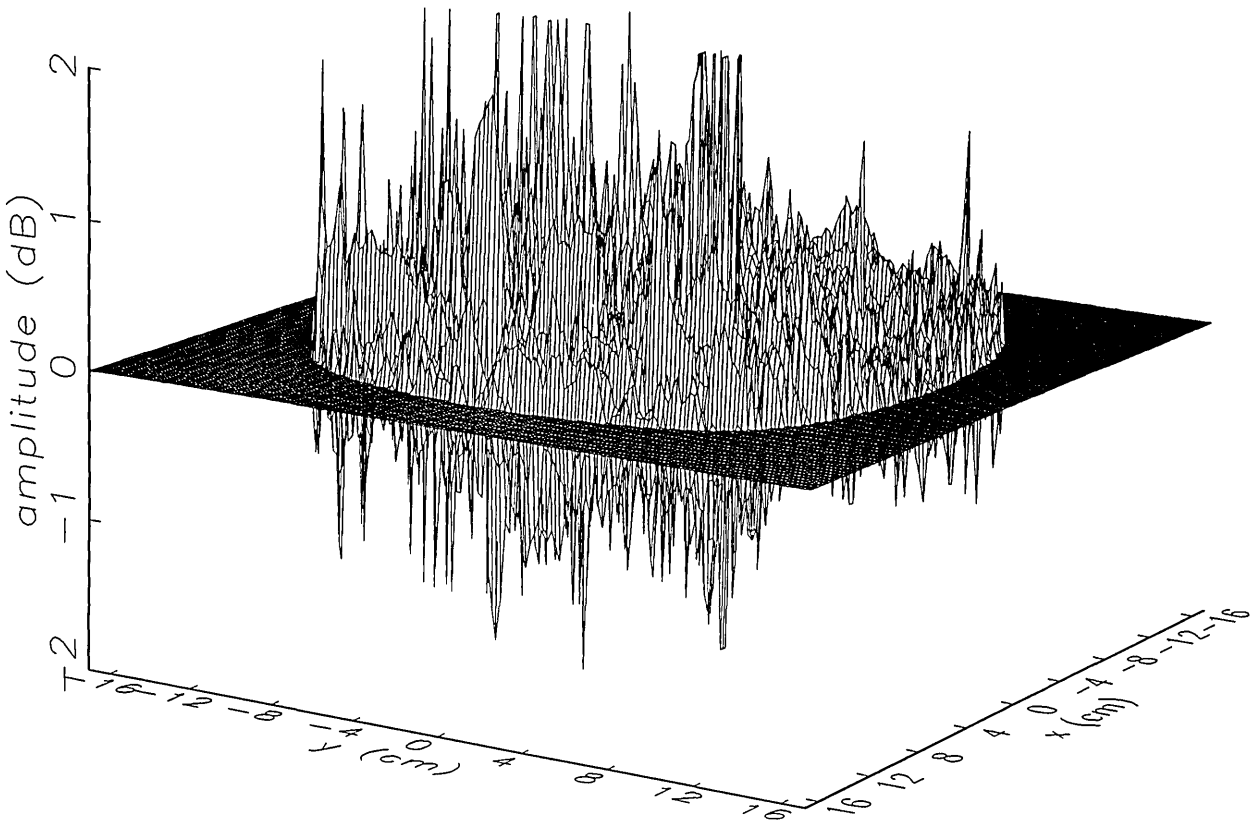

Fig. 16a. The center (main beam) portion of the ratio of the error-corrected and the error-free near-field amplitudes when the *discrete* error function in Fig. 7 is used to construct the error-contaminated near field from measurements.

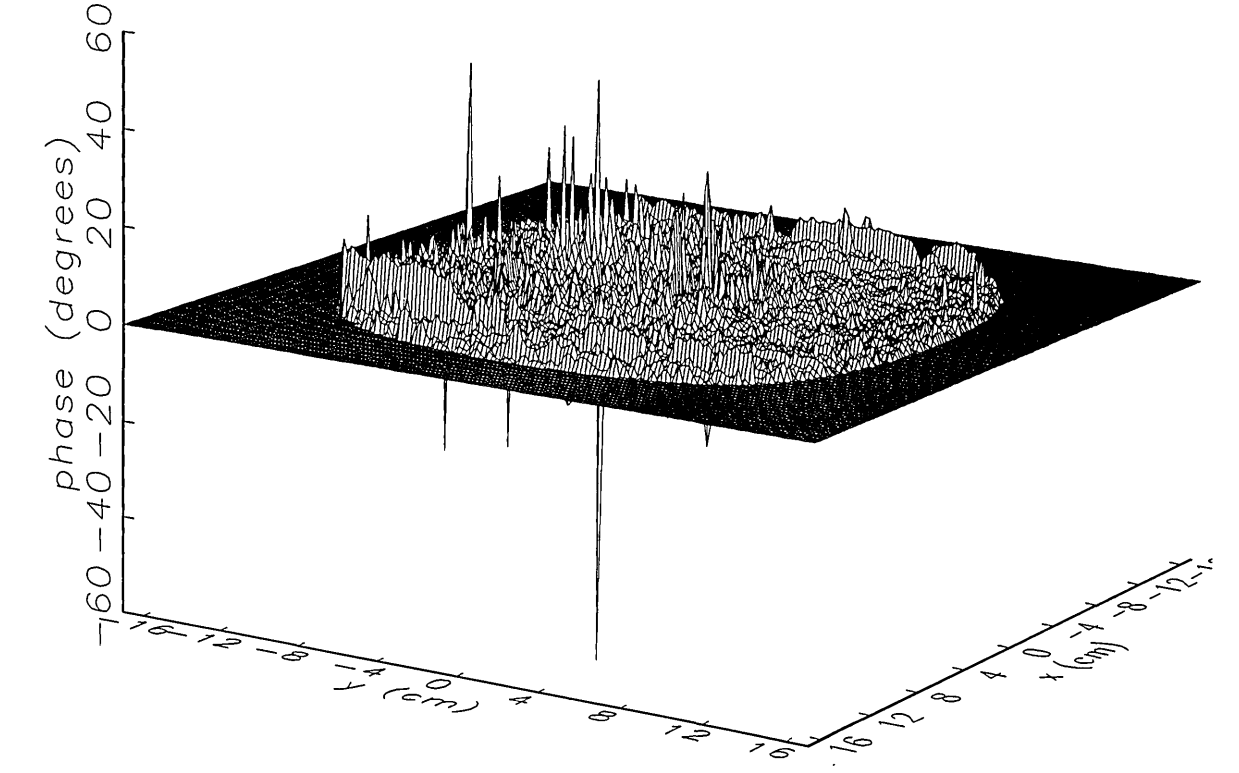

Fig. 16b. The center (main beam) portion of the phase difference between the error-corrected and the error-free near-fields when the *discrete* error function in Fig. 7 is used to construct the error-contaminated near field from measurements.

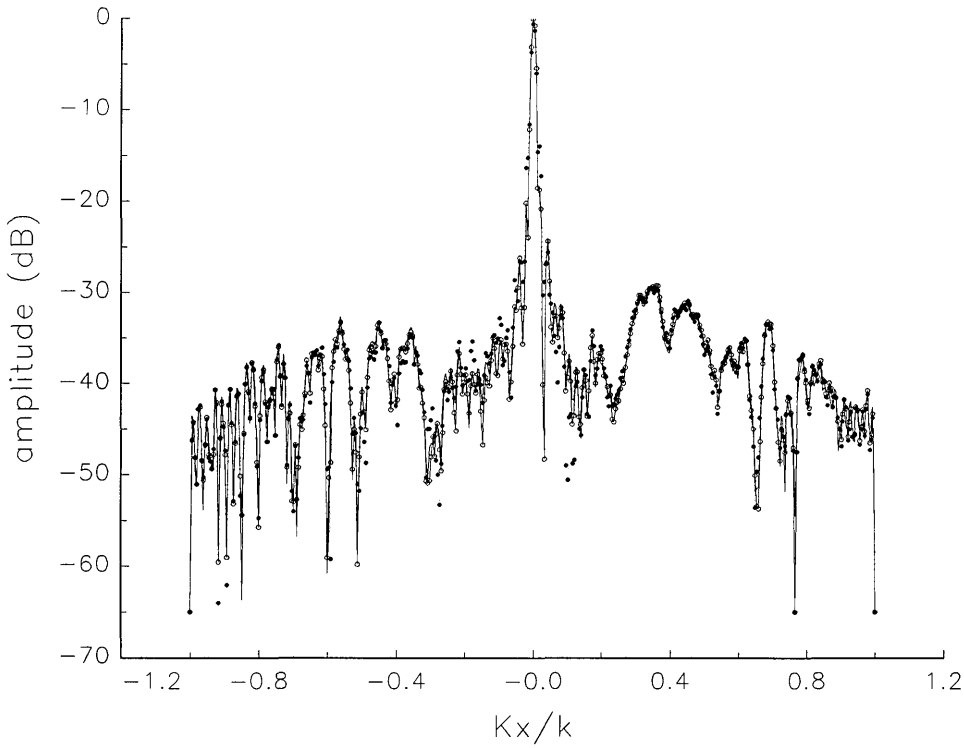

Fig. 17a. The amplitudes of the error-contaminated, error-corrected, and error-free far fields as functions of k_x for the full range of k_x derived from *measured* data. These fields are represented with solid circles connected with dotted lines, open circles connected with solid lines, and a solid line, respectively.

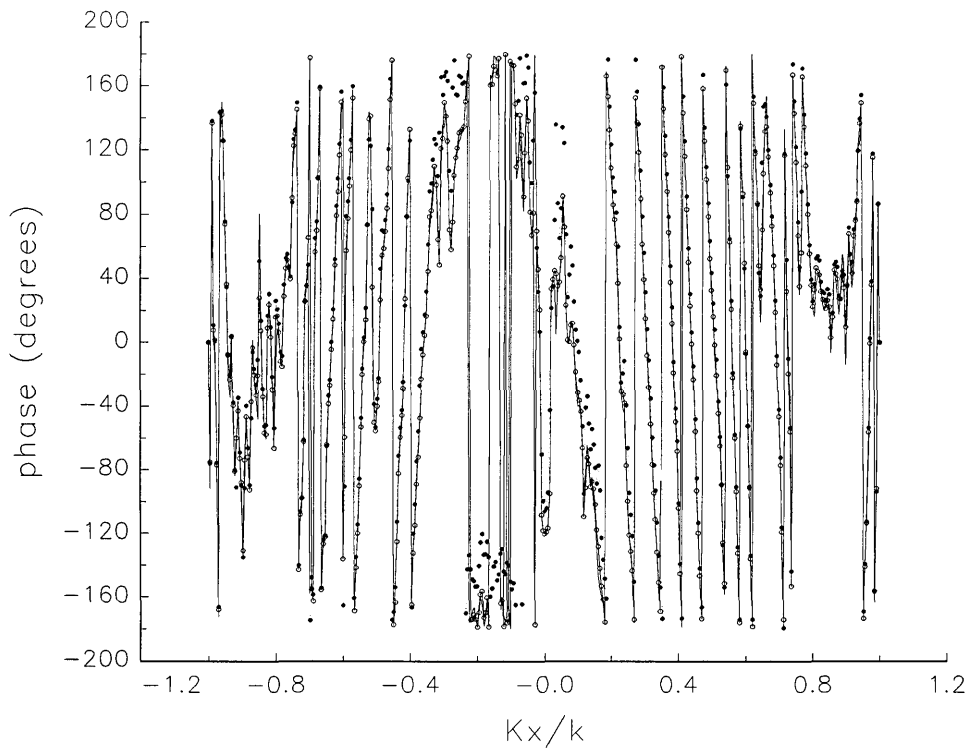

Fig. 17b. The phases of the error-contaminated, error-corrected and error-free far fields as functions of k_x for the full range of k_x derived from measured data. These fields are represented with solid circles connected with dotted lines, open circles connected with solid lines, and a solid line, respectively.

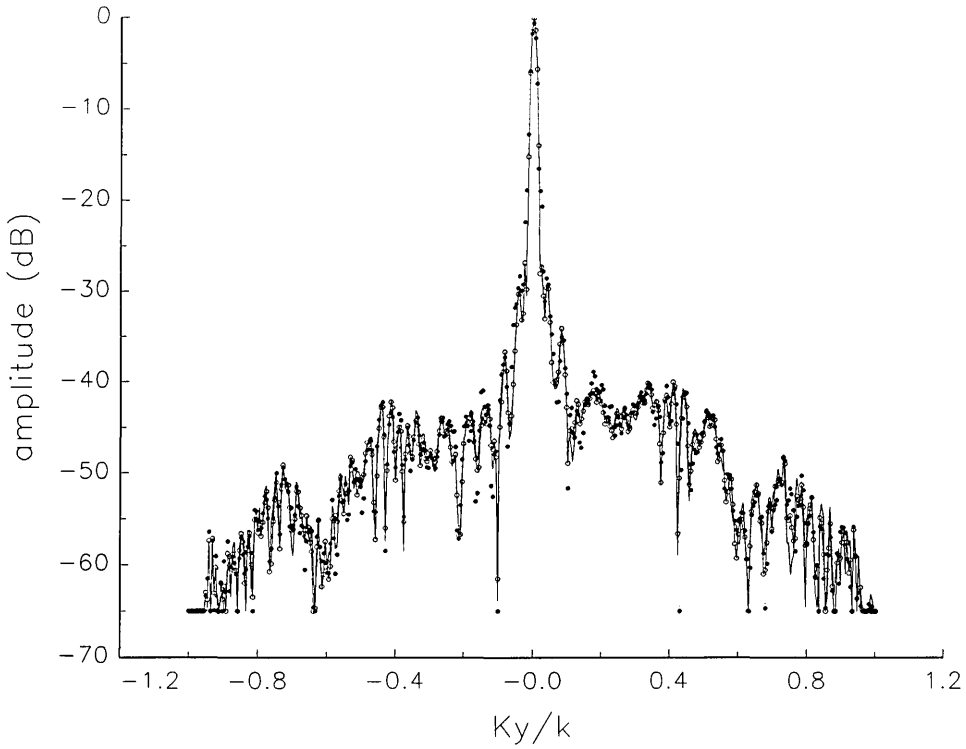

Fig. 17c. The amplitudes of the error-contaminated, error-corrected, and error-free far fields as functions of k_y for the full range of k_y derived from *measured* data (see Fig. 17a).

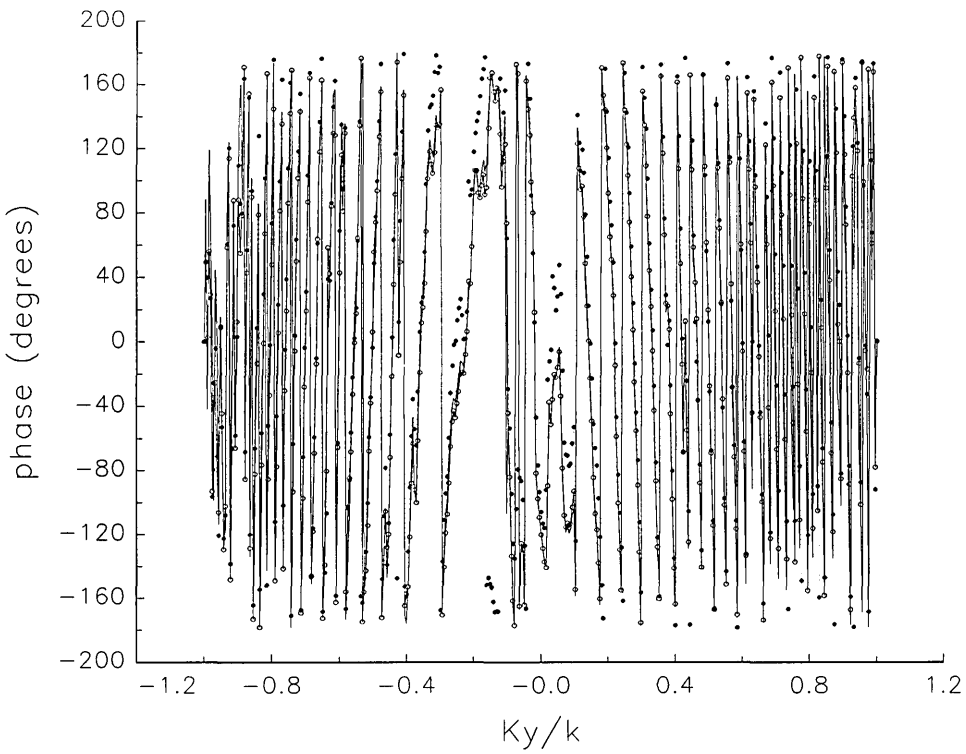

Fig. 17d. The phases of the error-contaminated, error-corrected and error-free far fields as functions of k_y for the full range of k_y derived from *measured* data (see Fig. 17b).

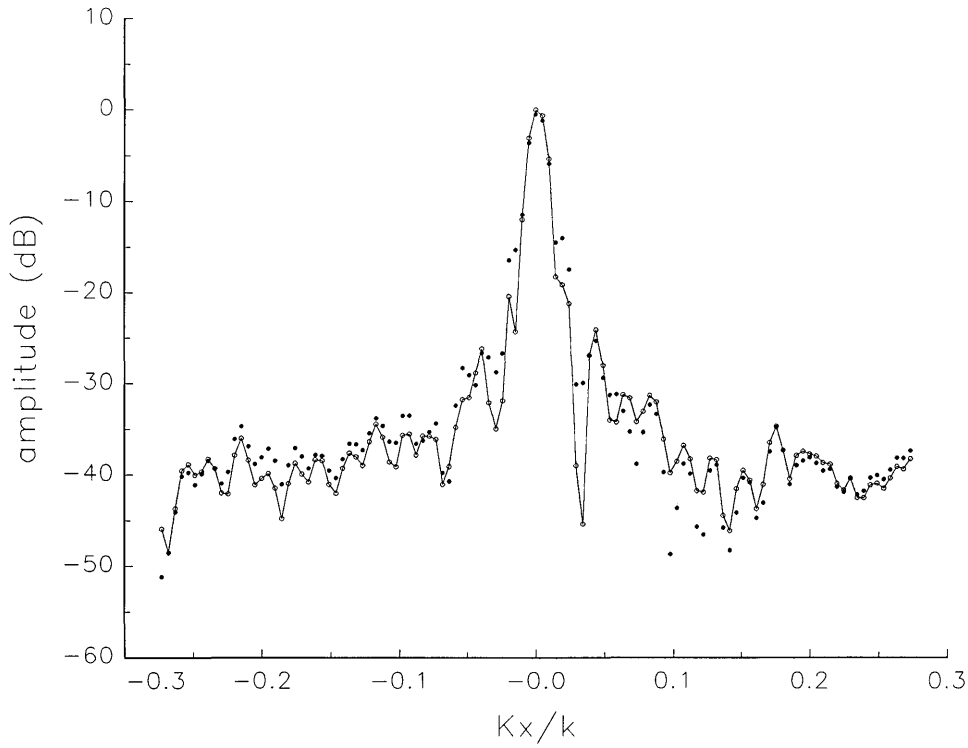

Fig. 18a. The center (main beam) portion of the amplitudes of the error-contaminated, error-corrected, and error-free far fields as functions of k_x derived from *simulated* data. These fields are represented with solid circles connected with dotted lines, open circles connected with solid lines, and a solid line, respectively. The error-corrected and error-free lines overlap, hence, cannot be distinguished.

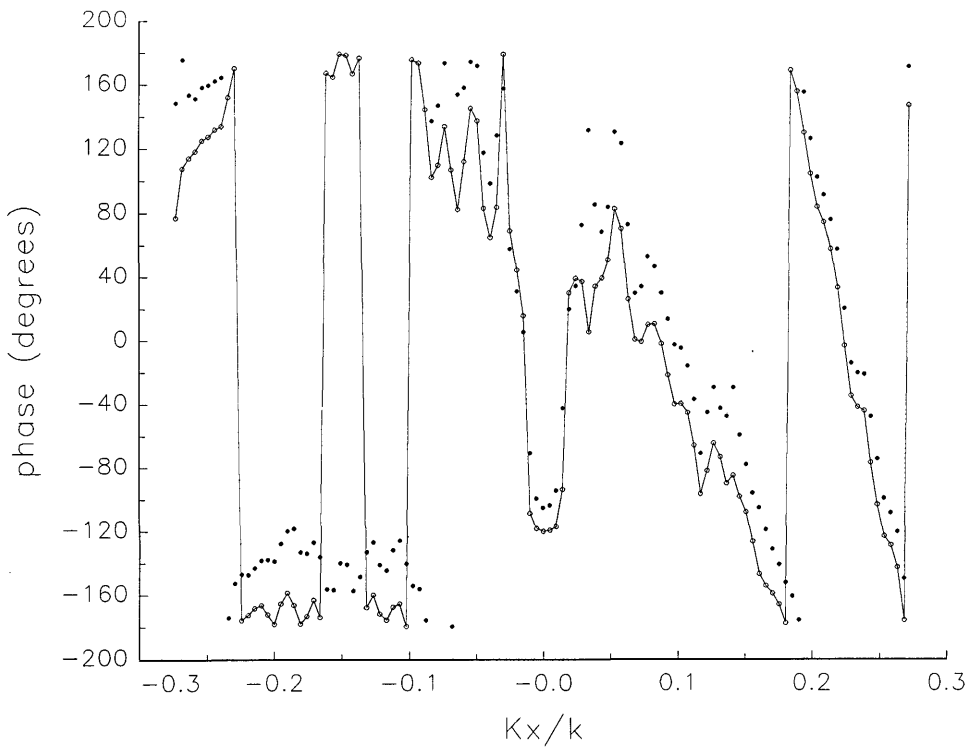

Fig. 18b. The center (main beam) portion of the phases of the error-contaminated, error-corrected, and error-free far fields as functions of k_x derived from simulated data. These fields are represented with solid circles connected with dotted lines, open circles connected with solid lines, and a solid line, respectively. The error-corrected and error-free lines overlap, and, hence, cannot be distinguished.

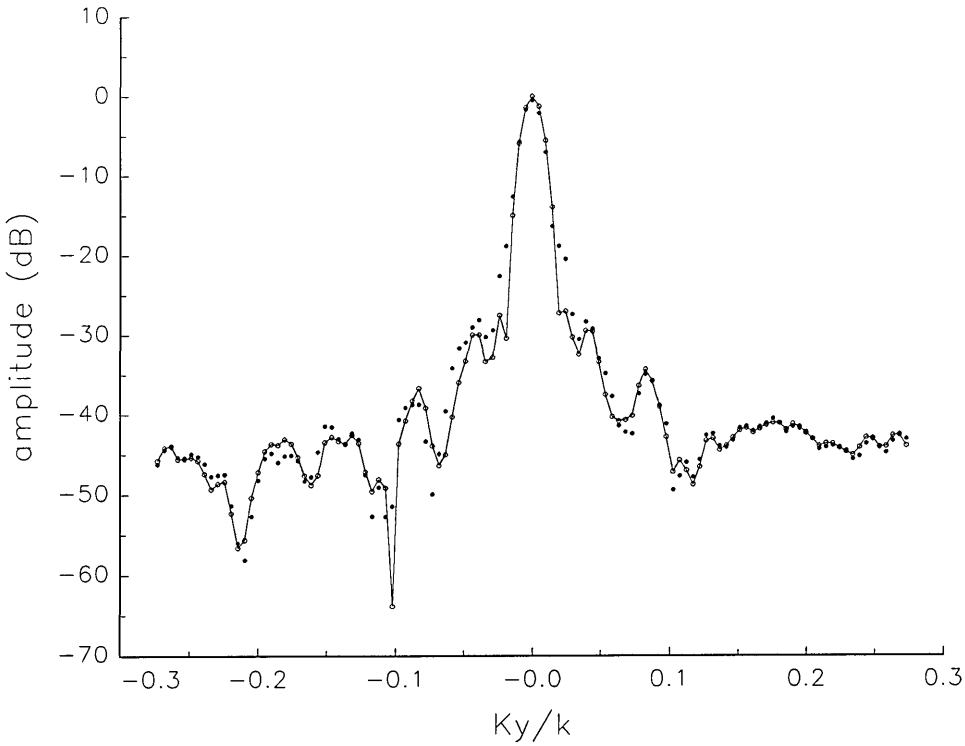

Fig. 18c. The center (main beam) portion of the amplitudes of the error-contaminated, error-corrected, and error-free far fields as functions of k_y derived from *simulated* data (see Fig. 18a).

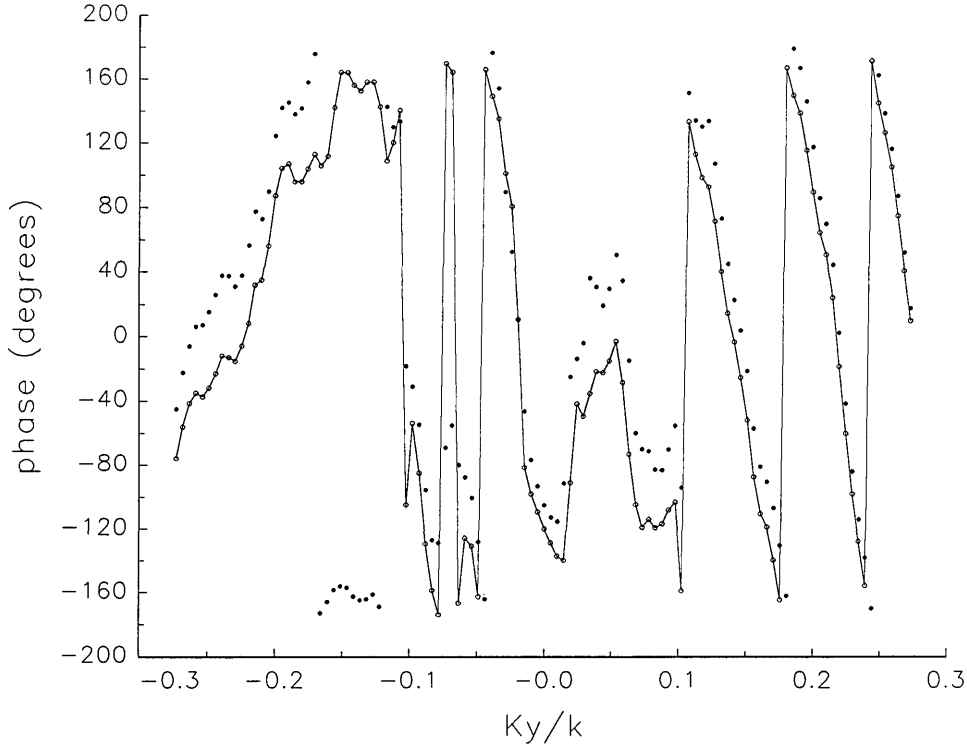

Fig. 18d. The center (main beam) portion of the phases of the error-contaminated, error-corrected, and error-free far fields as functions of k_y derived from *simulated* data (see Fig. 18b).

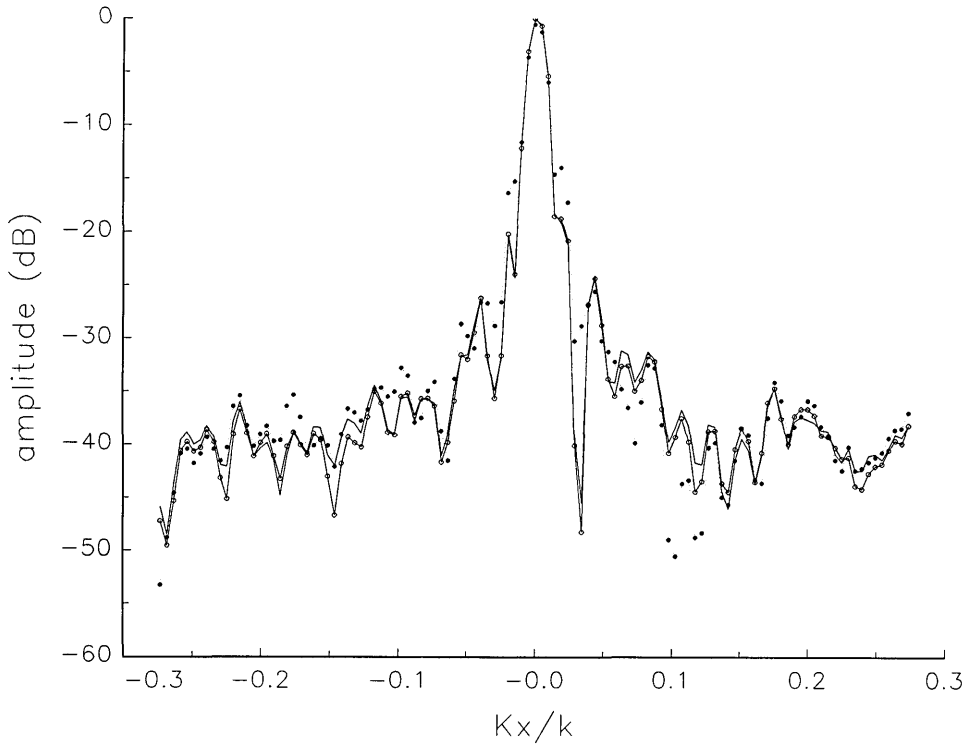

Fig. 19a. The center (main beam) portion of the amplitudes of the error-contaminated, error-corrected, and error-free far fields as functions of k_x derived from *measured* data. These fields are represented with solid circles connected with dotted lines, open circles connected with solid lines, and a solid line, respectively. The error-corrected and error-free lines do not overlap, showing the presence of residual errors.

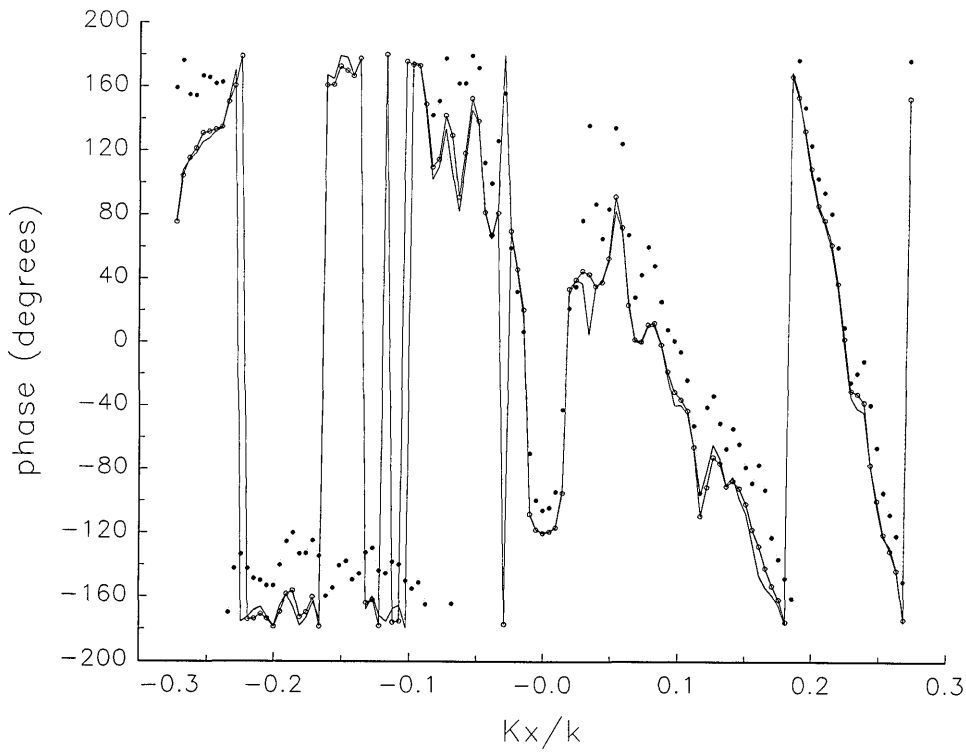

Fig. 19b. The center (main beam) portion of the phases of the error-contaminated, error-corrected, and error-free far fields as functions of k_x derived from *measured* data. These fields are represented with solid circles connected with dotted lines, open circles connected with solid lines, and a solid line, respectively. The error-corrected and error-free lines do not overlap, showing the presence of residual errors.

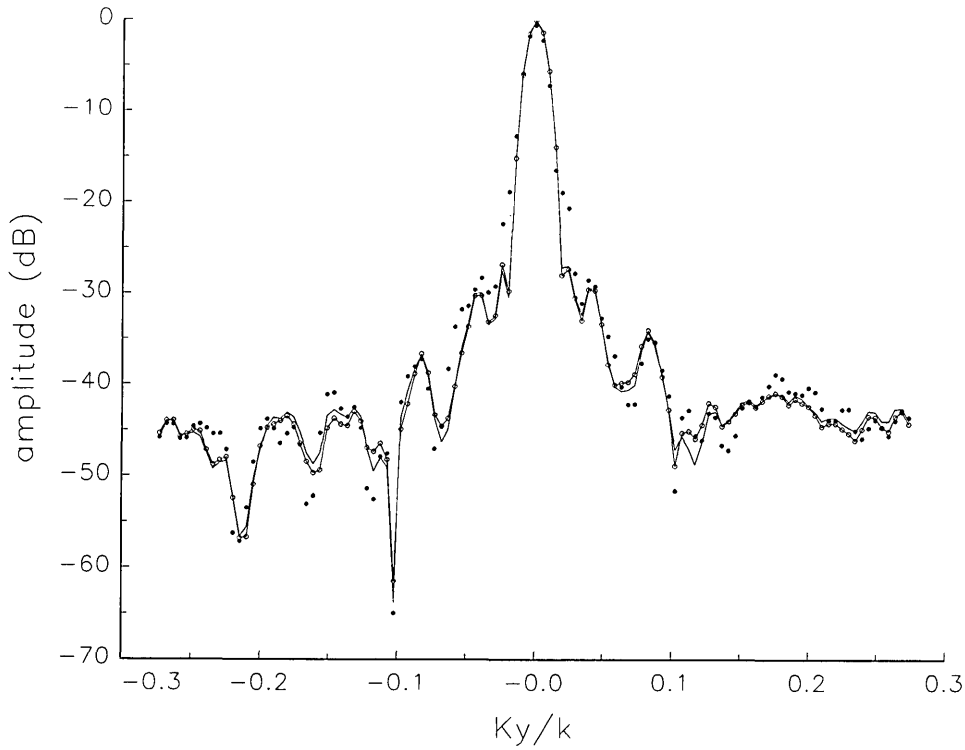

Fig. 19c. The center (main beam) portion of the amplitudes of the error-contaminated, error-corrected, and error-free far fields as functions of k_y derived from *measured* data (see Fig. 19a).

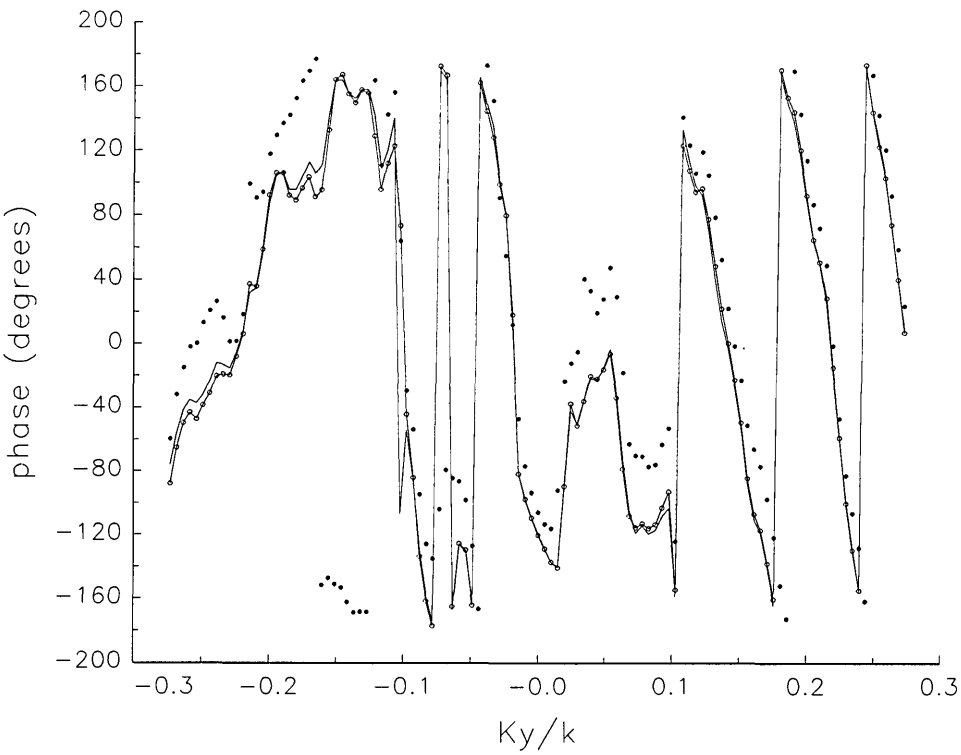

Fig. 19d. The center (main beam) portion of the phases of the error-contaminated, error-corrected, and error-free far fields as functions of k_y derived from *measured* data (see Fig. 19b).

6.2 Residual Drift

In Fig. 2 we have shown the least amount of residual drift observed during a few days of monitoring the system. In the initial stages of analysis *fast* tie-scans are used to analytically remove the drift. But system drift during tie-scans will introduce both amplitude and phase errors that will show up as part of the difference in the smoothness in the discrete surfaces shown in Figs. 12b and 13b. We could remove such residual drifts by isolating the mechanism of interaction between the near-field system and the environment. It is thought, but not proved, that temperature variations are the major cause of such drifts. Hence, the temperature sensitivity of each of the components of the scaner and its instrumentation should be studied, and the most sensitive components should be thermally isolated from the environment.

6.3 Residual Probe-Position Errors

In Fig. 1 we have represented residual probe position errors schematically. In the analysis we have assumed that probe position errors were only due to data selection from the various scan planes $z_0 \ldots z_5$. Each scan plane was treated as perfectly planar. Since the interscan distance δz is much greater than the residual errors in z, the error correction was not effected to first order. We also ignored x and y position errors; accurate data on these errors are not readily available. We can improve the final results of this study by initially correcting for known position errors on a single scan plane (residual errors). This was not done primarily because of practical limitations on time and funds available for the project.

Finally, we note that the error-correction analysis in this study has been carried to *fourth* order, as explicitly prescribed in Eq. (5). By including *fifth*-order terms in the analysis, we could improve convergence to the error-free values.

6.4 Conclusion

In this study we have shown that probe position errors can be removed from real near-field data by the technique developed at NIST, and made suggestions to further improve the quality of near-field measurements at high frequencies by fine tuning both the measurement system and the correction procedure.

7. References

[1] L. A. Muth and R. L. Lewis, IEEE Trans. Ant. Propagat. **38**, 1925 (1990).
[2] L. A. Muth, J. Res. Natl. Inst. Stand. Technol. **96**, 391 (1991).
[3] A. C. Newell, IEEE Trans. Ant. Propagat. **36**, 754 (1988).
[4] L. A. Muth and R. L. Lewis, Natl. Inst. Stand. Technol., Interagency Report, NISTIR 3970 (1991).
[5] A. C Newell, NIST Planar Near-Field Measurements, (1989) to be published.
[6] L. A. Muth, A. C. Newell, R. L. Lewis, S. Canales, and D. Kremer, 12th Annual Meeting and Symposium, AMTA, 13–27 (1990).
[7] L. A. Muth, IEEE Trans. Ant. Propagat. **36**, 581 (1988).

About the author: *Lorant A. Muth is a physicist in the Antenna Metrology Group of the Electromagnetic Fields Division, which is part of NIST Electronics and Electrical Engineering Laboratory. The National Institute of Standards and Technology is an agency of the Technology Administration, U.S. Department of Commerce.*

Volume 97, Number 2, March-April 1992
Journal of Research of the National Institute of Standards and Technology

[J. Res. Natl. Inst. Stand. Technol. 97, 299 (1992)]

Measuring the Electron's Charge and the Fine-Structure Constant by Counting Electrons on a Capacitor

Volume 97 Number 2 March-April 1992

E. R. Williams and Ruby N. Ghosh,

National Institute of Standards and Technology,
Gaithersburg, MD 20899

and

John M. Martinis

National Institute of Standards and Technology,
Boulder, CO 80303

The charge of the electron can be determined by simply placing a known number of electrons on one electrode of a capacitor and measuring the voltage, V_s, across the capacitor. If V_s is measured in terms of the Josephson volt and the capacitor is measured in SI units then the fine-structure constant is the quantity determined. Recent developments involving single electron tunneling, SET, have shown how to count the electrons as well as how to make an electrometer with sufficient sensitivity to measure the charge.

Key words: calculable capacitor; coulomb blockade; electron charge; electron counting; fine-structure constant; single electron tunneling.

Accepted: February 3, 1992

1. Introduction

The recent development of single-electron devices [1,2,3,4,5] has made possible a new and very precise technique to measure the charge of an electron. These devices are based on metal/insulator/metal tunnel junctions whose current-voltage (I-V) characteristics are determined by individual electron tunneling events. If such a device is used to place n electrons on a capacitor of capacitance C_s and the resulting voltage V_s is measured, the electron charge e can be determined in terms of this voltage and capacitance, $ne = V_s C_s$. In practice, V_s is most precisely determined in terms of the voltage generated by a Josephson junction and thus the experiment will not be a determination of e in SI units, but a measurement of e in terms of the Josephson volt [6]. In this paper we show that such a measurement will soon be possible and that an accurate result would make a useful contribution to the field of fundamental physical constants.

1.1 Relating the Fine-Structure Constant and the Electric Charge

First, we address how this measurement relates to the fine-structure constant, α. By relating the measured voltage to a Josephson voltage and the capacitance to SI capacitance as measured in a calculable capacitor experiment [7], we can calculate the fine-structure constant from the following simple equations:

$$V_s = \frac{ne}{C_s} = j f_j \frac{h}{2e} \tag{1}$$

where f_j is the frequency producing the Josephson steps and j is an integer associated with the Josephson effect. (Note that in a Josephson array j is the sum of all the integer steps of each junction.) Solving Eq. (1) for e^2/h, α is given by

$$\alpha = \frac{\mu_0 c e^2}{2h} = \frac{j \mu_0 c f_j C_s}{4n} \tag{2}$$

where μ_0 is the permeability of vacuum and C_s must be measured in SI units. Specifically, the capacitance must be related to the calculable capacitor experiment. In a calculable capacitor experiment a change of capacitance of 0.5 pF can be measured in terms of the meter with an accuracy of 0.014 ppm [7] (1 ppm $= 1 \times 10^{-6}$; throughout, all uncertainties are one standard deviation estimates). This capacitance can then be related with accuracies near the 0.01 ppm level to a 10 pF capacitor that is stable and transportable.

If this experiment to measure e in terms of the Josephson volt and the calculable capacitor can be realized with high accuracy, it will provide a new path to α. This new approach is similar to the measurement of α via the quantum Hall effect [8]. Although both experiments require a connection to the calculable capacitor, this new method is much more direct. The 0.5 pF capacitance change used in most calculable capacitor experiments is a good match to the size of the capacitance that might be used to determine e; only one or two precision ratio transformer bridges need be involved in the calibration of C_s. By contrast, in the quantum Hall case a chain of calibrations might involve these intermediate standards: 0.5 pF, 10 pF, 100 pF, 1000 pF, 100 k Ω, 10 k Ω, 1 k Ω, and 6453.2 Ω. The most accurate value of α determined from the calculable capacitor and quantum Hall effect has an uncertainty of 0.024 ppm [7,9] with 0.014 ppm coming from the calculable capacitor and the rest from the chain of intermediate standards. An alternate determination of α using the proton gyromagnetic ratio in H_2O and the quantum Hall effect but not the calculable capacitor, has an uncertainty of 0.037 ppm [9]. However, these two results differ from each other by (0.10 ± 0.043) ppm. A value of α determined from the anomalous magnetic moment of the electron and quantum electrodynamic theory (QED) has an uncertainty of 0.007 ppm [10] and its value lies between the two non-QED values. Therefore, the unexplained 0.10 ppm difference in the non-QED values limits the accuracy to which QED theory is tested. Any measurement of α by this new SET method at the 0.1 ppm level or better would be helpful in the field of fundamental constants [8].

1.2 SET Devices

K. K. Likharev and his colleagues [1] have long been proponents of the application of Coulomb blockade effects arising from the discreet charge of electrons to realize a precise current source. Their pioneering ideas and experiments paved the way for much of the recent progress. In the past few years, new devices employing metal/insulator/metal tunnel junctions have been demonstrated which could allow a precise measurement of the electron charge e and thus α. These include an electrometer [2], observation of single electron tunneling oscillations [3], a "turnstile" current source [4], and a "pump" current source [5]. A brief sketch of single-electron tunneling is presented to describe the operation of the electrometer and pump.

Consider a normal-metal tunnel junction biased by a current source and having a capacitance C. The change in energy of the junction after an electron tunnels through the barrier is $\Delta E = eQ/C - e^2/2C$, where Q is the charge across the junction and $e^2/2C$ is the Coulomb energy cost of the tunneling event. If the tunneling resistance of the junction is greater than the quantum unit of resistance, $R_t \gg h/e^2$, and thermal fluctuations do not mask the charging energy, $kT \ll e^2/2C$, then a Coulomb blockade appears in the junction I-V characteristic where the tunneling probability is greatly reduced for $|V| < e/2C$. At 50 mK, and using 1 fF for the junction capacitance, one finds $(kT)/(e^2/2C) \sim 1/20$, hence temperature effects are small but non-negligible. The single-electron devices exploit this Coulomb blockade of the tunneling current.

The Fulton-Dolan (SET) electrometer [2] is shown schematically in Fig. 1a. Aside from tunneling events, the electrode a between the two junctions and the gate capacitor C_0 is an "island" electrically isolated from the circuit. The electrometer provides a very high impedance technique to measure the potential U. At a constant bias V, the device conductance as a function of gate voltage is periodic with the period $\Delta U = e/C_0$. The bias voltages V and U are chosen to maximize the sensitivity of the electrometer so that the device current is linearly proportional to small changes of the potential U. Such electrometers have demonstrated

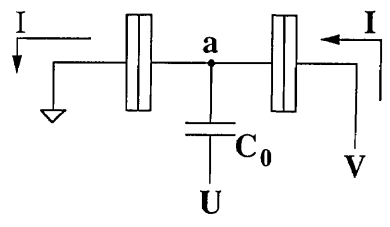

Fig. 1a. *This circuit shows an electrometer formed by two tunnel junctions each having a capacitance C. The input is potential U coupled to the isolated island a through C_0.*

charge sensitivity of 1.5×10^{-4} $e/\mathrm{Hz}^{1/2}$ at a frequency between 2 and 200 Hz [11].

Convincing experimental evidence of the SET oscillations producing the controlled transfer of electrons with the relation $I=ef$ was reported by Delsing et al. [3]. Geerligs et al. [4] were the first to demonstrate flat plateaus and observe a current with accuracies of better than 1% using the turnstile device. However, certain properties of the pump device suggest that it will be more precise in counting electrons and we therefore sketch its operation.

An electron pump [5] (see Fig. 1b) is a device similar to the electrometer, in which a single electron tunnels sequentially through the "islands" labeled **b** and **c**. For a given voltage V, a controlled number of electrons can be transferred in either direction by appropriately cycling the gate voltages U_1 and U_2 at the frequency f. The pump also delivers an electron current at the rate $I=ef$. The direction of the current can be reversed simply by reversing the phase of U_1 and U_2. A pump based on four or five tunnel junctions operating at 1–10 MHz has been theoretically predicated to be able to deliver a known current with errors below the 1 ppm level [12,13].

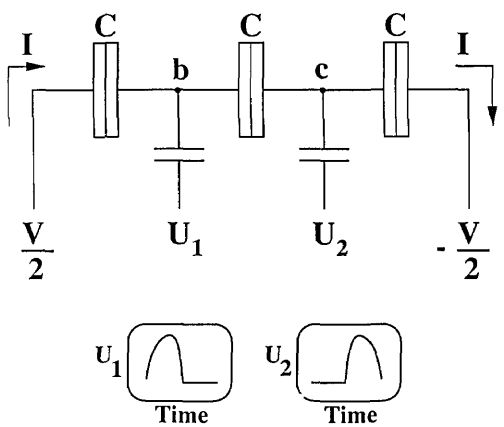

Fig. 1b. This circuit shows a three junction pump that pumps one electron per cycle of the wave-forms shown. The electron is first pumped to island **b** by potential U_1 then to **c** by U_2.

The currents produced by these pumps are only about 10^{-12} A and thus precision measurements will be a challenge. Direct measurement by sensing the voltage across a high resistance is a problem because it is difficult for metrologists to accurately calibrate the required high resistances. Capacitors, on the other hand, have already been accurately calibrated in a range that will be useful in the following experiment.

2. Experimental Configurations [14]

2.1 Measurements of the Electric Charge *e*

Figure 2a shows one possible configuration that incorporates these new SET devices to measure the electronic charge. A standard capacitor C_s is connected to a current source (pump) and also to the input of a Fulton-Dolan electrometer via a coupling capacitor C_c, forming an isolated island **a**. Using the electrometer as a null detector a voltage V_s is applied across C_s to maintain the island **a** at a fixed potential (near ground), while pumping electrons onto or off of the island. The stray capacitance to ground, C_g, limits the sensitivity of the electrometer to V_s. The voltage, V_s, on the capacitor is adjusted so that the electrometer input is always at the same potential (near ground). Thus the current from the

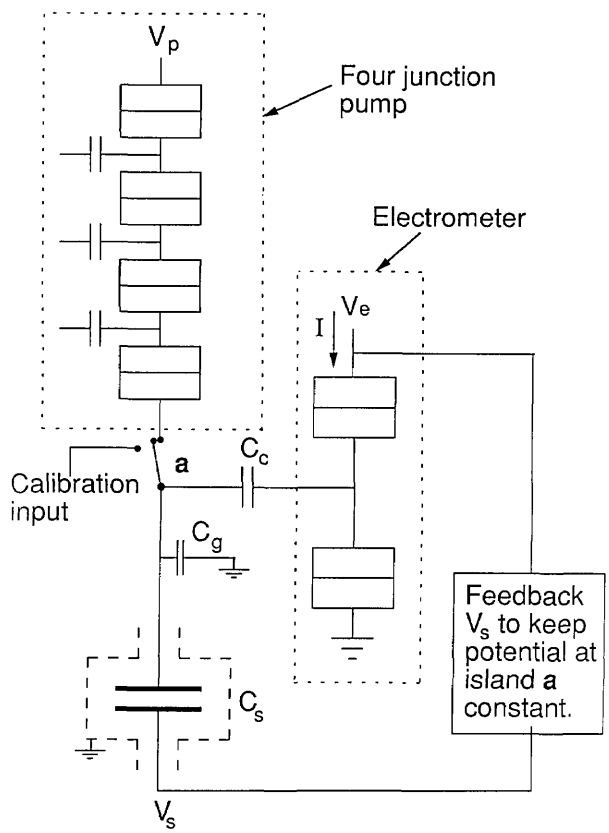

Fig. 2a. Proposed circuit for measuring α. The voltage V_s required to keep the potential of the island **a** constant when n electrons are pumped onto the island can be used to measure the electron charge in terms of C_s and V_s. The electrometer monitors the potential at **a**.

pump serves as the charging current of the capacitor as the voltage is ramped up. A specific example is illustrated in Fig. 2b. With the pump operating at 6.2 MHz for 10 s, the voltage across a 1 pF capacitor standard will charge to 10 V at a linear rate in order to keep the electrometer input constant. We stop the pump and measure the 10 V signal as well as any deviation of the electrometer from null. Reversing the pump for 20 s then brings the voltage to −10 V.

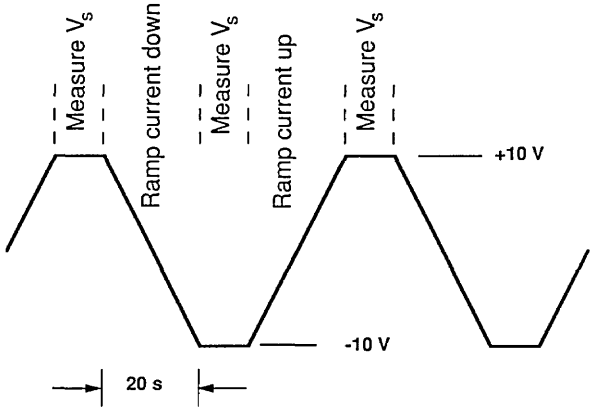

Fig. 2b. The measurement sequence for measuring α, showing the potential V_s as a function of time.

In order to use a capacitor as a standard it must have a well defined capacitance; it thus is necessary to understand how precision capacitors are measured and under what circumstances they are well defined. Figure 3 shows the essential features of one side of a standard bridge that is used to compare capacitors C_1 and C_2. The dashed lines represent the grounded shield that prevents the potentials V_1 and V_2 from affecting the detector except through their respective capacitances. This shielding is critical to making precise capacitance comparisons. The bridge is balanced by adjusting the potentials $V_1/V_2 = C_2/C_1$. C_{g1} and C_{g2} represent the stray capacitance to ground. The bridge balance is not affected by C_{g1} because there is no voltage across C_{g1} when the bridge is balanced. However, C_{g1} does affect the detector sensitivity so it should be kept small. The capacitance C_{g2} does not affect the balance as long as the impedance from the source to C_1 is small compared to the impedance of C_{g2}. Present day precision 10 pF capacitance standards with $C_{g1} = 200$ pF are compared at the 0.01 ppm level at a frequency $\omega = 10^4$ s^{-1} (1592 Hz) using a room temperature detector with a noise figure of 20 $e/\text{Hz}^{1/2}$. A SET electrometer should have similar noise performance at the same frequency and capacitance. Further improvements in the sensitivity of the SET electrometer are expected when measuring smaller capacitances.

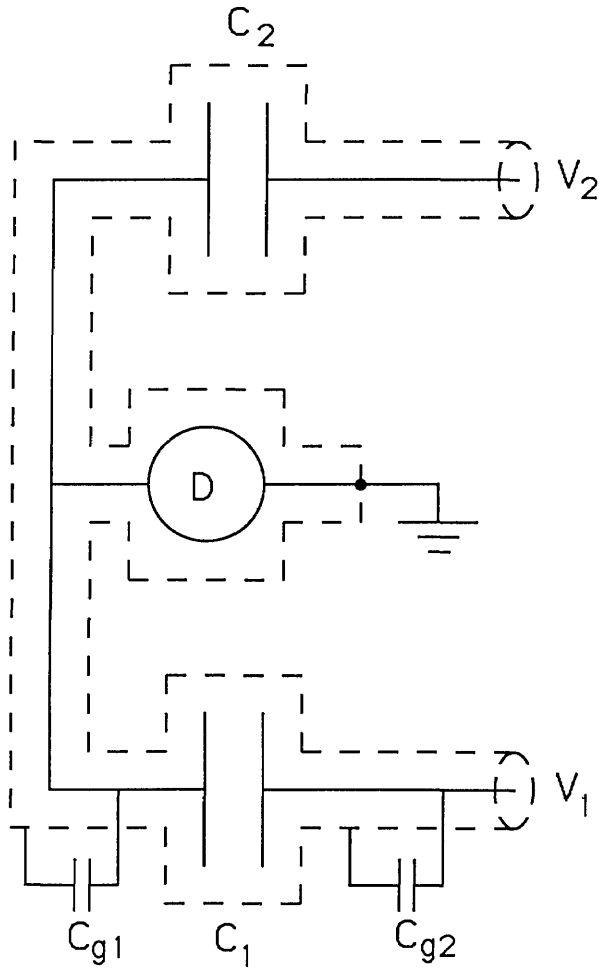

Fig. 3. Circuit showing half of a bridge used to compare capacitors C_1 and C_2. The potentials V_1 and V_2 are usually supplied by a precision transformer. The effect of stray capacitances C_{g1} and C_{g2} are discussed in the text.

The key to this experiment to measure e using a capacitor is to replace the detector in Fig. 3 with a Fulton-Dolan electrometer as shown in Fig. 2a. By placing the electrometer at 20 mK near the source of charge, we anticipate fewer problems from leakage and less stray capacitance to ground. In addition, we expect to gain from the impressive sensitivity of this device, reduce the leakage dramatically, and still make a well defined capacitor that can be calibrated *in situ.*

Because of the requirement to shield the standard capacitor, it is easier initially to have this capacitor on a different chip from the electrometer and pump. As multilayer technology becomes incorporated into the junction fabrication process this capacitor could be placed on the same chip. Having it on a separate chip leads to some practical limits in the optimum choice for C_s. The sensitivity of the electrometer is approximately given by $C_c/(C_s+C_g)$, where C_g represents all other capacitances to ground. This two chip arrangement will increase C_g, but we expect to keep it near 1 pF. Choosing C_s to be small both increases V_s and maximizes the electrometer sensitivity. A 1 pF capacitance for C_s constitutes a practical compromise.

Calibration of the capacitance requires making a connection to room temperature. However, the Fulton-Dolan electrometer could still be used by means of the calibration input switch shown in Fig. 2. Note that care must be taken to keep the capacitance from the island to ground low.

2.2 Dual Pump Bridge

Another interesting experiment (see Fig. 4) is to have two current sources (drawn as two, four-junction "pumps" in Fig. 4) feeding into an island **a** with a total capacitance of about 10 fF. The charge state of island **a** is then measured with an electrometer. This geometry will not measure e but will allow the very precise comparison of two current sources. Any difference in current from the two sources will show up as an accumulation of the island charge. The island capacitance is chosen to be large enough to greatly reduce the interaction of the two pumps but small enough to still have single charge resolution. Because the error is detected as an integrated charge on the island, only a short time is required to obtain extremely high precision. It would also be interesting to compare the error rate of a "pump" and a "turnstile."

3. Future Prospects

A new precision technique to measure the fine-structure constant via Eqs. (1) and (2) has been described. At present SET experiments have been used to determine currents only at the 0.1 to 1.0% level, hence it is risky to predict the ultimate accuracy of the technique. Based on theoretical predictions [12,13] we expect that the number of electrons could be measured with 1 ppm accuracy in a four junction pump. A five junction pump

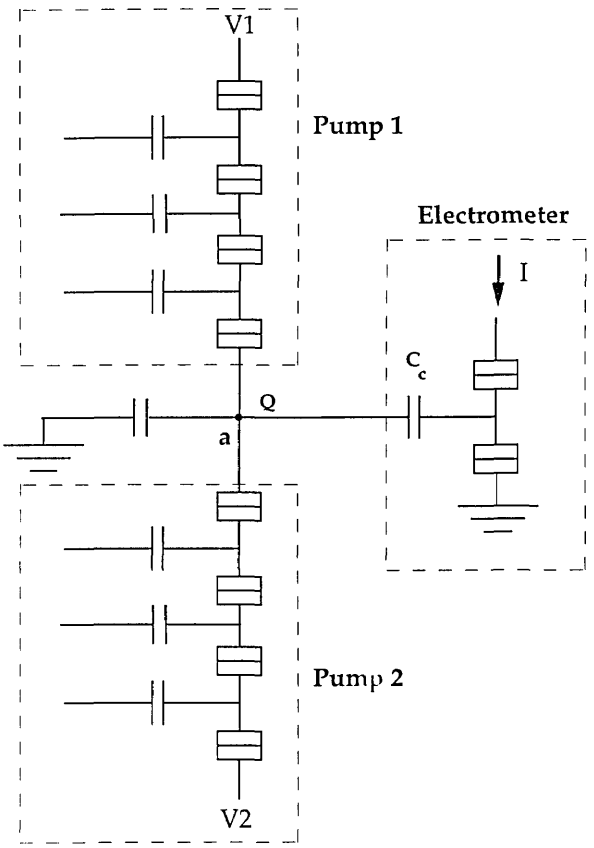

Fig. 4. A bridge circuit used to compare two pump circuits. The electrometer detects any accumulation of charge on island **a**.

should be more accurate still. At present the electrical standards needed to support this measurement do not appear to limit its accuracy. For example, capacitance standards of 10 pF are compared between national laboratories near the 0.02 ppm level and 10 V Zener voltage references are also compared with 0.02 ppm accuracy. In the first experiments these accuracies will likely not be reached, but much physics will be learned about SET devices as we make another accurate determination of α.

Acknowledgment

We thank M. H. Devoret, D. Esteve, C. Urbina, H. Pothier, and P. Lafarge of Service de Physique du Solide et de Resonance Magnetique, Centre d'Etudes Nucleaires des Saclay, for many informative discussions about SET devices. We thank J. Q. Shields for crucial discussions about the techniques used to measure standard capacitors. Discussions with B. N. Taylor, Hans Jensen, and R. L. Kautz were also very useful.

4. References

[1] D. V. Averin and K. K. Likharev, in Mesoscopic Phenomena in Solids, B. Al'tshuler, P. A. Lee, and R. A. Webb, eds., Elsevier, Amsterdam (1991) Chapter 6.

[2] T. A. Fulton and G. J. Dolan, Observation of Single-Electron Charging Effects in Small Tunnel Junctions, Phys. Rev. Lett. **59**, 109–112 (1987).

[3] P. Delsing, K. K. Likharev, L. S. Kuzmin, and T. Claeson, Time-Correlated Single-Electron Tunneling in One-Dimensional Arrays of Ultrasmall Tunnel Junctions, Phys. Rev. Lett. **63**, 1861–1864 (1989) and Phys. Rev. B **42**, 7439–7449 (1990).

[4] L. J. Geerligs, V. F. Anderegg, P. A. M. Holweg, J. E. Mooji, H. Pothier, D. Esteve, C. Urbina, and M. H. Devoret, Frequency-Locked Turnstile Device for Single Electrons, Phys.Rev. Lett. **64**, 2691–2694 (1990).

[5] H. Pothier, P. Lafarge, C. Urbina, D. Esteve, and M. H. Devoret, Single-Electron Pump Based on Charging Effects, Europhys. Lett. **17**, 249–254 (1992).

[6] Resolution 6 of the 18th Confèrence Gènèrale des Poids et Mesures. See B. N. Taylor, ed., The International System of Units (SI), Natl. Inst. Stand. Technol. Spec. Pub. **330** (1991) p. 45.

[7] J. Q. Shields, R. F. Dziuba, H. P. Layer, New Realization of the Ohm and Farad Using the NBS Calculable Capacitor, IEEE Trans. Instrum. Meas. **38**, 249–251 (1989).

[8] B. N. Taylor and E. R. Cohen, How accurate are the Josephson and Quantum Hall Effects and QED?, Phys. Lett. A **153**, 308 (1991).

[9] M. E. Cage, R. F. Dziuba, R. E. Elmquist, B. F. Field, G. R. Jones, Jr., P. T. Olsen, W. D. Phillips, J. Q. Shields, R. L. Steiner, B. N. Taylor, and E. R. Williams, NBS Determination of the Fine-Structure Constant and the Quantized Hall Resistance and Josephson Frequency-to-Voltage Quotient in SI Units, IEEE Trans. Instrum. Meas. **38**, 284–289 (1989).

[10] T. Kinoshita and W. B. Lindquist, Eighth-order Magnetic Moment of the Electron. V. Diagrams Containing No Vacuum-Polarization Loop, Phys. Rev. D **42**, 636–655 (1990).

[11] L. J. Geerligs, V. F. Anderegg, and J. E. Mooij, Tunneling Time and Offset Charging in Small Tunnel Junctions, Physica **B165/166**, 973–974 (1990).

[12] H. Pothier, 1991, Blocage de Coulomb et Transfert d'Electons Un Par Un, PhD Thesis, de l'Universite Paris 6.

[13] Hans Jansen and J. Martinis, private communications.

[14] The configurations shown here were first presented by the authors as a poster paper at the NATO Advanced Study Institute on Single Charge Tunneling, Les Houches, France, March 1991. J. Martinis will present a paper on this subject at the Conference on Precision Electromagnetic Measurements, June 1992, in Paris France.

About the authors: *Edwin R. Williams is a physicist in the Electricity Division at NIST. Ruby N. Ghosh is an American Society of Engineering Education Postdoctoral Fellow in the Electricity Division at NIST. John M. Martinis is a physicist in the Electromagnetic Technology Division at NIST. The National Institute of Standards and Technology is an agency of the Technology Administration, U.S. Department of Commerce.*

Volume 97, Number 2, March–April 1992
Journal of Research of the National Institute of Standards and Technology

News Briefs

General Developments

Inquiries about News Briefs, where no contact person is identified, should be referred to the Managing Editor, Journal of Research, National Institute of Standards and Technology, Administration Building, A635, Gaithersburg, MD 20899; telephone: 301/975-3572.

BIOASSAY REFERENCE VALUES ESTABLISHED FOR THREE NIST SRMs

Short-term bioassays are being used in many countries to evaluate the exposure of humans to complex mixtures of mutagens and potential carcinogens in air, water, soil and from various emission sources. The salmonella mutagenicity assay developed by Professor Bruce Ames and coworkers in 1925 is the mutagenesis bioassay most frequently used in such studies.

In 1987, the International Programme on Chemical Safety, in collaboration with the Environmental Protection Agency and NIST, initiated an international collaborative study to determine the variability of data being generated by labs using the Ames Bioassay. The study involved 20 laboratories from North America, Europe, and Japan that used the Ames test on a regular basis. Three NIST SRMs that are certified for chemical composition were used in the study: 1597, Complex Mixture of Polycyclic Aromatic Hydrocarbons from Coal Tar; 1649, Urban Particulate Matter; and 1650, Diesel Exhaust Particulate Matter.

The results from this study revealed an interlaboratory variability (approaching 100 percent coefficient of variation) among the twenty study participants. Representatives from these expert laboratories agreed that the variation found represented the current state-of-the-art practice for these assays. While a true value exists for chemical and physical properties that can be measured with a relatively high degree of accuracy and precision, bioassays are inherently more variable in part because the living organisms that serve as detection devices are constantly undergoing dynamic processes of growth, replication, metabolism, and interaction.

The data from the collaborative study has been used to establish two types of reference values. One, expressed as a 95 percent confidence interval, defines the actual mutagenic activity as measured by the Ames bioassay test. The other, expressed as an 80 percent tolerance interval, characterizes the differences in reported mutagenic activity and establishes a realistic target for comparing individual laboratory results with the state-of-the-practice. With these Ames Mutagenicity reference values, SRMs 1597, 1649, and 1650 can now be used by the international bioassay measurement community as powerful tools for reducing the variability of Ames bioassay data.

ANALYTICAL METHOD DEVELOPED TO INVESTIGATE THE ROLE OF VITAMIN C IN CANCER PREVENTION AND JUVENILE ARTHRITIS

The role of selected vitamins in the prevention of certain diseases, such as cancer, has been the subject of great interest in recent years. Scientists at NIST and the National Cancer Institute recently developed a method for the accurate and precise measurement of vitamin C in human plasma. Procedures also were developed for stabilizing calibration standards and for preparing stable and homogeneous quality control materials (70 °C). The results of studies conducted to assess the long-term stability of vitamin C in preserved frozen plasma and the short-term stability in whole blood (4 °C) indicated that plasma samples containing vitamin C can be stored for at least 1 yr without measurable analyte degradation. In addition, vitamin C remains intact for at least 6 h in whole blood. These studies also were used to assess the

performance of laboratories participating in NCI studies designed to examine the role of vitamin C in carcinogenesis.

This accurate method for the measurement of vitamin C has proven to be useful in a collaborative study with the Children's Hospital National Medical Center and George Washington University, where the vitamin C content of the serum of patients with juvenile arthritis was measured. The results indicate that the serum vitamin C levels correlate well with the pathological types of arthritis exhibited by the patients.

Each of these studies, the multilaboratory study on relationship of vitamin C to cancer incidence and the grouping of pathological states as a function of serum vitamin C levels, requires the use of accurate and precise trace organic measurement technology.

INTRAMOLECULAR VIBRATIONAL ENERGY REDISTRIBUTION STUDIED BY PICOSECOND IR SPECTROSCOPY

Measuring molecular vibrational energy redistribution rates and extracting transfer mechanisms are key steps toward understanding energy involvement in all chemical transformations. Obtaining this dynamical information is especially difficult for polyatomic molecules in high temperature condensed media since such processes occur on the picosecond and femtosecond timescales. NIST scientists have been able to examine these events in real time by developing novel ultrashort pulsed infrared techniques which monitor transient energy population in specific vibrational modes. Careful selection of the molecular species and surrounding environment has enabled them to directly probe fundamental transfer events after energy has been selectively deposited in a vibrational mode. The scientists have recently measured for the first time vibrational energy transfer rates for a metacarbonyl-nitrosyl molecule, $Co(CO)_3NO$, in the gas phase and as dissolved in $CFCl_3$ solution. The rates increased by factors of two to five for the molecule in solution and the measurements indicate that populated lower energy states readily relax by depositing energy into solvent motions. These energy transfer mechanisms are now being studied by selecting buffer gases with specific acceptor vibrational energies (e.g., CO, NO, $CFCl_3$) and measuring vibrational energy transfer processes as a function of pressure and density.

FREQUENCY AND WAVELENGTH STANDARD FOR THE FAR INFRARED

Visiting scientists at NIST recently completed a high-resolution study of the far-infrared spectrum of gaseous carbon monoxide (CO). The frequencies of pure rotational transitions in the ground state of the molecule were measured using their laser-synthesized, tunable far infrared spectrometer. A complete set of frequencies was calculated from these data with an accuracy of about 5 parts in 10^9. This is 10 times more accurate than the previous best measurements.

Accurate measurements of the spectrum of carbon monoxide are important for two reasons. First, CO is an abundant interstellar molecule, and many astrophysical measurements and tests of theory depend on the accuracy of CO rotational frequencies. Second, CO is often used as a reference standard to calibrate spectrometers (especially Fourier transform spectrometers) in the far infrared. With the completion of this work, the CO transitions are now the most accurate far-infrared frequencies available in the frequency range from 100 to 4300 GHz (wavelength of 300 to 7 μm).

IN SITU CHARACTERIZATION OF THE PULSED LASER DEPOSITION OF THIN FILMS

Pulsed laser deposition (PLD) has been shown to be an effective means of depositing thin films from refractory targets. Excimer and Nd/YAG lasers are being used by NIST to deposit thin films of high T_c superconductors, high dielectric constant $BaTiO_3$, ferroelectric $PbZr_{.53}Ti_{.47}O_3$ (PZT), and magnetic thin films of Fe_3O_4 and Ag-Fe_3O_4. During the PLD of these thin films, optical emission spectroscopy is used to determine the identity and energy (temperature) of the excited state species present in the laser induced plumes. These results, combined with the results of in situ molecular beam mass spectrometric analysis of the plumes, permits determination of both the minor and major species present during the PLD process, including nonexcited neutral species and complex molecular species. Correlations are being made with the film's stoichiometry, morphology and electric or magnetic properties.

NEW COMPUTATIONAL METHOD FOR PATTERN FORMATION DURING ALLOY SOLIDIFICATION

A new model has been developed that predicts the growth and resulting segregation patterns of solid

particles forming from a melt during alloy solidification. These segregation patterns are responsible for defects that limit the mechanical and corrosion properties of many alloys. This new approach was previously developed for pure materials but, through work at NIST has now been applied to the more useful case of binary alloys. The system is treated in its entirety with a continuous field variable describing the state (liquid or solid) of the various regions of the system. Classical methods previously used to calculate these growth morphologies have required numerical tracking of the free boundary that separates the liquid from the solid and individual treatment of each phase. By contrast, the present approach greatly simplifies the calculations, making predictions for practical alloys feasible.

FIBER LASER OFFERS WAVELENGTH STANDARD

NIST has successfully stabilized the wavelength of an erbium-doped fiber laser to a narrow atomic absorption line in the 1.5 μm region, offering industry a highly accurate optical wavelength standard. The work is critical to the development of advanced optical communication systems utilizing cables smaller in size and cheaper to operate than conventional wire lines. Narrow wavelength operation permits many optical channels to be packed into a single fiber. To create a system like this, an adequate laser wavelength standard is necessary. NIST's proposed standard uses both a diode laser operating near 0.78 μm and a fiber laser near 1.53 μm to drive transitions in rubidium. Additionally, the fiber laser already has been used successfully in high-resolution spectroscopy, aiding researchers in their investigations of atomic and molecular behavior. For technical information, contact Sarah Gilbert, Div. 814.02, NIST, Boulder, CO 80303, 303/497-3120.

NIST RESEARCH LEADS TO SIGNIFICANT YIELD IMPROVEMENT IN THE MANUFACTURE OF MEMORY CHIPS

Research by a NIST scientist has directly contributed to a significant improvement in yield in the manufacture of integrated circuit memory chips in SIMOX material. SIMOX material is made by implanting oxygen in silicon wafers to form a silicon dioxide layer beneath the silicon surface. Because of the smaller volume in which hole-electron pairs can be generated, electronic circuits fabricated in SIMOX material are much more resistant to radiation effects than bulk silicon.

If there are particles on the wafer surface during implanting, conducting channels or pipes form between the silicon layer on the top and the substrate. Devices made on such a SIMOX wafer do not work properly. The scientist developed a potassium hydroxide etching procedure which made the pipes visible using optical microscopy. Further investigation showed that the number of surface particles could be reduced from $10/cm^2$ to $0.1/cm^2$ by taking certain steps to reduce contamination within the implanter. Two private companies adopted these procedures for producing SIMOX material. One company used its material to manufacture SIMOX-based static random-access memories (SRAMs) and reports a significantly increased yield in 64 kilobit SRAMs. The company also reports that use of the new SIMOX material made manufacture of a 1 megabit SRAM possible.

NIST LEADS INDUSTRY TO ACCORD IN X-RAY MASK SPECIFICATIONS

A NIST scientist in his capacity as chairman of the X-Ray Program Mask Standards Committee established by the Defense Advanced Research Projects Agency, has led industry to adopt a standard limiting set of dimensions (the envelope) of the masks used for manufacturing integrated circuits defined through x-ray lithography. This accomplishment satisfies the charge given to the committee on its formation. An x-ray mask consists of a thin silicon membrane supported by a heavier frame; x-ray lithography extends the capabilities of optical lithography to finer dimensions, permitting the production of smaller integrated-circuit elements. The agreement constitutes an important step toward bringing x-ray lithography from the laboratory to the production line.

The committee also concluded that there is insufficient motivation for developing commonality between masks used with point (lower flux) and collimated (higher flux) sources, that there is no technical advantage anticipated from the concept of employing differing standards for primary master patterns and working x-ray mask copies, and that it would be neither necessary nor advantageous to impose any further dimensional constraints on x-ray masks until the technology becomes further advanced.

NEUTRON REFLECTOMETRY HELPS CHARACTERIZE POLYMER BRUSHES

Polymer brushes are central to many important problems in polymer science and biophysics, including colloid stabilization, polymeric surfactants, and polymer compatibalizers. Understanding the brush structure of the polymer chains is important in predicting the behavior of each of these systems.

Recently NIST scientists, in collaboration with researchers from two universities, have made a significant advance in determining the polymer segment density profile of these brushes using neutron reflectivity. The polymers used in this study are so-called "sticky foot" polystyrene in which one end of the polystyrene molecule has a functional group which adsorbs strongly onto the surface from the solution. This gives a very large density of adsorption of polymer near the surface, thus making neutron reflectivity measurements possible. NIST scientists use a technique unique to neutrons wherein the neutron beam traverses a large single crystal of silicon and reflects from the silicon-polymer solution interface, with the reflected beam again traversing the silicon crystal. For the first time, the neutron data show very strong minima and maxima in reflectivity, thereby significantly increasing the precision with which the structure of the polymer brushes adsorbed on the silicon-solution interface can be determined.

FAST RESTORATION OF IMAGES

Two NIST scientists have demonstrated the speed and flexibility which modern parallel computing can provide in restoring blurred images from a noisy background. Their restoration procedure, on a massively parallel machine (the Connection Machine at the University of Maryland Institute for Advanced Computer Studies), takes advantage of what the operator may know in advance and can recognize in the image as it is recovered.

Starting from a 512×512 image sample, the scientist first artificially blurred it, by convolution with a Gaussian-like point spread kernel, and then added random noise. This produced a blurred image, which resembled typical raw image data on a medical diagnosis system.

The recovery was undertaken by the method of "Tikhonov regularization"—using a low-pass spatial filter with an interactively set regularization parameter. In the presence of noise, the recovery of the image is a mathematically ill-posed problem. The computer by itself, not knowing the features of the image that are most important, may wander from the desired solution. The operator can sharpen important details in the recovered image by resetting the regularization parameter interactively.

In the recovered image, most of the significant detail from the original is present, plus a background pattern which originated with the noise component of the blurred data. These extraneous details can be easily ignored because the operator can distinguish them visually.

Massively parallel processing is fast, in this case making it possible to run the restoration process with many different settings of the regularization parameter.

NEUTRON FOCUSING USING CAPILLARY OPTICS

NIST researchers have been collaborating with researchers from the Kurchatov Institute for Atomic Energy Institute in Moscow and from the State University of New York at Albany on the use of multicapillary fibers for the focusing of neutrons. Recently, the researchers at NIST demonstrated the focusing of cold neutrons from the Cold Neutron Research Facility using a simple lens comprising a dozen of these capillary fibers. These neutron measurements were performed in conjunction with a newly developed charge transfer device neutron detector having a few tens of micrometers spatial resolution. A cooperative research and development agreement to develop multicapillary optical fibers for the transmission and focusing of cold neutrons has been signed with a private company.

These multicapillary fibers, which were developed at the Institute for Roentgen Optical Systems in Moscow, consist of thousands of parallel channels within a glass fiber of sub-millimeter diameter. Neutrons are guided down numerous open channels that are only 6 μm in diameter, a concept that has proved successful with x rays. Low-energy neutrons have optical properties analogous to those of photons and may be focused to produce significantly higher fluxes using the principle of mirror reflection from smooth surfaces at small grazing incident angles. The lens is formed by bending and orienting the fibers in such a way that the beams that emerge from each fiber point to the same spot, and so increase the neutron current density. Narrowly focused beams allow greater spatial resolution for neutron absorption measurements than previously available and suggest microprobe capabilities to complement other radiation techniques for multidimensional analysis in materials science.

NIST DEVELOPS METHODS FOR HIGH-PRECISION PHASE NOISE MEASUREMENTS

In response to new requirements of the U.S. aerospace industry for tighter phase noise specifications, NIST has developed the first measurement systems that yield high-precision phase noise measurements over a broad frequency range. Phase noise has been rising in importance in radars, telecommunications, and other systems where high spectral purity of signals is critical. Its presence in signal channels degrades the spectral purity and thus the performance of the system. The NIST phase noise measurement systems operate at carrier frequencies from 5 MHz to 26 GHz and 33 to 50 GHz with bandwidths up to 10 percent of the carrier frequency. The measurement precision ranges from about 1 to 2 dB depending on the operating conditions.

Commercial equipment for phase noise measurements have been available for several years, but there has been no satisfactory method for assuring that such systems were indeed giving accurate readings. The commercial systems are substantially more limited in dynamic range and precision. The NIST measurement systems have uncovered a number of measurement errors, some ranging from 5 to 20 dB.

HUBBLE DATA SUGGEST NO END FOR UNIVERSE

A team of scientists using NASA's Hubble Space Telescope (HST) has made the most precise measurement to date of the percent of deuterium (heavy hydrogen) in space. Led by a NIST astronomer and fellow of the Joint Institute for Laboratory Astrophysics in Boulder, CO, the researchers used HST's Goddard High Resolution Spectrograph to determine that the ratio of deuterium to hydrogen in space is 15 parts per million (15×10^{-6}). If the assumptions of the Big Bang theory for the universe's creation are correct, this ratio accounts for the maximum possible density of ordinary matter that can be present in the universe. The Hubble data also suggest that unless large amounts of some exotic form of matter exist in space, there is not enough matter present to halt the expansion of the universe. If true, the universe had a brilliant beginning but will have no end.

NEW "MEASURES" NEEDED TO BOOST PRODUCTIVITY

As American electronics firms strive to produce top-notch products, one factor emerges as a key to boosting domestic semiconductor productivity: measurement technology. This is the theme of a new NIST report, Metrology for the Semiconductor Industry. The 46-page document explains the importance of measurement in integrated circuit fabrication and how it enables manufacturers to better understand and control processes. The report says reliable measurement factors, such as circuit component dimensions and properties at various steps during the production process, are crucial. This ensures that processing errors are avoided and that faulty products are eliminated early in the production process. Besides presenting its measurement message, the report also details, in lay language, the semiconductor manufacturing process. For a free copy, contact Jane Walters, B344 Technology Building, NIST, Gaithersburg, MD 20899, 301/975-2050.

MEASUREMENT SERVICE FOR CW WATTMETERS COMING

NIST expects to establish a measurement service for high power continuous wave (cw) wattmeters in the near future. Measurements will be available at several points from 2 to 30 MHz (1 to 1,000 W) and 30 to 400 MHz (1 to 500 W). Advance notice is being provided because use of this service will require prearrangement with NIST. Wattmeters must be controllable via an IEEE-488 bus, have a type N male input connector, and either have a type N female output connector or be supplied with a load. At each measurement point, the customer will receive a calibration factor for the wattmeter, defined as the ratio of the wattmeter reading to the power incident on it. The measurement uncertainty for the new service is expected to be less than plus or minus 2 percent, depending on the frequency, power level, and electrical characteristics of the wattmeter/load combination. For more information, contact Gregorio Rebuldela or Jeffrey Jargon, Div. 813.01, NIST, Boulder, CO 80303, 303/497-3561.

NEW GLOSSARY OF COMPUTER SECURITY TERMINOLOGY

Computer security practitioners will be interested in The Glossary of Computer Security Terminology (NISTIR 4659), a collection of terms and definitions used by federal departments and agencies in their policies and standards. The 176-page document was developed under the auspices of the National Security Telecommunications and Information Systems Security Committee and published by NIST as part of its effort to distribute federally sponsored work. This glossary provides more than

one definition for many computer and communications security terms, reflecting the various uses by different federal agencies. Technical information on the publication is available from Edward Roback at 301/975-3696. The publication is for sale by the National Technical Information Service, Springfield, VA 22161 for $26 (hard copy) and $12.50 (microfiche) prepaid. Order by PB 92-112259/AS.

NEW PROCEEDINGS ISSUED ON HIGH INTEGRITY SOFTWARE

The Proceedings of the Workshop on High Integrity Software (NIST Special Publication 500-190) presents the results of a recent Assurance of High Integrity Software workshop sponsored by NIST. Participants addressed techniques, costs and benefits of assurance, controlled and encouraged practices, and hazard analysis. The workshop prepared a preliminary set of recommendations and proposed future directions for NIST to coordinate an effort to produce a comprehensive set of standards and guidelines for the assurance of high integrity software. Technical information on the workshop is available from Dolores R. Wallace at 301/975-3340. The publication is for sale by the National Technical Information Service, Springfield, VA 22161 for $17 (hard copy) and $9 (microfiche) prepaid. Order by PB 92-109040/AS.

AUTOMATED MANUFACTURING STARS IN NEW VHS PROGRAM

A new videotape describing information management strategies developed for NIST's Automated Manufacturing Research Facility (AMRF) was recently released. The AMRF is a prototype small-batch manufacturing facility used for integration and measurement-related standards research. "Information Management in the AMRF, November 1991," a 12 1/2 min tape describes five major manufacturing functions: design, process planning, off-line programming, shop floor control, and materials processing. Special emphasis is placed on how the AMRF manages information flow between these functions. The video is available on free loan by requesting title number 24798 from Modern Talking Picture Service Inc., 5000 Park St. North, St. Petersburg, FL 33709, 800/237-4599. VHS copies are $12 (shipping included) and may be purchased from Video Transfer Inc., 5709-B Arundel Ave., Rockville, MD 20852, 301/881-0270.

NIST REPORTS ON ISO 9000 STANDARD SERIES

Answers to many commonly asked questions about quality, quality systems, and the use and application of such systems are found in Questions and Answers on Quality, The ISO 9000 Standard Series, Quality System Registration, and Related Issues (NISTIR 4721). The report briefly describes the contents of the ISO 9000 standards that were published in 1987 by the International Organization for Standardization (ISO) in Geneva, Switzerland. The five international standards, along with the terminology and definitions contained in ISO Standard 8402, Quality-Vocabulary, provide guidance for industry decision makers on the selection of an appropriate quality management program or system. Among other topics, the report describes the conformity assessment scheme of the European Community (EC) for EC-regulated products. To obtain a copy of NISTIR 4721, send a self-addressed mailing label to the Standards Code and Information Program, A629 Administration Building, NIST, Gaithersburg, MD 20899, 301/975-4031.

SOFTWARE PACKAGE FOR ANTENNA METROLOGY AVAILABLE

A demanding task in antenna metrology is developing computer programs to process the massive amounts of measurement data needed to determine antenna performance characteristics. NIST scientists are currently creating a comprehensive and easy-to-use personal computer software package for conducting advanced research related to near-field antenna metrology. Ultimately, it will simplify methods for precisely determining the far-field properties of state-of-the-art antennas based on laboratory measurements. The software will isolate common computational themes and develop dedicated modules for use in performing computational tasks (involving real or simulated data for research and error analysis in antenna metrology). A recent NIST publication describes a software system that achieves a high degree of power, modularity, and flexibility for studying planar near-field measurements. The package consists of many FORTRAN modules that can be called from DOS to achieve a variety of computational tasks. For a copy of Personal Computer Codes for Analysis of Planar Near Fields (NISTIR 3970), contact the National Technical Information Service, Springfield, VA 22161. Order by PB 92-112283; the price is $19 prepaid.

NEW GUIDE DESIGNED TO HELP FEDERAL GOSIP USERS

Federal managers, procurement personnel, and technical specialists seeking to buy or evaluate Government Open Systems Interconnection Profile (GOSIP) products should find a new users guide helpful. The guide is a valuable reference designed to help federal users interpret GOSIP technical information. It also can aid users in setting up GOSIP-compliant products in the workplace. Persons with little or no experience in Open Systems Interconnection (OSI)—which allows unrelated computer systems to communicate in an open network environment—should be able to understand all portions of the guide. The guide also contains worthwhile information for the experienced OSI user. Government Open Systems Interconnection Profile Users' Guide, Version 2 is available for $26 prepaid from the National Technical Information Service, Springfield, VA 22161. Cite order number PB 92-119676/AS. (Note: This users guide serves as a companion document to Version 2 of GOSIP, issued as Federal Information Processing Standard (FIPS) 146-1. It is best used in conjunction with GOSIP and/or OSI documents.)

BOOK REVIEWS SUPERCRITICAL FLUID EXTRACTION

Two NIST researchers have authored and edited a definitive book that reviews the theory and applications of supercritical fluid technology. Over the past 5 years, there has been renewed interest in supercritical fluid extraction (SFE) methods. SFE has many industrial applications, but the systems must be carefully chosen. The best candidates for extraction are high-cost, low-volume commodities that require the use of a non-toxic solvent in their processing. The researchers have collected a series of reviews covering theoretical and experimental work geared toward the more exact requirements of current SFE applications. Supercritical Fluid Technology: Reviews in Modern Theory and Applications contains 16 chapters written by some of the foremost experts in this technology. For more information, contact Tom Bruno at Div. 838, NIST, Boulder, CO 80303, 303/497-5158.

VIDEO HIGHLIGHTS 1991 BALDRIGE AWARD WINNERS

What is quality management? Why is it important to U.S. competitiveness? How is it achieved? In a new 20 min video, representatives from the three 1991 winners of the Malcolm Baldrige National Quality Award answer these questions and others on quality and quality management strategies. The 1991 winners are Solectron Corp., San Jose, CA; Zytec Corp., Eden Prairie, MN; and Marlow Industries, Dallas, TX. The award, named for the late secretary of commerce, was established by federal legislation in August 1987. It promotes national awareness about the importance of improving quality management and recognizes quality achievements of U.S. companies. However, the award is not for specific products or services. The award program is managed by NIST, with the active involvement of the private sector, including the American Society for Quality Control (ASQC). The 1991 winners video is available from ASQC for $15. Item TA996 in ASQC's inventory, it can be ordered by calling 1-800/952-6587.

RADIO WAVES "LOWER THE BOOM" ON BURIED MINES

NIST has completed a 6 year effort to help the U.S. Army detect buried land mines (either plastic or metal) using electromagnetic (EM) technology. The method involves sending radio waves into the soil and analyzing the reflections received. A new report, Qualifying Standard Performance of Electromagnetic-Based Mine Detectors (NISTIR 3982), discusses the best ways of conducting controlled tests of portable detectors under varying soil conditions and recommends means for establishing a stable test range. Topics covered include: theoretical relationships between EM fields and matter; critical EM performance factors for portable mine detectors; measuring EM properties of materials relevant to EM mine detection; EM properties of soils and recommendations for simulated soil standards; desired properties and recommendations for simulated mine standards (both plastic and metal); recommended mine detector testing strategy; maintenance of test records and a test range; and recommendations for future work. Copies of NISTIR 3982 are available from the National Technical Information Service, Springfield, VA 22161. Order by PB 92-116292; the price is $26 ($9 microfiche).

PHOTONIC PROBES DEVELOPED TO MEASURE EM FIELDS

Photonic probes using lasers and fiber optics offer many advantages in electromagnetic field measurements, especially when measuring electromagnetic pulses (EMP) and high-power microwaves. These probes provide the wide bandwidth and low dispersion needed to measure EMP signals. They are free

from EM interference and provide minimal disturbance of the field being measured. NIST's interest has been in passive probes, where the probe head contains no active electronics or power supplies. A recent paper discusses the characteristics of photonic probes, presents an overview of system design (with emphasis on the transfer functions of appropriate antennas and electro-optic modulators), and details three photonic systems NIST has developed. For a copy of paper 61-91, contact Jo Emery, Div. 104, NIST, Boulder, CO 80303, 303/497-3237, fax: 303/497-5222.

SHAPING NEW DESIGNS FOR WAVE PROBES

There is a growing need for basic measurement support at millimeter wave and upper microwave frequencies. One requirement is for transfer standard probes—electric or magnetic field probes used for comparing standard electromagnetic fields generated in calibration laboratories. Another requirement is for radiation hazard meters. NIST scientists are using an optical sensor to measure the temperature rise of a resistive element in an electromagnetic field. In a recent paper, they report on the analyses and evaluations of numerous configurations for the resistive element. A sphere was chosen as the most promising shape. Several probe tips of this design were made and tested for sensitivity, frequency response, and linearity. Test results were very encouraging, with one design providing adequate performance for a transfer standard for millimeter waves. Report 54-91 is available from Jo Emery, Div. 104, NIST, Boulder, CO 80303, 303/497-3237.

IC DEVICE OFFERS IMPROVED SPEED, ACCURACY

NIST researchers have created a novel integrated circuit "comparator" that samples electrical signals faster and with less error than existing devices. Potential uses for the circuit include measuring performance of video display integrated circuits, where output voltage must change and settle rapidly to assure a crisp image. The NIST device eliminates thermal effects that can cause errors and affect voltage settling time. More than twice as fast as most other available comparators, it makes decisions with 0.1 percent accuracy within 2 ns following an abrupt input change. Unlike other comparators, the NIST device is intended for use only in a "strobed" or sampling mode (in which an unknown signal and a reference signal are compared on command). The circuit's inventors have applied to patent the device. For more information, contact Michael Souders, B162 Metrology Building, NIST, Gaithersburg, MD 20899, 301/975-2406.

ALASKA MARINE MAMMAL POLLUTION DATA AVAILABLE

Tissue samples from seals and whales in Alaska contain varying levels of pesticides, PCBs and trace elements, according to a new report by scientists from NIST and the National Oceanic and Atmospheric Administration (NOAA). The document presents baseline data from analyses of selected tissue samples in the Alaska Marine Mammal Tissue Archival Project (AMMTAP). The publication also describes the current inventory of tissue samples in the AMMTAP and methods used to analyze the samples. Since 1987, NIST and NOAA scientists have collected marine mammal tissue samples on subsistence hunts with Native Alaskans. The samples are stored at NIST's National Biomonitoring Specimen Bank in Gaithersburg, MD. The publication, AMMTAP: Sample Inventory and Results of Selected Samples for Organic and Trace Elements (NISTIR 4731), is available from the National Technical Information Service, Springfield, VA 22161 for $26 prepaid. Order by PB 92-143718.

SUPERCONDUCTOR ABSTRACTS COMPILED IN SINGLE VOLUME

The abstracts of 243 papers published by NIST authors in the field of high critical temperature superconductors have been collected and reprinted in High-Temperature Superconductivity: Abstracts of NIST Publications, 1987–1991 (NIST SP 826). These papers—which appear in proceedings of meetings, scientific and technical journals, and as NIST publications—represent work from nine of the institute's divisions. Many are the result of collaborations with researchers in industry, academia, and other government agencies. Abstracts are grouped in the following categories: compositional analysis; critical current and critical temperature; crystal structure; elastic constants and phonon spectra; electrical contacts; electronic structure; energy gap and tunneling spectra; Josephson effect and devices; magnetic measurements; phase equilibrium; processing—bulk material; and processing—thin films. SP 826 is available from the National Technical Information Service, Springfield, VA 22161, for $19 (paper) or $9 (microfiche) prepaid. Order by PB 92-126564/AS.

REPORT DETAILS RISKS, HANDLING CARE FOR 3480 TAPE

Since the mid-1980s, data centers have used 3480-type magnetic tape to archive information. Some users have saved critical data on literally thousands of 3480 cartridges. But what kind of shelf life can users expect from these magnetic media? Are 3480 tapes a dependable way to save crucial material? NIST researchers recently examined these issues and published their results in a new report, The 3480 Type Tape Cartridge: Potential Data Storage Risks, and Care and Handling Procedures to Minimize Risks (NIST SP 500-199). Under sponsorship of the National Oceanic and Atmospheric Administration, NIST appraised potential risks in using 3480 materials, studying factors such as chemical, mechanical, and magnetic failure mechanisms. The report summarizes reasonable procedures for the care and handling of the tapes to minimize risk. Also included are recommendations from applicable scientific literature and opinions from other tape experts. Available for $3.50 prepaid from the Superintendent of Documents, U.S. Government Printing Office, Washington, DC 20402-9325. Cite stock number SN 003-003-03127-5.

NIST ISSUES "HOW-TO" MANUAL ON SMOKE CONTROL

Smoke is the killer in most fires. Flowing silently through corridors, elevator shafts, and stairwells, it can be deadly even to those far removed from the fire. For example, most of the 85 people who died in the 1980 fire in the Las Vegas MGM Grand Hotel were far above the first floor where the fire started and was contained. Researchers at NIST have worked with private industry for several years to find ways to prevent such tragedies. The result is a new "how-to" manual for designing systems to control or contain smoke. The systems described in the manual use pressurization produced by mechanical fans. Such techniques have been used for at least 50 years to control the flow of airborne products such as dangerous gases or bacteria. However, only recently have they been considered for controlling smoke. The project was funded by the American Society of Heating, Refrigerating, and Air-Conditioning Engineers. Technical assistance came from the National Research Council of Canada and numerous industry experts. The Design Manual for Smoke Control Systems (NISTIR 4551) is available from the National Technical Information Service, Springfield, VA 22161 for $43 prepaid. Order by PB 92-144104.

BETTER SOLUTIONS FOR WAVE EQUATIONS OFFERED

NIST has published a tutorial monograph that features an improved method for deriving solutions to one of the basic equations of mathematical physics, the wave equation. Modified Airy Function and WKB Solutions to the Wave Equation (Monograph 176), defines the Modified Airy Function (MAF) method. The MAF method is more useful than the WKB method developed in the 1920s and long used for approximate solutions to problems in quantum mechanics and optical waveguides with a non-uniform refractive index. The monograph discusses and compares the WKB and MAF methods, drawing examples from the optical waveguide community. It also deals with eigenvalue and initial value problems. Single copies of Monograph 176 are available at no charge from R.L. Gallawa, Div. 814.02, NIST, Boulder, CO 80303, 303/497-3761. Multiple copies may be purchased from the Superintendent of Documents, U.S. Government Printing Office, Washington DC 20402-9325, for $5.50 each. Order by stock no. 003-003-03123-2.

NEW MICROSCOPE OFFERS UNPRECEDENTED RANGE

Imagine a camera that can image individual flowers in a Philadelphia tulip bed and then expand to successively larger frames until the 170 km expanse between Philadelphia and Baltimore is in view. By analogy, a novel scanning tunneling microscope (STM) designed by NIST researchers accommodates a comparable range for material surfaces. Sixty times better than the span of ranges achieved with standard STMs, the 600 000 times difference in the field permits greater viewing flexibility. One can attain a resolution of 1 nm—fine enough to scrutinize a cluster of molecules—or enlarge the field to survey a square area measuring 600 μm on a side. Researchers at NIST report the magnification range and zooming capabilities of their long-range STM rival that of a scanning electron microscope (SEM). Also, high-magnification viewing does not require placing samples in a vacuum chamber like an SEM. For more information, contact Theodore Vorburger, A117 Metrology Building, NIST, Gaithersburg, MD 20899, 301/975-3493.

NEW TEST IMPROVES UNDERSTANDING OF SMOKE DANGER

NIST researchers have developed the first comprehensive method for determining the toxic potency of smoke from burning materials. The technique provides a more realistic way of analyzing the potential hazard to humans of a burning product, such as a chair or wall covering. As manufacturers, code officials, and others gain experience and confidence with this method, say NIST researchers, the toxic potency of some products, such as those with similar chemical makeups, could be assessed without testing. This could speed the development of new products without adding risk to the consumer and will reduce the need for animal testing. The test includes a unique small-scale instrument for gathering accurate smoke toxicity data in conjunction with a method of predicting smoke toxicity that is faster and less costly than current toxicity tests. NIST is working with standards groups to have the NIST method accepted both in the United States and abroad as a standard smoke toxicity measurement. A report, Toxic Potency Measurement for Fire Hazard Analysis (NIST Special Publication 827), is available from the National Technical Information Service, Springfield, VA 22161 for $26 prepaid. Order by PB 92-137546.

NEW DETECTOR FOR GAS CHROMATOGRAPHY PATENTED

A NIST researcher has been granted a patent (U.S. Patent No. 5,070,024) for a hydrocarbon detector designed for use during gas chromatography in harsh industrial process environments. The research was sponsored by, and the patent assigned to, the Gas Research Institute, Chicago. The device indicates the presence and quantity of hydrocarbons in the exit stream of a gas chromatography column by sensing catalytic cracking of the hydrocarbons. It is much simpler in construction and operation than commonly available commercial detectors. By recording the temperature difference between gas flowing past a catalyst-coated thermopile (a linked group of thermocouples) and a similar uncoated thermopile, the device can determine the proportions of chemical components, identify unknowns, and distinguish between straight chain and branched hydrocarbons. The new device uses simple voltage-measuring instrumentation and is estimated to cost about one-tenth as much to fabricate as existing detectors. The detection cavity is very small, so minute amounts of hydrocarbons can be detected. For licensing information, contact Jeffrey Savidge, Gas Research Institute, 8600 W. Bryn Mawr Ave., Chicago, IL 60631, 312/399-8100. For technical information, contact Thomas Bruno, Div. 838.02, NIST, Boulder, CO 80303-3328, 303/497-5158.

GUIDE MAKES SRMs USEFUL TOOLS IN CHEMISTRY LABS

NIST chemists describe how analytical laboratories can assess the accuracy of their chemical analyses in a new publication describing the use of Standard Reference Materials (SRMs). The publication, Use of NIST Standard Reference Materials for Decisions on Performance of Analytical Chemical Methods and Laboratories (NIST Special Publication 829), guides laboratory managers on the most effective ways to use SRMs. SRMs serve as quality control standard samples for laboratories analyzing organic and inorganic compounds in a wide variety of materials. The NIST publication gives quality control managers specific guidelines for using SRMs to design measurement methods and interpret the accuracy of data. Copies are available from the Chemical Science and Technology Laboratory, A317 Chemistry Building, NIST, Gaithersburg, MD 20899, 301/975-3146.

CARB SOLVES SECOND SUGAR TRANSPORT PROTEIN

Researchers at the Center for Advanced Research in Biotechnology (CARB) have defined the three-dimensional structure of a second bacterial sugar-transport protein. The protein, known as histidine-containing phosphocarrier protein HPr, is essential for transporting energy from the environment into bacterial cells. The same CARB team solved the structure of a related bacterial sugar-transport protein last fall. Both proteins are involved in the same chain reaction that brings glucose molecules into bacterial cells. With protein structures such as these in hand, pharmaceutical companies may soon be designing drugs that prevent sugar transport and, in turn, starve infectious bacteria by cutting off their energy supply. Researchers from NIST, the University of Maryland, and the University of California at San Diego collaborated on the protein studies at CARB. A paper describing the new structure appears in the March 15, 1992, issue of Proceedings of the National Academy of Sciences. CARB was established in 1984 by NIST, the University of Maryland, and Montgomery County, MD, as a unique center for government, academic, and industry scientists.

PAPERS REQUESTED FOR FALL OPTICS SYMPOSIUM

NIST, in cooperation with the Institute of Electrical and Electronics Engineers (IEEE) Lasers and Electro-Optics Society and the Optical Society of America, will sponsor the 7th Biennial Symposium on Optical Fiber Measurements on Sept. 15–17, 1992, in Boulder, CO. Symposium sessions will cover measurements for things such as telecommunications fibers, fiber lasers and amplifiers, fibers for sensors, couplers, connectors, multiplexers, integrated optics, sources, detectors, modulators, switches, long-haul systems, LANs, subscriber loops, field and laboratory instrumentation, and standards. Experimental and analytical papers currently are being solicited on all aspects of the measurement of guided-lightwave technology. Summaries of proposed papers must be submitted by May 29, 1992, to Gordon W. Day, Program Chairman, Symposium on Optical Fiber Measurements, NIST, Div. 814.02, Boulder, CO 80303-3328. For more information on the symposium, contact the general chairman, Douglas L. Franzen, at the same address, or call 303/497-3346.

CONFORMITY ASSESSMENT PROGRAM PROPOSED

NIST is seeking public comments on a proposal to establish a voluntary conformity assessment systems evaluation (CASE) program. CASE will enable the Department of Commerce, acting through NIST, to assure foreign entities that U.S. conformity assessment activities related to laboratory testing, product certification, and quality systems registration satisfy international guidelines. NIST proposes to prescribe criteria and a system to evaluate and, when requested or directed, recognize specified conformity assessment activities. Program operation will be fully fee supported. Deadline for remarks is May 26, 1992. Comments or requests for information should be sent to Stanley I. Warshaw, Director, Office of Standard Services, A603 Administration Building, NIST, Gaithersburg, MD 20899, 301/975-4000, fax: 301/963-2371.

NEW ATLAS IMPROVES INFRARED SPECTROMETRY CALIBRATIONS

NIST recently published the most accurate atlas to date for the calibration of infrared spectrometers. Several hundred spectral maps and tables (with data based on frequency rather than wavelength techniques for absolute references) are presented for various calibration molecules. The text portion of the atlas contains a description of heterodyne frequency measurement techniques, details of the analysis, and calculation procedures. Intensities and lineshape parameters also are included. To order multiple copies of Wavenumber Calibration Tables from Heterodyne Frequency Measurements (NIST Special Publication 821), contact the Superintendent of Documents, U.S. Government Printing Office, Washington, DC 20402. Order by number 003-003-03136-4 for $31 prepaid.

COMMENTS SOUGHT FOR LANGUAGE C TEST METHOD

NIST is soliciting the views of industrial, public, and federal computer users about its choice of a method for testing C compilers for conformance to Federal Information Processing Standard (FIPS) 160. This FIPS, which adopts ANSI Standard X3.159-1989 Programming Language C, applies to C compilers acquired for federal use after Sept. 30, 1991. NIST has chosen the Perennial ANSI C Validation Suite as its test method and needs feedback to assess the method's suitability for appraising FIPS compliance. NIST also is using a trial validation service to verify the accuracy and completeness of its C validation procedures. The C standard is designed to permit portability of C applications across a variety of hardware configurations. NIST's test method and the results from its validation service will be especially helpful to federal agencies that require FIPS 160 conformance. Written comments on the NIST method should be sent to the Computer Systems Laboratory, Attn: C Test Service, A266, Technology Building, NIST, Gaithersburg, MD 20899.

REPORT EXAMINES "BRIDGING" SGML/ODA STANDARDS

Standard Generalized Markup Language (SGML) and Office Document Architecture (ODA) are the two most prominent international standards for markup and interchange of electronic documents. However, the two are incompatible. Documents encoded in SGML cannot be used directly in an ODA-based system, and vice versa. Users of one standard must learn the other before importing or exporting material encoded in the other standard. In a new report, NIST researchers explore creation of a "bridge" between the two standards. The report evaluates Office Document Language (ODL), an SGML application specifically designed for ODA documents. Also described is a translation program that converts SGML documents to ODA and back. The report concedes that both

standards have loyal users and will likely be around for some time, so it suggests ways to minimize costly duplication efforts and allow users of each standard to take advantage of features offered by the other. On the Interchangeability of SGML and ODA (NISTIR 4681) is available for $17 (print) or $9 (microfiche) prepaid from the National Technical Information Service, Springfield, VA 22161. Order by number PB 92-149830/AS.

SUMMER TECHNOLOGY OUTREACH CONFERENCES SCHEDULED

An updated schedule has been announced for the eight remaining National Technology Initiative (NTI) meetings. The new schedule includes a date, July 9, for the 10th meeting in Gaithersburg, MD, and plans for an 11th meeting on July 22 in Princeton, NJ. Co-sponsored by the Departments of Commerce, Energy, and Transportation, and NASA, NTI is designed to promote industry/government collaborations and commercialization of federal R&D technologies. Meetings cover two topics of regional interest (listed below) and include core sections on manufacturing partnerships, financing, and cooperative research and development relationships. The remaining schedule for NTI meetings is: May 14, Seattle, WA (transportation, environment); May 28, Pasadena, CA (aerospace, biotechnology); June 11, Denver, CO (natural resources, communications); June 25, Kansas City, MO (agricultural technology, advanced manufacturing); July 9, Gaithersburg, MD (life sciences, systems integration); and July 22, Princeton, NJ (transportation, electronics).

NIST LABORATORY METROLOGY SEMINAR HELD AT THE UNIVERSITY OF PUERTO RICO (UPR), MAYAGUEZ

The NIST Office of Weights and Measures (OWM) sponsored a laboratory metrology seminar at UPR in Mayaguez Feb. 10–14, in cooperation with the Puerto Rican Weights and Measures Division, Department of Consumer Affairs. The seminar was coordinated through the Center for Cooperation in Education and Research in Engineering and Applied Science (Co-Hemis), also representing national agencies in charge of technological research in Argentina, Canada, Costa Rica, Cuba, Chile, Guatemala, Mexico, Peru, Dominican Republic, Trinidad-Tobago, Uruguay, and Venezuela.

The seminar was taught in English by a member of NIST OWM and in Spanish by a representative of the P.R. Department of Consumer Affairs. They covered basic measurement concepts and procedures in mass, volume, statistics, and measurement control programs as part of laboratory quality assurance. Most of the participants represented legal metrology or legal weights and measures jurisdictions (U.S. Virgin Islands, St. Lucia Bureau of Standards, Direccion General de Normas of Mexico, Jamaica Bureau of Standards, Grenada Bureau of Standards, and Barbados National Standards Institution); private industry also was represented (National Standards of Puerto Rico, Inc., and Advanced Instruments, also of Puerto Rico). Participants were excited about this opportunity for training; plans are being made for interlaboratory measurements in mass calibration during the next year. Another meeting is being planned for February 1993, with the objective of creating an ongoing Regional Measurement Assurance Program Group.

SPHERICAL-WAVE EXPANSIONS OF PISTON-RADIATOR FIELDS, ALGORITHM DERIVED

Researchers from NIST and the Air Force have derived simple spherical-wave expansions of the continuous-wave fields of a circular piston radiator in a rigid baffle and presented their derivation in a paper recently published in the Journal of the Acoustical Society of America. The team also has produced an accurate and efficient algorithm for numerical computation of the near field, based upon the spherical-wave expansions. This work represents a key step toward the solution of an important electromagnetic field problem and, at the same time, constitutes a significant contribution to the science of acoustics. The motivation for the research was the need for a model electromagnetic field radiator that is both totally understood and physically realizable, for use in validating methods for measuring radiated fields. Through their calculations, the researchers have shed new light on the long-standing problem of determining the near field of a piston radiator transducer. This is the (scalar) acoustic analog of the (vector) electromagnetic field problem of analytically determining the radiated field of a uniformly excited circular aperture. The entire field, both near field and far field of the piston radiator is, therefore, completely characterized. The work provides the scientific community with

the first exact spherical wave expansion that makes possible a complete understanding of the near-field structure of the piston radiator from a theoretical point of view. The expansions are of considerable interest since there are relatively few non-trivial problems for which a complete development in spherical-wave modes can be given.

NIST TO APPLY PROBE POSITION-ERROR CORRECTION IN NEW NEAR-FIELD SPHERICAL SCANNING RANGE

NIST scientists have developed methods for correcting for positional errors of the probes used in near-field spherical scanning. These methods are both theoretical and computational in nature and will be used in the measurements to be made in the NIST near-field spherical scanning range now under development and have general applicability to other spherical ranges. In near-field scanning, amplitude and phase measurements are made close to (i.e., in the near field) the antenna being measured, and the resulting data are mathematically transformed into plots of the antenna's far field. In the NIST spherical range, position errors, defined as differences between the actual positions of the probe and mathematically defined regular grid points lying on the surface of a true sphere (or spherical segment), will be measured accurately by means of angle encoders and a state-of-the-art laser positioning system. Position errors in any of the three spherical coordinates introduce phase errors in the near-field data, leading to significant errors in the calculated far field. The removal of position errors from the near-field data therefore improves the accuracy of the determination of the far field. This process becomes increasingly important and necessary at higher frequencies, where position errors are a significant fraction of the wavelength.

NIST SCIENTIST REPORTS FINDINGS OF NASA'S AIRBORNE ARCTIC STRATOSPHERIC EXPEDITION II

A NIST scientist reported the preliminary findings of the NASA Airborne Arctic Stratospheric Expedition II. He is the acting manager of the NASA Upper Atmosphere Research Program and served as program manager/scientist for the airborne expedition.

The expedition took place between October and January and involved sampling the upper atmosphere from aircraft flying out of Fairbanks, Alaska, and Bangor, Maine. The expedition team sought information about the causes of widespread stratospheric ozone decreases over mid-latitudes in the first part of the calendar year and about the effects of volcanic debris on the chemical processes which govern stratospheric ozone depletion.

The researchers found elevated levels of reactive intermediates known to be responsible for ozone destruction over a wide area ranging from eastern Canada to the southernmost latitudes examined in the study, the central Caribbean. Evidence was obtained that reactions on aerosol surfaces reduce the concentration of reactive forms of nitrogen oxides, which act as a brake on ozone destruction by ClO and BrO. Volcanic debris from the eruption of Mt. Pinatubo was shown to facilitate the rate of ozone loss, leading to a conclusion that the volcanic eruption may lead to enhanced ozone layer reduction for several years.

FLUID EQUILIBRATION IN LOW GRAVITY

Two NIST scientists participated in an experiment flown on the space shuttle Discovery Jan. 22-30. Direct and interferometric images were used to record the equilibration of a small sample of fluid sulfur hexafluoride (SF_6) following changes in the temperature. Since the density and temperature of this fluid are near the critical point, this process, which ordinarily takes place in seconds, can take as long as 1 hour. It is known that on Earth, gravity greatly affects the final density distribution; however, the influence of gravity on the way the fluid achieves this equilibrium is unclear. Once the data from the microgravity experiment are analyzed, the results should provide a better theoretical understanding of this process and guide the design of future low-gravity critical point experiments.

The experiment team was headed by a NASA scientist and included participants from the University of Maryland and the Technical University in Munich. This team was one of three using the Critical Point Facility developed through the European Space Agency's microgravity program. Participation in the mission, named International Microgravity Laboratory-One, included researchers from 14 countries.

NIST RADIO BROADCASTS TO SUPPORT INSPIRE PROGRAM FOR HIGH SCHOOL SCIENCE STUDENTS

NIST time and frequency broadcast station WWV will provide short broadcasts of scheduling information to high school science students participating in the Interactive NASA Space Physics Ionosphere Radio Experiment (INSPIRE). This unique program will involve radio reception of signals produced by a beam of accelerated electrons modulated at various audio frequencies. The beam of electrons will be guided by the Earth's magnetic field producing a large virtual an-tenna. The experiment requires reception of the signals on Earth with a geographically diverse network of receivers. This network will be provided by INSPIRE, which is a group made up of physicists, amateur radio enthusiasts, scientific experimenters, and teachers. One objective is to involve a large number of high school students in the program.

Equipment for the satellite-signal broadcasts was carried on the space shuttle in March in the first of 10 ATLAS (ATmospheric Laboratory for Applications and Science) missions. Taped observations made by the INSPIRE network will be gathered to determine the footprint of the arriving signals, providing information on the propagation of signals through the ionosphere and magnetosphere. Since the schedule of broadcasts from space was subject to changes, a means for communicating these changes to the observers was needed. With its broad geographic coverage, the NIST shortwave broadcasts can meet this need. Furthermore, automated methods for recording messages for broadcast are already in place providing special announcements (e.g., marine storm warnings) for other agencies.

IONOSPHERIC RECEIVER TECHNOLOGY TRANSFERRED TO INDUSTRY

NIST scientists have successfully transferred the technology for a codeless GPS ionospheric receiver to a local Colorado company that deals in atmospheric measurement technology. The general idea of a codeless GPS receiver had been conceived by several organizations including the Jet Propulsion Laboratory, but no implementation to date has been as simple and versatile as the NIST receiver.

NIST developed the receiver in order to provide for continuous measurement of the ionospheric delay involved in time transfer using the common-view method (also developed by NIST). The receiver picks up signals from two different frequencies broadcast by the GPS satellites and, from the phase difference of the signals, determines the ionospheric delay and thus the free electron content along the path to the satellite. The receiver stores a catalogue of all GPS satellites and identifies each from its Doppler signature. It can track approximately 10 satellites, simultaneously providing ionospheric measurements for each.

While the market for receivers that measure the ionospheric time-delay is significant, the systems can potentially be used for improving the accuracy of geophysical GPS surveying and for studies of the ionosphere. In fact, this latter application is important, because the current measurement method for studying the ionosphere involves expensive and cumbersome use of reflected radar signals which then only provide a measure of the vertical ionospheric component.

OBSERVATION OF "QUANTUM PROJECTION" NOISE

NIST scientists have completed and published theoretical and experimental work describing a previously unrecognized noise source they have called "quantum projection" noise.

In spectroscopy, "technical noise," such as laser amplitude fluctuations caused by an unstable power supply, often dominates the noise. These sources of noise can be eliminated by careful engineering. Two examples of more fundamental noise sources are the detection shot noise in a laser absorption spectroscopy experiment and the fluctuations in signal caused by the fluctuations in the number of atoms in an atomic beam experiment. These sources of noise also can be eliminated or significantly reduced. For example, laser shot noise can, in principle, be reduced by use of squeezed light. In a stored-ion experiment, the number of ions can be held constant, thereby reducing the atomic number fluctuations to zero. Also, when absorption is detected using electron shelving, the detection noise approaches zero since 100 percent detection efficiency is possible. Because of this immunity from some sources of noise, the NIST scientists have been able to observe this "quantum projection" noise in a clear manner. Basically, this source of noise is caused by the statistical fluctuations in the number of atomic absorbers (ions in this case) that are observed to make the transition in an absorption spectroscopy experiment.

APPARATUS FOR MEASURING THERMAL CONDUCTIVITY AT LOW TEMPERATURES

A guarded-hot-plate apparatus has been developed to measure the thermal conductivity of insulating materials in the temperature range 10 to 400 K. NIST is using the new apparatus to perform measurements for a private company on foam insulations with environmentally acceptable fill gases. The specimen environment may be vacuum or non-condensing gas and the mechanical load on the specimen may be varied from 222 N to 8896 N during a test. Specimen diameter is 30.5 cm and thickness up to 5 cm can be accommodated. Initial test results suggest an uncertainty of 2 percent for polymeric foam insulations. The apparatus was designed to optimize operation at low temperatures, e.g., a variable heat switch is used to provide refrigeration from a static cryogenic bath. Data acquisition and temperature control are completely automated so that extensive data sets can be generated with minimal operator interaction.

PROPOSED CONSORTIUM ON CASTING OF AEROSPACE ALLOYS

NIST scientists recently met with industrial representatives to initiate the planning for a NIST-administered consortium on casting of aerospace alloys. The meeting, which was sponsored by the Aerospace Industries Association, the National Center for Advanced Technologies, and the NIST Office of Intelligent Processing of Materials, took place on Jan. 16 at the Aerospace Industries Association in Washington, DC. There were 31 attendees from a wide variety of aerospace companies and universities. There were also representatives from NSF, DARPA, and the Bureau of Mines.

A consensus was reached at the meeting that a consortium should be formed to carry out precompetitive generic research to improve the processing of aerospace metal alloys by casting. Further planning by the potential consortium members is currently under way in the areas of process modeling, process sensing, and thermophysical properties data. A tentative consortium initiation date of July 1 has been set.

ELECTRODEPOSITION OF COMPOSITIONALLY MODULATED ALLOYS

Nanostructural alloys are a new class of materials whose unusual properties are a result of the large volume fraction of atoms either in, or close to, an interface within the structure. These materials may be both compositionally and structurally modulated and include both metals and ceramics. Studies at NIST show that it is possible to produce compositionally modulated alloys with layers as thin as two monolayers using electrochemical techniques. The virtually atomic-scale control of composition allows the production of alloys with tailored (or designed) magnetic, optical, and mechanical properties. It has been demonstrated that microlayered alloys produced electrochemically exhibit a much higher degree of perfection than comparably produced sputtered alloys and that large-scale structures can be electroformed with near atomic control over properties. Microlayered alloys have clear applications to electrical contacts, magnetic recording, and semiconductor devices.

TECHNOLOGY OF GLASS-CERAMIC INSERTS TRANSFERRED TO DENTAL MATERIALS INDUSTRY

Glass-ceramic inserts for composite dental restorations, a technology invented by an American Dental Association research associate, were recently introduced to the dental materials marketplace. Appropriate premolded sizes and shapes of tooth-colored beta-quartz solid-solution glass-ceramic are inserted into dental composite fillings prior to polymerization. The inserts decrease polymerization shrinkage, increase the modulus of elasticity, and may improve the dimensional stability of occlusal and interproximal restorations. Insert kits were introduced in fall 1991 to the United States and world markets.

The inventor is director of the Paffenbarger Research Center in the dental and medical materials group at NIST. NIST scientists advised the inventor and his research team and provided glass melts.

PREDICTING PERFORMANCE OF ADHESIVE BONDS

A new study at NIST shows that the fracture energy of adhesive bonds loaded in shear can be predicted from a knowledge of the stress-strain behavior of the adhesive. This is an important result because the inability to predict failure in adhesive joints is a major factor limiting their use, particularly in structural applications where adhesives offer the significant advantages of lower weight and design flexibility. The recent work successfully treats the critical role played by the bond thickness. Restricting the adhesive to thin layers significantly changes its mechanical properties, which are important in the fracture of bonded joints. The study used video microscopy to record

the details of the deformation behavior in the crack-tip region during fracture and compared these data with results from stress-strain experiments conducted on the same adhesive confined to a thin layer with a thickness equal to that in the adhesive bond. The strain to failure in thin-layer specimens was found to be much greater than that obtained from experiments on bulk samples because of the inability for flaws to develop in very thin layers. The area under the stress-strain curve of a thin layer adhesive was found to correlate very well with the adhesive fracture energy. This new understanding will help improve the design of new adhesive systems and increase the ability to predict the lifetimes of bonded structures.

NIST STUDY OF STAGING AREAS FOR PERSONS WITH MOBILITY LIMITATIONS

NIST has completed a project for the General Services Administration (GSA) to evaluate the concept of a staging area as a means of fire protection for persons with disabilities. GSA has modified six buildings as test installations with staging areas. Staging areas are intended as spaces in which people with disabilities can safely wait during a fire. Spaces that were turned into staging areas included passenger elevator lobbies, service elevator lobbies, sections of corridor, and rooms. The NIST project consisted of field tests, human behavior studies, and threat analysis. The threat analysis evaluated tenability in route to staging areas and within staging areas due to transport of smoke from post flashover fires, sprinklered fires, and smoldering fires. The sprinklered fires were based on a model of post-sprinkler heat release recently developed by a NIST scientist.

It was concluded that staging areas can be either a haven of safety or a death trap. The difference is highly dependent on details of design, the type of fire exposure, outside wind and temperature conditions, and the capability and reliability of the smoke control pressurization system. Without pressurization, all staging areas studied are subject to lethal failure. In many cases, the persons most needing the staging area protection may be unable to reach that area before their pathway (corridor or aisle ways) becomes lethal. Further, it was concluded that the operation of a properly designed sprinkler system eliminates the life threat to all occupants regardless of their individual abilities and can provide superior protection for people with disabilities as compared to staging areas.

NIST COLLABORATES WITH THE NATIONAL ARCHIVES AND RECORDS ADMINISTRATION (NARA) ON OPTICAL DISK TECHNOLOGY

Development of a Testing Methodology To Predict Optical Disk Life Expectancy Values (NIST SP 500-200) reports the results of a cooperative research effort to develop a methodology for determining how long records may be safely stored on optical disk media. Partially sponsored by NARA, NIST researchers set up an optical media measurement laboratory to test and analyze optical disk media characteristics and to produce a testing methodology that can be used to derive life expectancy values for optical disks. A standardized test methodology and standards for measuring media characteristics would assist federal managers in selecting the right media for the storage of permanent records.

NIST PROPOSES FEDERAL INFORMATION PROCESSING STANDARD (FIPS) FOR SECURE HASH STANDARD

A FIPS for Secure Hash Standard has been proposed which specifies a Secure Hash Algorithm (SHA) for use with the proposed Digital Signature Standard. For applications not requiring a digital signature, the SHA would be required whenever a secure hash algorithm is needed for federal applications.

The hash standard provides a formula for producing a numeric value (called a "message digest") of a message (or more generically, any digital information). The formula is devised so that virtually any change to the message results in a change to the message digest. The message digest can be recalculated at any time and compared to the original. If they are not identical, the information has been changed. This mechanism verifies the integrity of data.

SPATIAL DATA TRANSFER STANDARD IMPLEMENTATION WORKSHOP ATTRACTS LARGE TURNOUT

NIST, in cooperation with the National Mapping Division, United States Geological Survey, and the Standards Working Group, Federal Geographic Data Committee, held a Spatial Data Transfer Standard (SDTS) Implementation Workshop Feb. 18–21 at NIST. The workshop attracted about 150 participants from government, industry, and academia.

SDTS recently completed the Federal Register comment and review period of the FIPS approval

process. SDTS is the result of major efforts by federal and national organizations during the past 10 years. Specifications are provided for the organization and structure of digital spatial data transfer, definition of spatial features and attributes, and data transfer encoding.

Following in-depth tutorials on SDTS implementation, the workshop featured a demonstration of encoding and decoding test data. Other sessions covered the refinement of the Federal Vector Profile with Topology and an initiation in developing a SDTS Raster Profile. This is the first of a series of workshops designed to educate the vendor community on the implementation of SDTS.

INTERNATIONAL WORKSHOP ON HARMONIZING CONFORMANCE TESTING OF PROGRAMMING LANGUAGE STANDARDS HELD

NIST recently convened the sixth in a series of international workshops on harmonizing validation procedures for testing implementations for conformance to programming language standards. The Instituto Italiano del Marchio di Qualita hosted the workshop in Milano, Italy; countries represented included the United Kingdom, France, Italy, Japan, Germany, and the United States. The workshop brought together conformance testing experts for the programming languages of COBOL, Pascal, Ada, FORTRAN, MUMPS, C, and the graphical standards of Graphical Kernel System, Computer Graphics Metafile, and Computer Graphics Interface.

The European participants briefed participants on an application that has been made to the European Committee for IT Testing and Certification to register a new agreement group, the Graphics and Languages–Agreement Group for Testing and Certification (GLATC). The GLATC group is using documents produced in previous workshops as the basis for developing the GLATC recognition arrangement. Expanding the format of workshops to include graphic standards validation activities also was considered.

Attendees focused on updating guidelines for vendors to register equivalent hardware and software environments and on developing a procedural model for coordinated maintenance and control of test suites. A proposal was made to register test reports rather than certificates for products found to have areas of non-conformance. Finally, the workshop updated the Areas of Agreement document, which covers test laboratory accreditation, test reports, registration, certification, and mutual recognition.

Calibration Services

UPDATED CALIBRATION SERVICES USERS GUIDE AVAILABLE

More than 500 different calibration services, special test services, and measurement assurance programs (MAPs) are listed in the NIST Calibration Services Users Guide 1991 (SP 250). The services referenced are the most accurate calibrations of their type in the United States. These calibrations directly link a customer's precision equipment or in-house transfer standards to national standards. Services are listed in the following seven areas: dimensional; mechanical (including flow, acoustic, and ultrasonic); thermodynamic quantities; optical radiation; ionizing radiation; electromagnetic (including direct current, alternating current, radio frequency, and microwave); and time and frequency measurements. Copies of the guide are available from the Calibration Program, A104 Building 411, NIST, Gaithersburg, MD 20899, 301/975-2002.

Standard Reference Materials

EASY ACCESS TO MATERIALS STANDARDS OFFERED

Thanks to a group of new NIST brochures, producers and manufacturers of plastic, rubber, glass, ceramic, and metal products now have rapid access to special listings of Standard Reference Materials (SRMs). The brochures list more than 400 available SRMs with certified chemical and physical properties for calibrating instruments and evaluating measurement systems. These SRMs help industry achieve greater quality assurance of materials and goods by improving measurement accuracy. The group of six brochures lists SRMs for polymers; glass and related materials; ferrous metals; non-ferrous metals; cast iron; and ores, minerals, and refractories. Copies of the brochures (part of a series of 16 on select SRMs), as well as information on more than 1,200 other certified calibration standards on nutrition, clinical health, engineering materials, and environmental standards, are available from the Standard Reference Materials Program, Rm. 204, Building 202, NIST, Gaithersburg, MD 20899, 301/975-6776.

SRM IMPROVES LEAD POISONING DIAGNOSIS ACCURACY

Public health officials warn that lead poisoning—from household paints, dust, and water pipes in 57 million American homes—is a serious environmental threat facing U.S. children. The Centers for Disease Control (CDC) responded to this issue in October 1991 by lowering the tolerable threshold for lead in blood to 10 μg/dL (100 parts in 10^9), and recommending lead screenings for all 12-month olds. In order to help labs more accurately measure low lead levels (less than 50 parts in 10^9), NIST has issued a new Standard Reference Material (SRM) for lead in blood. The SRM contains four vials of frozen cow blood, each with a certified lead concentration between 5 and 55 μg/dL. NIST scientists collaborated with environmental health specialists at the CDC in preparing SRM 955a, available for $261. To order, contact the Standard Reference Materials Program, Rm. 204, Building 202, NIST, Gaithersburg, MD 20899, 301/975-6776.

SAMPLE AVAILABLE FOR HUMAN HAIR DRUG ANALYSIS

Researchers seeking an alternative to urinalysis for identifying drug abusers are looking strongly at using human hair. Studies show that after ingestion, drugs are incorporated into hair and remain detectable for long periods of time. This gives law enforcers a method sensitive enough to reveal drug use from months past instead of just within a few days of the test date. In addition, only a small amount of hair is required and samples can be obtained from the scalp without cosmetic effect. This could help avoid privacy issues often associated with urinalysis. NIST researchers have created a reference material (Reference Material 8449) to help ensure hair test accuracy, making the analysis more reliable and, hopefully, more admissible as legal evidence. The product is a bottled sample of human hair in powdered form that contains known amounts of each of four different drugs: cocaine, morphine, codeine, and benzoylecgonine. Because the drug quantities are fixed, investigators can use the sample to check analytical instruments or ensure measurement compatibility among laboratories. One unit of RM 8449 costs $276 from the Standard Reference Materials Program, Rm. 205, Building 202, NIST, Gaithersburg, MD 20899, 301/975-6776.

STANDARD REFERENCE MATERIAL 893 AND 1295—STAINLESS STEEL (SAE 405)

The Standard Reference Materials Program announces the availability of Stainless Steel (SAE 405) Standard Reference Materials (SRMs) 893 and 1295. SRM 893 is in the form of chips sized between 0.5 and 1.18 mm, and is intended for use in chemical methods of analysis. SRM 1295 is in the form of a disk, approximately 32 mm in diameter, and is intended for use in optical emission and x-ray spectrometric methods of analysis. These SRMs are certified for chromium at 13.5 weight percent and for 10 other elements which occur at concentrations of less than one weight percent.

They were developed and certified under the auspices of the ASTM-NIST Research Associate Program.

STANDARD REFERENCE MATERIAL 2708—ZINC SULFIDE THIN FILM ON POLYCARBONATE

The Standard Reference Materials Program announces the availability of a zinc sulfide thin film standard, Standard Reference Material (SRM) 2708. It is intended primarily for use in the standardization of x-ray fluorescence spectrometers for sulfur determinations in applications where measurements are made of particulate matter collected on filter media or on thin films. It consists of a single layer of zinc sulfide, about 0.02 μm thick, deposited on a polycarbonate filter and mounted on an aluminum ring to maintain uniform geometry. Certification for sulfur is based on isotope dilution thermal ionization mass spectrometry; an informational (non-certified) value is provided for zinc.

STANDARD REFERENCE MATERIAL 2034—HOLMIUM OXIDE SOLUTION WAVELENGTH STANDARD 240 TO 650 nm

The Standard Reference Materials Program announces the availability of a renewal lot of Standard Reference Material (SRM) 2034. This SRM is a certified transfer standard intended for the verification and calibration of the wavelength scale of ultraviolet and visible absorption spectrometers having nominal bandwidths not exceeding 3 nm. Certification is for wavelength location of minimum transmittance of 14 bands at each of six

bandwidths, in the range 240-650 nm. SRM 2034 is an aqueous solution of four percent (by weight) holmium oxide in 10 percent (V/V) perchloric acid, flame sealed in a non-fluorescent fused-silica cuvette of optical quality. The square cuvette has a nominal 10 mm pathlength and will fit into the sample compartments of most conventional absorption spectrometers.

REFERENCE MATERIALS 8506 AND 8507—MOISTURE IN TRANSFORMER OIL AND IN MINERAL OIL

The Standard Reference Materials Program announces the availability of Reference Materials (RMs) 8506 and 8507, primarily intended for use in calibration of equipment used to determine water in transformer oils, mineral oils, and/or materials of a similar matrix. RM 8506 is a petroleum electrical insulating oil containing 21 mg/kg water, while RM 8507 is a petroleum lubricating oil containing 47 mg/kg water. Coulometric Karl Fischer measurements from two round-robin analytical programs were used to assign the reference concentration values; chromatographic and Karl Fischer measurements made at NIST were used for confirmation.

Standard Reference Data

NEW PC PACKAGE SPEEDS CHEMICAL MICROANALYSIS

Scientists using electron microscopy to analyze chemical composition can save hours of laboratory work with a new software and database package from NIST and the National Institutes of Health. The system, called the Desktop Spectrum Analyzer and X-Ray Database (DTSA), can simulate experiments and evaluate electron microscopy data. It allows scientists to design effective experiments quickly without using trial and error to find the best experimental conditions. With a special acquisition board installed in the desktop computer, the DTSA also can collect data directly from an electron microscope. The DTSA sells for $790 through the Standard Reference Data Program at NIST. It is designed for Apple Macintosh II series computers and requires a minimum of 4 megabytes of memory. For more information, contact the Standard Reference Data Program, A320 Physics Building, NIST, Gaithersburg, MD 20899, 301/975-2208, fax: 301/926-0416.

Volume 97, Number 2, March–April 1991
Journal of Research of the National Institute of Standards and Technology

Calendar

August 2–6, 1992
NATIONAL CONFERENCE OF STANDARDS LABORATORIES WORKSHOP AND SYMPOSIUM "MANAGING WORLDWIDE MEASUREMENTS"

Location: Grand Hyatt Washington
Washington, DC

Purpose: To provide a forum for exchange of ideas, techniques, and innovations among those engaged in measurement science and has evolved as a major educational activity of the year for the measurement community worldwide.
Topics: Technical sessions include papers on mechanical, dimensional, electrical, optical, and temperature. Managaement sessions on international standards, develo;pment of a calibration lab, and laboratoary accreditation. In addition there will be workshops on subjects such as: Intrinsic and Derived Standards, Automatic Test Equipment, Measurement Assurance, National Measurement Requirements, Biomedical and Phaarmaceutical Metrology.
Format: Symposium, exhibits and workshop sessions.
Sponsors: NIST and the National Conference of Standards Laboratories (NCSL).
Contact: Wilbur Anson, 303/440-3339, NCSL, 1880–30th St., Suite 305B, Boulder, CO 80301.